

Title	Study on the Energy-Saving Mechanism of Rudder-Bulb-Fins System Applied to KVLCC2 Model in Waves
Author(s)	Htay, Win Naing
Citation	大阪大学, 2022, 博士論文
Version Type	VoR
URL	https://doi.org/10.18910/89631
rights	
Note	

Osaka University Knowledge Archive : OUKA

<https://ir.library.osaka-u.ac.jp/>

Osaka University

Doctoral Dissertation

Study on the Energy-Saving Mechanism of Rudder-Bulb-Fins
System Applied to KVLCC2 Model in Waves

(波浪中における KVLCC2 模型に対する舵-バルブ-フィン
システムの省エネルギー性能に関する研究)

WIN NAING HTAY

June 2022

Department of Naval Architecture and Ocean Engineering
Division of Global Architecture
Graduate School of Engineering,
Osaka University

Study on the Energy-Saving Mechanism of Rudder-Bulb-Fins System Applied to KVLCC2 Model in Waves

By

Win Naing Htay

A Dissertation for Doctor of Engineering Degree submitted to
Graduate School of Engineering

Department of Naval Architecture and Ocean Engineering

Osaka University

in

June 2022

Supervised by

Professor Yasuyuki Toda

Professor Hiroyoshi Suzuki

Committee members

Professor Naoya Umeda

Associate Professor Atsuo Maki

Acknowledgement

Throughout conducting this research and writing this dissertation, I would firstly like to thank my advisor, Professor Yasuyuki TODA for allowing me to study and perform my research in his laboratory and supporting me with his precious expert academic knowledge and patient and kind guidance. The door to Prof. Toda's office always opens for me whenever I run into a trouble spot and have a question or want to ask some suggestion or advice not only about my research or writing academic papers but also for other problems.

I would like to appreciate Professor Hiroyoshi Suzuki for his supervision of my dissertation and for taking kind care of me after the retirement of Professor Yasuyuki Toda.

I would like to thank Professor Ping-Chen Wu for his technical support and explanation concerned with some computer applications when I just arrived at Osaka University, Japan.

I wish to express my sincere gratitude to all the professors from my department not only at Osaka University but also at Myanmar Maritime University where I studied for my bachelor's degree for their precious lectures and speeches.

My sincere thanks also go to all of my seniors from my laboratory, Dr Truong Quang Tho, Dr MD. Alfaz Hossain, Dr Seemontini RoyChoudhury, and Dr Mwangi Benson Oyunge for their patient and kind technical support for some computer applications, for sharing their valuable experience and knowledge, and giving me the motivation to become a good researcher.

I am very grateful to all members of my laboratory, especially Mr Yuji Tsuda and Mr Ogawa Shunya, for the moment that I could learn some Japanese terms for my research and could exchange knowledge during solving the simulation problems together.

I am wholeheartedly thankful to the Ministry of Education, Culture, Sports, Science and Technology, Japan (MEXT) for supporting me financially.

Last but not least, I also want to express my appreciation to my family, relatives, and friends in both Japan and Myanmar for their sacrifices, patience and support either mentally or physically throughout my academic journey which has contributed to this achievement.

Abstract

Along with the making vigorous efforts on meeting the specific customers' demands, the shipyards have been facing consistently many challenges concerned with global energy crises and environmental protection. One of the biggest challenges is to enforce the carbon dioxide emission regulations implemented by the International Maritime Organization, mainly the Energy Efficiency Design Index (EEDI) in the last decade. By the same token, the United Nations adopted the Sustainable Development Goals (SDGs) to protect the planet. In this regard, ship designers are exploring advanced technologies to construct efficient ships with low carbon dioxide emissions. The rudder-bulb-fins system (RBFS) is one of the energy-saving technologies by recovering the rotational energy of the propeller slipstream that can fulfil the above-mentioned demands. The propulsive performance of a 1:100 scaled KRISO very large crude oil carrier (KVLCC2) model ship with RBFS system containing the various fin configurations is investigated by comparing the efficiency of the model with the conventional rudder in regular head waves. CFDShip-Iowa V4.5 was utilized for hydrodynamic numerical simulations and the computational results were validated with the available experimental data, which were carried out in the towing tank of Osaka University. The analysis of motions, viscous flow fields, forces, and self-propulsion factors was carried out in five different wavelengths ($\lambda/L=0.6, 0.85, 1.1, 1.35, \text{ and } 1.6$) for the comparison of normal rudder and RBFS and in three wavelengths ($\lambda/L=0.6, 1.1, \text{ and } 1.6$) for investigation of the performance of new fins. The ship's motions response to various types of RBFS was almost similar to a hull without RBFS. From the results of the wake fields, the hub vortex strength was weakened and the high axial velocity field was a bit wider by RBFS as compared to the conventional rudder. Some of the new fins could eliminate the flow separation that occurred in the original rudder fin. The improvement of self-propulsion by all types of RBFS was observed in many wave conditions but the gain was smaller than in calm water and was almost zero in one wave condition for one RBFS. Overall, CFD predicted well and had good agreement with the experiment in self-propulsion performance prediction in waves.

KEYWORDS: Energy-Saving Device, Rudder Bulb-Fins System (RBFS), CFD, Propulsion Performance, Head Waves.

Contents

ACKNOWLEDGEMENT.....	II
ABSTRACT.....	III
NOMENCLATURE.....	VI
LIST OF FIGURES.....	IX
LIST OF TABLES.....	XI
CHAPTER -1- INTRODUCTION.....	- 1 -
1.1 GENERAL BACKGROUND.....	- 1 -
1.2 VARIOUS ENERGY-SAVING METHODS AND DEVICES.....	- 2 -
1.2.1 ESDs by operating zones.....	- 3 -
1.2.2 ESDs by working principle.....	- 3 -
1.3 RUDDER-BULB-FINS SYSTEM.....	- 7 -
1.4 RESEARCHES RELATED TO ESDS.....	- 8 -
1.5 MOTIVATION.....	- 11 -
1.6 STRUCTURE OF THE THESIS.....	- 12 -
CHAPTER -2- GEOMETRY, DESIGN, AND TEST CONDITIONS.....	- 14 -
2.1 GEOMETRY.....	- 14 -
2.2 DESIGN CONCEPT OF RBFS.....	- 17 -
2.3 TEST CONDITIONS.....	- 20 -
CHAPTER -3- METHODOLOGY.....	- 22 -
3.1 COMPUTATIONAL FLUID DYNAMICS (CFD) METHOD.....	- 22 -
3.1.1 Grid Generation.....	- 22 -
3.1.2 Computational domain and boundary conditions.....	- 26 -
3.1.3 Overview of CFDSHIP-IOWA version 4.5.....	- 29 -
3.1.4 Governing equations.....	- 30 -
3.1.5 Turbulence model.....	- 31 -
3.1.6 Free surface.....	- 33 -
3.1.7 Body force propeller model.....	- 33 -
3.2 EXPERIMENTAL FLUID DYNAMIC (EFD) METHOD.....	- 36 -
CHAPTER -4- RESULTS AND DISCUSSIONS.....	- 39 -
4.1 SHIP MOTION ANALYSIS.....	- 39 -
4.1.1 Time history of motions.....	- 39 -
4.1.2 First harmonic amplitude and phase.....	- 44 -
4.2 FLOW FIELD ANALYSIS.....	- 48 -
4.2.1 Flow field measurements.....	- 48 -
4.2.2 Flow field at $x/L=0.96875$	- 51 -
4.2.3 Flow field at $x/L=1.0$	- 58 -
4.2.4 Flow field at $x/L=1.025$	- 66 -

4.2.5 Flow field at $y/L=0$	- 74 -
4.2.6 Flow field at horizontal plane	- 76 -
4.2.7 Visualization of vortex.....	- 78 -
4.3 SELF-PROPULSION ANALYSIS	- 80 -
4.3.1 Effective wake	- 81 -
4.3.2 Thrust and resistance.....	- 83 -
4.3.3 Torque and delivered power.....	- 88 -
4.3.4 Efficiencies.....	- 90 -
CHAPTER -5- VARIOUS FIN'S CONFIGURATIONS	- 95 -
5.1 MOTIVATION	- 95 -
5.2 PHYSICAL GEOMETRY	- 95 -
5.3 TEST CONDITIONS	- 98 -
5.4 RESULTS AND DISCUSSIONS	- 99 -
5.4.1 Motion responses.....	- 99 -
5.4.2 Wake Fields	- 101 -
5.4.3 Self-propulsion factors	- 108 -
CHAPTER -6- CONCLUSION AND SUGGESTIONS FOR FURTHER WORK..	- 112 -
6.1 CONCLUSION	- 112 -
6.1.1 Comparison between a normal rudder and RBFS.....	- 112 -
6.1.2 Various fin's configurations	- 114 -
6.2 SUGGESTIONS FOR FURTHER WORK	- 115 -
REFERENCES.....	- 116 -
APPENDIX.....	- 120 -
LIST OF PUBLICATIONS	- 122 -
CURRICULUM VITAE.....	- 123 -

Nomenclature

Symbol	Description
η_H	Hull Efficiency
ϕ	Level Set Function
$f_{b_i}^*$	Non-dimensional Body-Force Vector
η_0	Open-water Efficiency
\hat{p}	Piezometric Pressure
η_D	Quasi Propulsive Efficiency
η_r	Relative Rotative Efficiency
$-\overline{u_i u_j}$	Reynold Stress Tensor
β_i	Propeller hydrodynamic pitch angle
δ_{ij}	Kronecker delta
A	Wave Amplitude
AOA	Angle of Attack
AP	After Perpendicular
c	Propeller chord length
C_D	Drag Coefficient
CFD	Computational Fluid Dynamics
C_L	Lift Coefficient
CO ₂	Carbon dioxide
C_T	Total Resistance Coefficient
D	Propeller Diameter
DES	Detached Eddy Simulation
DOF	Degree of Freedom
DSME	Daewoo Shipbuilding and Marine Engineering
EEDI	Energy Efficient Design Index
EFD	Experimental Fluid Dynamics

ESD	Energy Saving Device
FP	Forward Perpendicular
Fr	Froude Number
HHI	Hyundai Heavy Industries
IBVP	Initial Boundary Value Problem
ICCT	International Council on Clean Transportation
IHI	Ishikawajima-Harima Heavy Industries
IMO	International Maritime Organization
JMU	Japan Marine United
k	Turbulence Kinematic Energy
k	Wave number
K_Q	Torque Coefficient
K_T	Thrust Coefficient
KVLCC2	KRISO Very Larger Crude Carrier
L	Ship Length
L _{pp}	Length between Perpendiculars
MEPC	Marine Environment Protection Committee
MHI	Mitsubishi Heavy Industries
n	Number of propeller revolution
p	Non-dimensionalized Static Pressure
P	Propeller Pitch
P_D	Delivered Power
PDEs	Partial Differential Equations
P_E	Effective Power
PID	Proportional-Integral-Differential
P_T	Thrust Power
Q_0	Torque in open water test
Q_D	Torque
R	Propeller Radius

R	Resistance under Self-propulsion
R_0	Towing Resistance Without Propeller
RBFS	Rudder Bulb-Fins System
Re	Reynold Number
RENS	Reynolds-averaged Navier-Stocks
r_{hub}	Hub Radius
S	Wetted Surface Area
SDGs	Sustainable Development Goals
SEEMP	Ship Efficiency Management Plan
S_{ij}	Shear Strain Rate
SST	Shear Stress Transport
SURF-BULB	Swept-back Up-thrusting Rudder Fin with Bulb
T	Thrust
t	Thrust Deduction Fraction
T_e	Encounter Wave Period
u, v, w	Velocity Components in X,Y,Z direction
UN	United Nations
URANS	Unsteady Reynolds-averaged Navier-Stocks
V_a	Advanced Velocity
V_s	Ship Speed
w	Wake Fraction
ζ	Wave Elevation
λ	Wavelength
ρ	Density of water
ω	Wave Frequency
ω_e	Encounter Wave Frequency
Ω_{ij}	Vorticity Tensor

List of figures

Fig 1-1 Classification of operating zones of ESDs -----	3 -
Fig 1-2 Wake equalizing duct (www.technava.gr) -----	4 -
Fig 1-3 Grim vane wheel (https://siemshipmanagement.pl/) -----	4 -
Fig 1-4 Propeller boss cap fins (www.greenaward.org) -----	5 -
Fig 2-1 Hull form of KVLCC2-----	15 -
Fig 2-2 Three dimensional perspective view of propeller model-----	16 -
Fig 2-3 Flow field predicted at $x/L = 0.986$ in calm water (Truong TQ, 2019)-----	18 -
Fig 2-4 RBFS in CFD simulation -----	18 -
Fig 2-5 Sketch of rudder bulb-fins system-----	19 -
Fig 2-6 Scaled RBFS model -----	19 -
Fig 2-7 Scaled normal rudder model -----	20 -
Fig 3-1 Overset grid system of KVLCC2-----	24 -
Fig 3-2 Overset grid system around a rudder-----	24 -
Fig 3-3 Computational domain and boundary conditions -----	28 -
Fig 3-4 (a) Schematic of rotating hub boundary condition (b) Rotating vectors on hub---	28 -
Fig 3-5 CFD process -----	30 -
Fig 3-6 Sketch of blade element theory -----	34 -
Fig 3-7 Towing tank of Osaka University -----	36 -
Fig 3-8 KVLCC2 tanker model (Mwangi, 2021)-----	37 -
Fig 3-9 Propeller models (Mwangi, 2021)-----	37 -
Fig 4-1 Comparison of heave and pitch motion time histories at $\lambda/L=0.6$ -----	41 -
Fig 4-2 Comparison of heave and pitch motion time histories at $\lambda/L=1.1$ -----	42 -
Fig 4-3 Comparison of heave and pitch motion time histories at $\lambda/L=1.6$ -----	43 -
Fig 4-4 First harmonic amplitude, phase lag, and mean value of heave motion -----	46 -
Fig 4-5 First harmonic amplitude, phase lag and mean value of pitch motion -----	47 -
Fig 4-6 Positions of flow field computed in CFD -----	50 -
Fig 4-7 Two transverse position of flow field measured in experiment -----	50 -
Fig 4-8 Transverse $x/L=0.96875$ plane of the velocity field measurement -----	51 -
Fig 4-9 Comparison of flow field at $x/L=0.96875$ in $\lambda/L=0.6$ -----	52 -
Fig 4-10 Comparison of flow field at $x/L=0.96875$ in $\lambda/L=1.1$ -----	54 -
Fig 4-11 Comparison of flow field at $x/L=0.96875$ in $\lambda/L=1.6$ -----	56 -
Fig 4-12 Transverse $x/L=1.0$ plane of flow field computation -----	58 -

Fig 4-13 Comparison of flow field at $x/L=1.0$ in $\lambda/L=0.6$ -----	59 -
Fig 4-14 Comparison of flow field at $x/L=1.0$ in $\lambda/L=1.1$ -----	61 -
Fig 4-15 Comparison of flow field at $x/L=1.0$ in $\lambda/L=1.6$ -----	64 -
Fig 4-16 Transverse $x/L=1.025$ plane of flow field measurements -----	66 -
Fig 4-17 Comparison of flow field at $x/L=1.025$ in $\lambda/L=0.6$ -----	69 -
Fig 4-18 Comparison of flow field at $x/L=1.025$ in $\lambda/L=1.1$ -----	70 -
Fig 4-19 Comparison of flow field at $x/L=1.025$ in $\lambda/L=1.6$ -----	73 -
Fig 4-20 Longitudinal $y/L=0$ plane of flow field predicted -----	74 -
Fig 4-21 Comparison of flow field at $y/L=0$ -----	75 -
Fig 4-22 Horizontal plane of flow field computed -----	76 -
Fig 4-23 Comparison of flow field at horizontal plane -----	77 -
Fig 4-24 Illustration of Q-criterion for $Q=500$ colored by the axial velocity contours-----	79 -
Fig 4-25 Open water graph of KVLCC2 propeller by Kishi (2018) -----	80 -
Fig 4-26 Comparison of time history of wake fraction -----	83 -
Fig 4-27 Comparison of time history of thrust-----	85 -
Fig 4-28 Comparison of mean thrust in CFD -----	85 -
Fig 4-29 Comparison of mean thrust in EFD-----	86 -
Fig 4-30 Comparison of computed axial force-----	87 -
Fig 4-31 Comparison of mean value of resistance in CFD-----	88 -
Fig 4-32 Comparison of mean value of resistance in EFD-----	88 -
Fig 4-33 Comparison of torque-----	89 -
Fig 4-34 Comparison of computed hull efficiency -----	92 -
Fig 4-35 Comparison of measured hull efficiency -----	92 -
Fig 5-1 Cut0.005-fin -----	96 -
Fig 5-2 Cut0.007-fin -----	97 -
Fig 5-3 NACA-fin-----	98 -
Fig 5-4 Comparison of heave and pitch motions -----	100 -
Fig 5-5 Comparison of flow field at $x/L=1.0$ in $\lambda/L=1.1$ -----	103 -
Fig 5-6 Comparison of flow field at $x/L=1.025$ in $\lambda/L=1.1$ -----	106 -
Fig 5-7 Comparison of total resistance predicted by CFD -----	108 -
Fig 5-8 Comparison of thrust predicted by CFD -----	109 -

List of tables

Table 1-1 Energy-saving devices and their working principles summarized by Xu et al. --	5 -
Table 2-1 Principle particulars of KVLCC2-----	14 -
Table 2-2 Principle particulars of propeller model -----	16 -
Table 2-3 Main particulars of rudder -----	20 -
Table 2-4 CFD simulation matrix-----	21 -
Table 3-1 Details grid without rudder -----	25 -
Table 3-2 Details grid of rudders-----	25 -
Table 3-3 Boundary conditions-----	27 -
Table 3-4 List of Measuring parameters and devices -----	38 -
Table 4-1 Propeller open water data-----	82 -
Table 4-2 Comparison of delivered power -----	90 -
Table 4-3 Self-propulsion factors computed by CFD -----	91 -
Table 4-4 Self-propulsion factors measured by EFD -----	92 -
Table 4-5 Propeller open water data-----	93 -
Table 4-6 Comparison of propulsive efficiencies-----	94 -
Table 5-1 CFD simulation matrix-----	99 -
Table 5-2 Comparison of self-propulsion factors predicted by CFD -----	110 -
Table 5-3 Comparison of self-propulsion factors measured in experiment -----	111 -

Chapter -1- Introduction

1.1 General Background

Nowadays, the ship designers and shipyards are making efforts the finding solutions to meet the specific customers' needs and will as much as possible. On the other hand, they have been facing consistently many challenges concerned with global energy crises, environmental protection, economic stability, and so on. These are handled and taken control by the international institutes or organizations.

One of the biggest challenges is to meet and follow the carbon dioxide emission regulations implemented by the International Maritime Organization (IMO). It set three terms of regulations; the near-term regulation for the 2020s, the medium-term regulations for the 2030s, and longer-term regulations for the 2050s. The near-term regulation for the 2020s is fairly manageable by using a scrubber and substituting the alternative fuel. However, the medium-term regulations for the 2030s and the longer-term regulations for the 2050s are still difficult to be met.

According to the policy update by the International Council on Clean Transportation (ICCT), it was stated that IMO amended MARPOL Annex VI Regulations to prevent the air pollution made by ships at the 62nd session of the Marine Environment Protection Committee (MEPC). Considered the establishing carbon dioxide standards globally, it had discussed mainly the Energy Efficiency Design Index (EEDI) in the last decade. The requirement of that regulation was for most of the new ships to be 10% more efficient at the beginning of 2015, 20% more efficient by 2020 and 30% more efficient by 2025¹⁾.

In addition to the EEDI regulation, not only shipyards but also ship operation companies are necessary to implement and maintain a Ship Efficiency Management Plan (SEEMP) providing a mechanism for monitoring efficiency performance with time and considering new technologies. Verification of the regulation has been conducted generally in two stages; ship design and sea trial. The ship owner, shipbuilder, and verifier from Maritime Administration or Classification Society) have to involve closely at both stages.

On the other hand, the United Nations (UN) adopted the Sustainable Development Goals (SDGs) to protect the planet, and ensure that by 2030 all people enjoy peace and prosperity. In SDGs, there are seventeen goals including upgrading technology to provide clean, and more efficient energy, mechanisms for raising capacity for effective climate change-related planning

and management, and so forth. In this regard, ship designers are trying to invent efficient, green, and clean ships with low carbon dioxide emissions. Wang et al. proposed a unified framework where how much level of comprehensiveness of sustainability the maritime industries are making efforts. It reports that the maritime industries are contributing to SDG8 (decent work and economic growth), SDG9 (industry, innovation, and infrastructure), SDG11 (sustainable cities and communities), SDG12 (responsible consumption and protection), SDG13 (climate action), and SDG16 (peace, justice, and strong institutions)²⁾.

1.2 Various energy-saving methods and devices

Reduction of the power requirements of a ship without affecting any vessel's operational capability is the target of energy saving methods³⁾. In 2009, IMO provided the energy breakdown mechanisms of propulsion energy on board a small cargo ship in a head sea, Beaufort 6. In that report, a large amount of energy is lost at the stage of delivering to the propeller shaft. As a theory of propulsion system, the delivered power, P_D required by the propeller to obtain the desired speed is expressed by the equation (1).

$$P_D = \frac{R_T V_s}{\eta_D} \quad (1)$$

R_T represents the total resistance of a ship, V_s is the ship speed, and η_D is the quasi propulsive coefficient, which is the efficiency of the propeller operating in the stern of a ship. According to the equation (1), three main factors can be considered to save power. These are reduction of ship speed, minimizing the resistance of ship operating at the same speed, and raising the performance of the propulsor generating the thrust.

In this study, improving the performance of the propulsor to save energy is mainly discussed. The ability of the propeller to generate the thrust depends on the propeller design and the viscous flow field around its vicinity. There are three main components (hull efficiency, open water efficiency, and relative rotative efficiency) in propulsive efficiency. It means that we have three strategies to increase the propeller's performance. To improve the hull efficiency, resistance, thrust, and wake need to be controlled properly. That part of ways to improve hull efficiency will be discussed later. Increasing the propeller diameter, increasing the blade pitch, and adjusting rpm proportionally can enhance the open water efficiency.

1.2.1 ESDs by operating zones

It can be considered that the ESDs are principally operating in the three zones of the hull⁴⁾. Those three zones are defined as Zone 1 (before the propeller), Zone 2 (at the propeller station), and Zone 3 (downstream of the propeller) respectively as demonstrated in Fig 1-1.

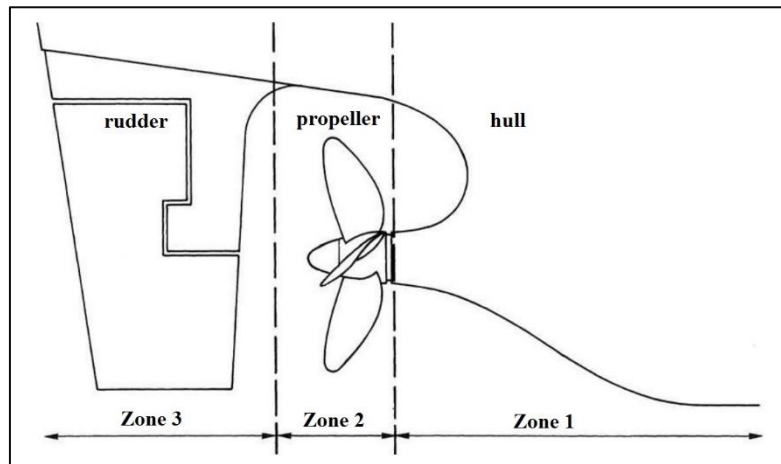


Fig 1-1 Classification of operating zones of ESDs

The energy-saving devices operating in Zone 1 are reacting with the growth of the boundary layer over the stern of the ship so as to obtain some benefit with a more advantageous flow regime. Some examples of ESDs in Zone 1 are wake equalizing duct, asymmetric stern, Grothues spoilers, and semi- or partial ducts.

In Zone 2 and Zone 3, ESDs are running within both the hull wake field and the slipstream of the propeller and thus, it seems that they can control the loss of rotational flow energy. Reaction fins, ducted propeller, nozzle, Grim vane wheels, propeller boss cap fins and rudder bulb fins system can be classified as ESDs working in Zone 1 and Zone 2.

1.2.2 ESDs by working principle

Based on the working principle, ESDs can be distinguished into four types⁵⁾ as shown in Table 1-1. The first type of ESD is the one that can optimize the inflow towards the propeller. The second one is the ESD recovering the rotational energy of the propeller. The third and fourth types are the ones that reduce the separation of the vortex tempted by the ship and new propellers.

A Wake-equalizing duct is a kind of ship hull appendage built in the inflow region of a propeller intended to realign and adjust the velocity of the wake upstream of the propeller disc. Wake velocity may be strengthened, given contra-rotational swirl, accelerated, or a combination of these effects, all of which can increase propeller efficiency, giving either higher thrust or requiring less power for the same thrust.

Introduction

The grim vane wheel is positioned just behind the propeller and its blades have turbine profiles in the inner section while they have the propeller profile in the outer portion. The turbine section takes the advantage of kinetic energy from the propeller slipstream and then transforms it into the additional thrust. The working concept of the vane wheel is to extract energy from the propeller slipstream and convert that energy into an additional thrust improving hull efficiency.

Propeller boss cap fins is one of the ESDs which is mounted at the propeller shaft and downstream of the propeller. It can recycle the rotational wake flow energy in the propeller root region. The blade of the propeller boss cap fins can produce the reverse torque in order to reduce the load of a propeller. The energy saving effects are dependent on the installation angle, the diameter and the longitudinal position along the propeller shaft.

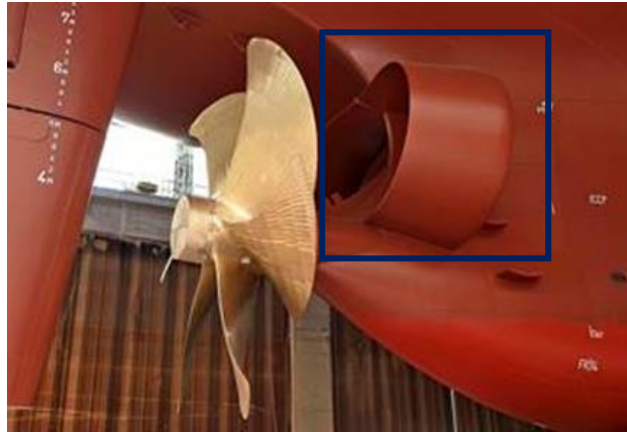


Fig 1-2 Wake equalizing duct (Source: www.technava.gr)

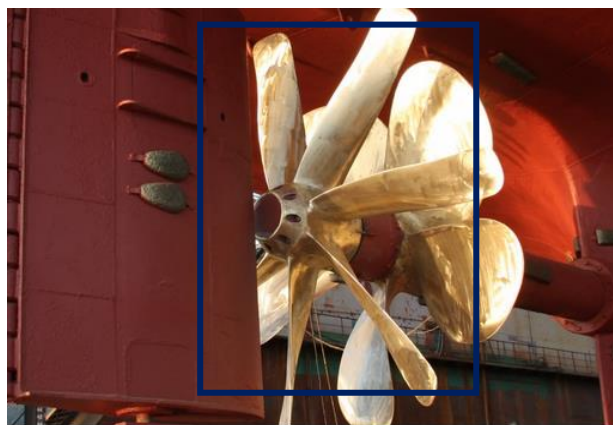


Fig 1-3 Grim vane wheel (Source: <https://siemshipmanagement.pl/>)



Fig 1-4 Propeller boss cap fins (Source: www.greenaward.org)

Table 1-1 Energy-saving devices and their working principles summarized by Xu et al (2017).

Inflow optimization (improve the inflow of propeller and optimize the wake in the stern)		
(1) Wake equalizing duct (fore duct or compensating duct)	<ul style="list-style-type: none"> ▪ Improve inflow velocity and uniform ▪ Reduce flow separation and resistance (especially viscous resistance for large block coefficient ship) ▪ Provide extra thrust 	Firstly applied in bulk carrier 1980
(2) Pre-swirl stator	<ul style="list-style-type: none"> ▪ Make inflow pre-rotate ▪ Recycle rotation energy loss 	
(3) Energy saving shaft strut (with two support arms)	<ul style="list-style-type: none"> ▪ Make the flow have circulation opposite with the rotation of propeller 	
Energy recovery technology of propeller (recovery of rotation energy of the wake of propeller)		
(1) Rudder ball	<ul style="list-style-type: none"> ▪ Cut down the space of low pressure at the axis after the propeller ▪ Reduce circumferential velocity of propeller ▪ Make wake field more uniform 	

	<ul style="list-style-type: none"> ▪ Beneficial to cavitation performance 	
(2) Thrust fins	<ul style="list-style-type: none"> ▪ Turn rotational energy of flow after propeller into thrust 	<ul style="list-style-type: none"> • Installation angle • Length of the fins
(3) Grim vane wheel	<ul style="list-style-type: none"> ▪ Turn rotational energy of flow after propeller into thrust ▪ Reduce pulsating pressure about 40-50% so as to weaken shaking of hull 	Originated in 1960
Reduction or Separation of the vortex		
(1) Propeller boss cap fins	<ul style="list-style-type: none"> ▪ Eliminate propeller vortex ▪ Recover the pressure of the boss and cap ▪ Increase thrust ▪ Provide opposite torque to reduce the whole torque of the propeller ▪ Reduce torque, vibration, underwater noise and rudder erosion 	Payback time is 6 months
New propeller		
(1) Contra-Rotating Propellers (aft propeller diameter is smaller than frond propeller)	<ul style="list-style-type: none"> ▪ Rear propeller absorb rotation energy of wake flow of front propeller ▪ Wake flow of the rear propeller does not exist circumference induced velocity 	<p>Ships with heavily loaded propellers (very fast cargo vessel like Ro-Ro ship, container ship)</p> <ul style="list-style-type: none"> • Rotating speed ratio • Blade numbers • gap

1.3 Rudder-bulb-fins system

The current study is about the rudder-bulb-fins system (RBFS), which is one of the hydrodynamically based ESDs improving hull efficiency. It can contribute to the SDGs and achieve some amount of the required EEDI index. The rudder bulb is mounted on the leading edge of the airfoil-shaped rudder blade at the center of a propeller hub for the purpose of modification of the hub vortex. RBFS can reduce the space of low pressure at the axis after the propeller and intensify the rectification of the rudder and lessen the circumferential velocity of a propeller. The propeller viscous wake field can be made uniform by RBFS and thus it gives the benefit of the cavitation performance of the propeller. The main hydrodynamic effectiveness of the rudder bulb can be described as follows.

- Alleviation of the contraction of flow the downstream of a propeller
- Mitigation of a propeller hub vortex
- Making the wake distribution uniform to some extent and improvement of hull efficiency by wake gain

The rudder fin is a kind of thrust fin fitted on both sides of the rudder and may have an opposite installation angle according to the direction of the inflow. When the airfoil-shaped fins are installed downstream of a propeller, it is sure that the lift force can be generated since they are working in the helical slip-stream of the propeller, and thus get flow at incidence. In that phenomenon, the axial component of this lift force will transform as the additional thrust. Therefore, the design of the fin should be optimized based on its lift-drag ratio while operating in the slipstream of the propeller. In addition, the fatigue behavior needs to be considered in designing the rudder fins because they are operating within the flow variations caused by the vortex sheets originating from the propeller.

RBFS cannot retrofit the rudder of the existing vessel. For that reason, a new rudder must be designed. The rudder bulb can be built by the traditional technology and the investment cost is not very high. The estimated payback time is a medium around 10 years. It can be set up easily in most types of the vessel except ferries and cruises (tanker, bulk carrier, container, and Ro-Ro ships). Crist stated that efficiency under normal conditions can be improved by about 4% by rudder bulb⁶. RBFS is quite compatible with other ESDs. Therefore, it can be used in combination with either wake equalizing duct or nozzle⁴.

1.4 Researches related to ESDs

Various studies on the performance of ESDs around marine propeller have been conducted numerically and experimentally in the recent years. Matsumoto and Sakamoto (2009) filed a patent of finned rudder⁷⁾. The starboard side fin was located lower than the center position of the propeller and portside one was higher. One type of portside fin was designed with an upward inclination. The fin tips were inside propeller radius. It reported that fuel consumption can be reduced about 2%. South Korea's Daewoo Shipbuilding and Marine Engineering (DSME) Company had developed rudder bulb fin in 2011 and the maximum possible power reduction achievable with ESDs was in the range of 3% - 4% (Mewis, 2013)⁸⁾.

The Rudder-bulb-fin system had been developed by Kawasaki Heavy Industries, comprising of a large bulb, having a diameter of 30- 40 percent of the propeller diameter, which was installed on the rudder close behind the propeller boss. Kawasaki heavy industries, Ltd had constructed more than 100 ships with RBS-F (Rudder Bulb System with Fins). The power saving achievement was around 2-7%. JMU (Japan Marine United Corporation) invented SURF-BULB (Swept-back Up-thrusting Rudder Fin with Bulb). About 3-5% fuel consumption can be cut by converting the rotational energy behind a propeller to the thrust force.

In the design of IHI (Ishikawajima-Harima Heavy Industries Co., Ltd) and HHI (Hyundai Heavy Industries), horizontal fins were attached on the rudder horn. The fuel consumption reduction up to 6% at best was claimed by HHI for the fins with some angle of attack. MHI (Mitsubishi Heavy Industries) developed a stator fin behind the propeller on the rudder horn using advanced panel method. Model and full scale experiment were conducted for propulsion, cavitation, and strength and vibration test (Hoshino et al., 2004)⁹⁾. Lately, Kawakita et al. (2012) performed the viscous flow simulation with cavitation model to analyze detailed flow field around the hull, stator and propeller¹⁰⁾. It was enables a detailed flow field characteristics and pressure distributions around the propeller.

Okada et al. (2015) performed the research on the development of ultimate rudders with small and large diameter of rudder bulb for bulk carrier by using a commercial CFD code, SOFTWARE CRADLE SCRYU/Tetra Ver.10¹¹⁾. The improvement of efficiency by CFD analysis was 3.5% at ultimate rudder with small diameter and was 4.1 % at ultimate rudder with large diameter compared with the normal rudder. Nielsen et al. (2012) studied the improvement in efficiency of Kappel propeller with rudder bulb systems by using CFD analysis and validated against experimental model test¹²⁾. The Kappel propeller with rudder bulb has

Introduction

shown improvement of 9.3% in propulsive efficiency compared to conventional propeller without rudder bulb.

Kim et al. (2014) studied a Z-twisted rudder with bulb and fins for a 320m long container ship at 20 knots by viscous simulation. The turbulence model was Reynolds stress model. They pointed out that the rudder bulb should not be installed together with contra-rotation propeller and propeller boss cap fin. The bulb fin not only improved the effective wake but gained extra thrust raising the propulsive efficiency 2.95% as well¹³).

Li et al. (2014) studied the interaction between the rudder and the propeller as well as the influence of the size of the rudder ball on the propeller efficiency. It was concluded that the ratio between the rudder ball and the propeller existed a best number¹⁴). Yan et al. (2014) analyzed the efficient rudder ball and fin stabilizer on a container ship under open water condition. The results revealed that combination using of the rudder ball and fin stabilizer could bring about better energy-saving effect¹⁵).

Chen et al. (2015) compared the oil tanker model with or without the bulk ball. It drew the conclusion that for each diameter of the propeller, there remained a best diameter for the bulk ball where the bulk ball could show the best energy-saving efficient. In addition, while the gap between the propeller and the bulk ball was determined, the longer the bulk ball was, the more thrust it would produce¹⁶). Wang et al. (2013) performed an analysis of the hydrodynamic performance of the propeller-rudder-rudder-ball system on a 42 meter long trawler with duct rudder. Because of the exist of the duct, the energy saving effect of the rudder ball would increase first, then decrease, then increase again and then decrease along with the increase of the advance coefficients. Two peaks and one trough was shown in the curve of the energy saving effect¹⁷).

Hu et al. (2016) investigated the energy saving efficiency gained by rudder thrust fin on a bulk carrier using CFD method. It drew the conclusion that the thrust fin could absorb the wake energy, increase the thrust of the propeller, reduce the resistance of the hull and bring about 2.3% energy-saving¹⁸). Wang et al (2016) calculated the hydrodynamic numerical result of the ship-propeller-rudder system with or without thrust fin on a 75000 tones ship model. The numerical result showed that the thrust fin was beneficial to the increase of the propeller efficiency in the hydrostatic test and the motion test¹⁹).

Shin et al. (2018) studied the rudder bulb performance in the maneuvering of a Ro-Ro ship. The comparison between simulation results with and without rudder bulb in rudder

Introduction

turning conditions showed that the efficiency gain of the rudder bulb is maintained over 10 degree rudder angles and the rudder effectiveness at a certain turning moment is improved in the whole considered range of rudder angles by adding rudder bulb²⁰). Shen et al. (2016) performed the analysis of scale effects of rudder bulb and rudder thrust fin on propulsive efficiency of bulk carrier. The numerical results demonstrated that the energy gains predicted at model scale are more than twice those predicted at full scale²¹).

Tacar et al. demonstrated experimentally and numerically the effect of the gate rudder system that improve propulsive efficiency of 14% in sea trial on the powering performance of a 2400 DWT container ship in two different model scales. Concerned with the scale effect, the smaller model size over-predicted the required power but the larger model under-predicted it²²). The interaction mechanism between the hull, pre swirl stator and rudder bulb was analyzed by Su et al. The computational results was verified by comparing the test results of 25m long scaled ship model in the actual sea conditions. The average efficiency gain of up to 3% was obtained²³). It also confirmed that rudder bulb can optimize the hub vortex and make the pressure distribution more uniform so that the course stability of the ship can improve.

Obwogi et al. investigated the effects of rudder bulbs and rudder fins on the performance of a 35000DWT bulk carrier using numerical simulations STAR CCM+ and model tests. It was noted that the energy improvement increases with the increase in the bulb diameter from 0.2D (diameter of propeller) to the maximum at the diameter of 0.3D and drops afterwards. The energy-saving at the optimum diameter was 2.03%. The optimal thrust fin was at a span of 0.6D, the chord length of 0.3D, and zero angle of attack. The energy-saving effect at these optimum parameters was 2.63%²⁴). Kim et al. proposed a design optimization of ESD combined duct and pre swirl stator fins for a standard VLCC. It was concluded that the combination of these two ESDs improved the propulsive performance not only in model scale but also in full scale. The optimized ESD could increase the power saving from 1.9% to 3.2% in full scale²⁵).

Truong et al. (2016) carried out the Experimental Fluid Dynamics (EFD) and CFD study of the bulbous rudder with asymmetric horizontal fins with various angles of attack in still water condition. The installed angle of fin around -2 to 1 degree with 1-degree increment for the fins on the both starboard and port sides had been done to search the best energy efficient fin. It was stated that the best angle of attack had been found at zero degree for port side and minus one degree for starboard side. At that best angle of attack position, very small flow

separation near the root and large flow separation near the tip were observed. The rudder bulb fins system (RBSF) showed the lower resistance and higher self-propulsion performance than the normal rudder in calm water condition²⁶). They also performed the modification of rudder fin configurations by adjusting the span length and root camber profile in calm water^{27, 28}).

Mwangi et al. (2021) studied the effect of energy saving devices (ESDs) on the forces, motions and flow field around the stern of KVLCC 2 using Experimental Fluid Dynamics method in regular head waves of $\lambda/L=0.6, 0.85, 1.1, 1.35$ and 1.6 with an amplitude of $0.03m$. It was concluded that RBF-F system was able to attenuate the hub vortex strength in the propeller slipstream due to its bulb and fins and it could improve the effective wake in waves²⁹).

1.5 Motivation

Over the last few years, with the increase in fuel price as well as the fuel shortage and global warming, marine propulsor with higher efficiency are being demanded. Therefore, ship designers have been focusing on optimizing the existing solutions and researching new designs for the last decade. Consequently, many types of ESDs have been explored continuously by using the various methodological approach. Most of these researches were carried out in calm water conditions but the study on their performance in wave conditions has not been observed yet. In the hydrodynamic performance of the ship, the role of the wave and ship body interaction is considerably influent and thus power-saving of ESDs can be different in waves although it is favorably effective in calm water.

From the aspect of the design concept, it must be emphasized that design is targeted at good performance not only for the model test or trial condition in the calm sea but also for the service conditions with wind and waves as the ship may encounter the various phenomenon of weather conditions in the actual sea state. Moreover, the performance of ESDs in both ideal conditions and operational conditions is essential to be proved by international organizations. Besides that, the detailed flow fields, and interrelation between ship, propeller, rudder, and ESD should be fully understood.

The objective of this dissertation is to contribute to the above requirements through Computational Fluid Dynamics (CFD) analysis and Experimental Fluid Dynamics (EFD). In this research, the targeted type of ESD and hull form are RBFS and 1/100 scaled KVLCC2 tanker model. The predictions of motions, the viscous flow field around the propeller, forces and propulsive efficiencies of KVLCC2 without rudder, with normal rudder, and with RBF system were predicted using CFD to check the influence of the rudder and rudder with ESD on

the propulsive performance in waves. The validation with available experimental data was carried out properly. The RBFS used in this current study has been approved and validated in calm water. Hull efficiency improvement of 3.6% at CFD and 7.3% at EFD was investigated by Truong et al.

1.6 Structure of the Thesis

The thesis is comprised of six chapters in total.

The dissertation begins with an introduction that consists of general background concerned with current environmental regulations, various energy saving devices (ESDs), some literature reviews on ESDs, and motivation for this study. In the general background, currently facing problems around the world with ship design, types of energy-saving devices and the working principle of rudder bulb-fins system are briefly explained.

Chapter 2 consists of two parts; geometry and test conditions. In the first part, the principle particulars and diagrams of the objective ship, propeller, and rudder are shown. The second part represents the summary matrix of the simulations conducted in five wavelengths ($\lambda/L = 0.6, 0.85, 1.1, 1.35, \text{ and } 1.6$).

Chapter 3 is about the methodology composed of two sections; namely as Computation Fluid Dynamics (CFD) and Experimental Fluid Dynamics (EFD). In the first section, details of the generated grid, an overview of CFDSHIP-IOWA, and adopted computational domain and boundary conditions are described. The second section gives a brief explanation of the experimental setup and measurements.

In chapter 4, the results and discussion on the comparison of RBFS and normal rudder are stated by dividing into three sections; motions analysis, viscous flow fields, and self-propulsion analysis. In motion analysis, two degree of freedom motions (heave and pitch) are discussed including the first harmonic analysis. The axial velocity fields predicted at three longitudinal positions (upstream of a propeller, AP, and downstream of rudder), single transverse, and horizontal positions are illustrated in section 2. The 3D vortex flow comparison is also shown in the second section. In the final section of chapter 4, graphs and tables of effective wake, thrust, resistance and efficiencies ($\eta_H, \eta_o, \eta_r, \text{ and } \eta_D$) are demonstrated. The time history comparison of motions, forces and effective wake is presented as well. The validation against EFD results in each case is performed.

Introduction

Chapter 5 shows the simulations of new fins modifying span length, root camber profile and angle of attack in three wavelengths ($\lambda/L = 0.6, 1.1, \text{ and } 1.6$). Comparison of those newly designed fins and original fin is carried out from the aspect of motion, flow field and self-propulsion analysis with the aid of graphs and tables. The comparison of the time history of motions and forces in one to three encountered periods is also included.

The summary of the entire work performed is described with the specific and remarkable facts from each and single section in chapter 6. The suggested works that should be done in the future are mentioned.

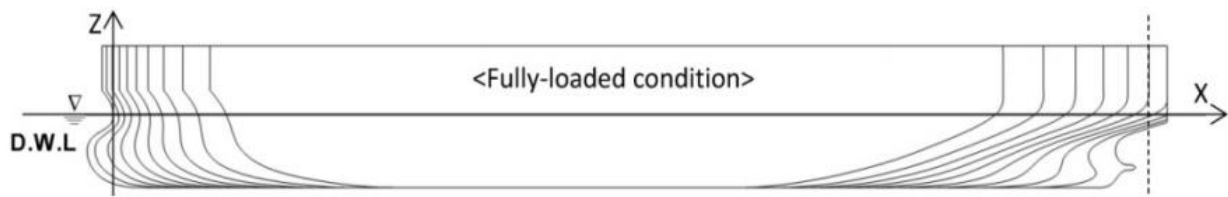
Chapter -2- Geometry, Design, and Test Conditions

2.1 Geometry

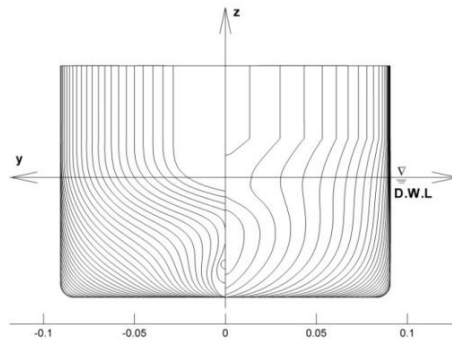
All the studies are performed for a 1/100 scale model of KRISO very large crude oil carrier KVLCC2 tanker appended with a propeller dummy hub and rudder in the fully loaded condition. The main particulars of full-scale ships are provided in Table 2-1. Fig 2-1 demonstrates the lines plan (profiles and body plan) and 3-D perspective view of KVLCC2. The coordinated system is fixed at a forward perpendicular (FP), with the x-axis pointing toward aft perpendicular (AP), the y-axis toward the starboard side, and z axis pointing upward. The length between perpendiculars of the ship model is 3.2m and its block coefficient is 0.8098. The mid-ship section of KVLCC2 is almost rectangular with a coefficient of 0.998. These studies are conducted at Froude and Reynolds numbers of $Fr = 0.142$ and $Re = 2.546 \times 10^6$ corresponding to 15.5 knots (7.967 ms^{-1}), the design speed of the full-scale ship.

Table 2-1 Principle particulars of KVLCC2

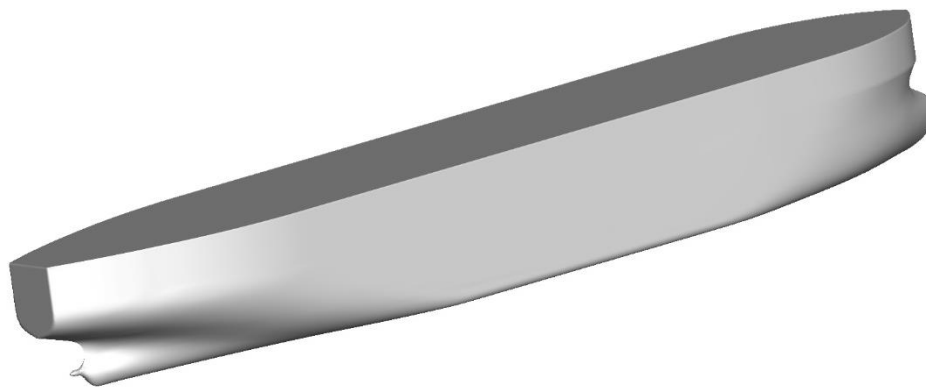
Main particulars of ship		Full scale	Model Scale
Length between perpendiculars	L_{PP} (m)	320.0	3.2
Length of waterline	L_{WL} (m)	325.5	3.255
Maximum beam of waterline	B_{WL} (m)	58.0	0.58
Depth	D (m)	30.0	0.3
Draft	T (m)	20.8	0.208
Displacement	Δ (m^3)	312622	0.312622
Wetted area w/o rudder	S_W (m^2)	27194	2.7194
Wetted surface area of rudder	S_R (m^2)	273.3	0.02733
Block coefficient (CB)	$\Delta / (L_{PP} B_{WL} T)$	0.8098	0.8098
Midship section coefficient (CM)		0.9980	0.9980
LCB (% L_{PP}), fwd+		3.48	0.0348
Vertical Center of Gravity (from keel)	KG (m)	18.6	0.186
Metacentric height	GM (m)	5.71	0.0571
Radius of gyration for rolling	K_{xx}/B	0.40	0.4
Radius of gyration for pitching and yawing	$K_{yy}/L_{PP}, K_{zz}/L_{PP}$	0.25	0.25



Profile view



Body plan



3-D perspective view

Fig 2-1 Hull form of KVLCC2

Table 2-2 provides information about the main particulars of the propeller model and Fig 2-2 is the 3-D perspective view of the propeller model. The type of propeller is a fixed pitch propeller and the number of blades is four. The propeller used in the experiments rotates in the clockwise direction with the rotational speed of 16.5 rps, which is measured at the model point of the ship with the normal rudder in calm water. That is a little different in CFD

simulations where the propeller rotational speed was set to 16.3 rps, revolution at the model point of a ship with RBF system in calm water.

During the self-propulsion experiments, an additional towing force was taken into account to get the self-propulsion point in waves. The number of revolutions was kept for all wave conditions because the loading effect on the wake fraction can be avoided by keeping a similar loading value. As a consequence, the resistance with propeller and thrust were not balanced. The reason for doing that is to verify the wake fraction changes due to waves at similar loading as the increase of effective wake coefficient($1-w_e$) can be explained by the increase of loading. In fact, the ship point should be used to be more practical by considering the skin friction correction for the full-scale ship. However, the propulsion test in ship point has not been conducted yet.

Table 2-2 Principle particulars of propeller model

Type	Fixed Pitch
Diameter (m)	0.0986
Expanded blade area ratio	0.431
Rotation direction	Clockwise
Boss ratio	0.155
Number of blades	4
P/D (0.7R)	0.721

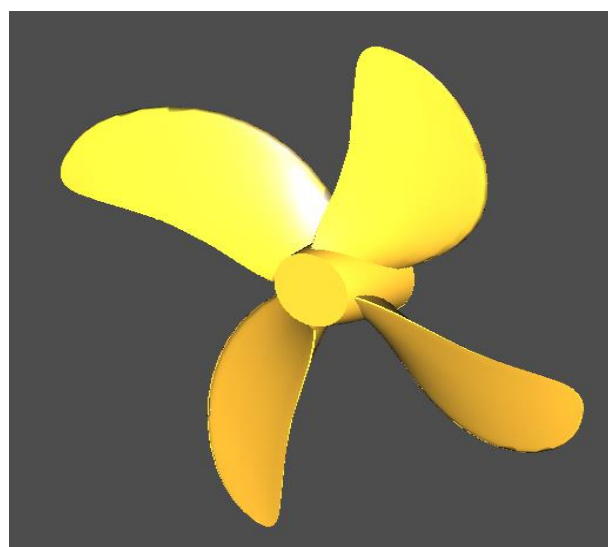


Fig 2-2 Three dimensional perspective view of propeller model

2.2 Design concept of RBFS

The conceptual design of RBFS was mainly based on the theory of flow over immersed body and the characteristic of the flow field downstream of a propeller. Fig 2-3 shows the contour of the z component velocity profile and cross-flow vector predicted at $x/L = 0.986$, which is the cross-section just after the propeller in calm water³⁰). The red colored contour means the upward flow and the blue colored one represents the downward flow. The flow after passing through the propeller goes upward on the port side and downward on the starboard side. This is owing to the rotational direction of the propeller. Taking the advantage of this phenomenon, the camber of the starboard side fin sets downward and that of the port side one is upward to generate the thrust in the forward direction as shown in Fig 2-4.

Bernoulli's Theorem explains lift as a consequence of the airfoil-shaped fin's curved upper surface. Due to this curvature, the air travelling across the top of the wing passes faster than that of the bottom flat surface. The velocity and pressure are inversely proportional to each other. Therefore, the pressure on the bottom surface is higher than that of the top surface. This pressure difference generates the lift force, which can be decomposed into a horizontal component as thrust. The magnitude of this lift force is highly dependent on the angle of attack between the chord line and the water flow direction. In this section, the rudder fins on both sides are horizontal and have no inclination as demonstrated in Fig 2-4. The performance in the wave of rudder fin modified based on the flow field in calm water will be discussed in chapter 5.

Table 2-3 shows the principal particulars of the rudder and Fig 2-5 represents the sketch of the rudder bulb fins system. The ratio of the diameter of the bulb and propeller is 0.223, and the total span length is 6.902×10^{-2} m on the model scale. Fig 2-6 and Fig 2-7 illustrate the 1/100 scaled normal rudder and RBFS models used in the experiment.

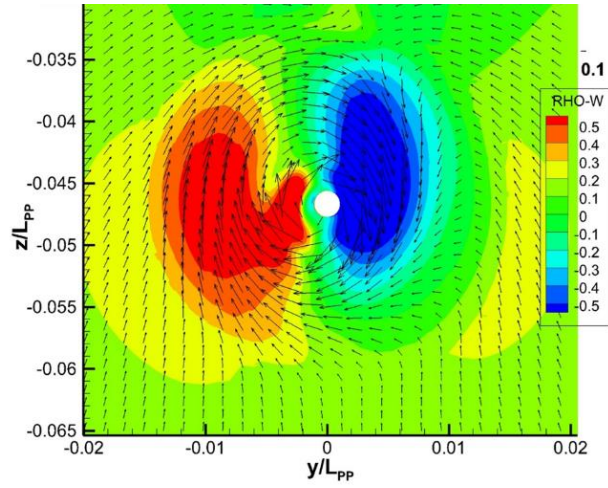
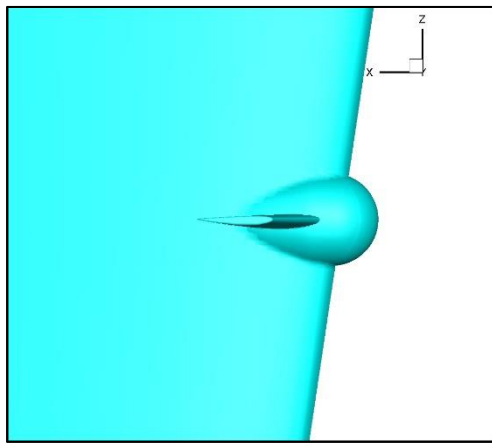
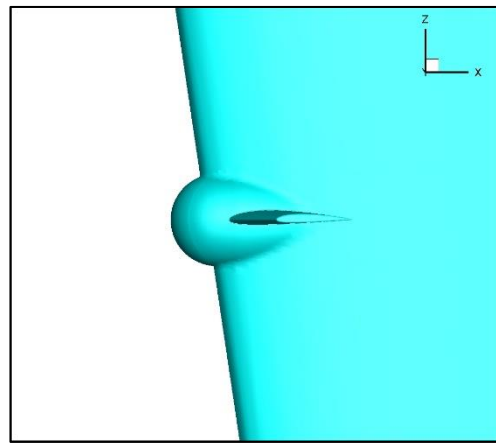


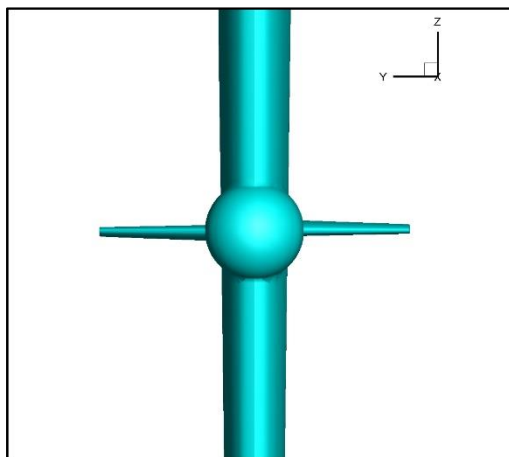
Fig 2-3 Flow field predicted at $x/L = 0.986$ in calm water (Truong TQ, 2019)



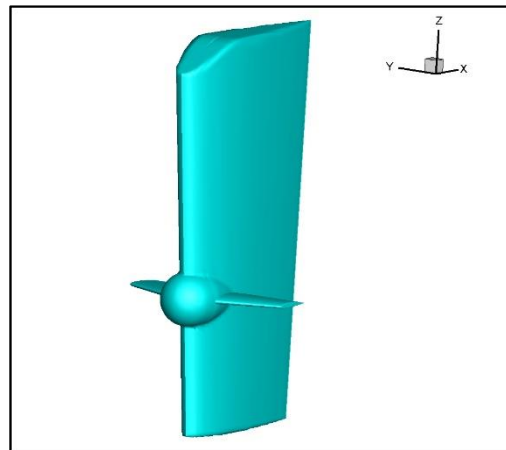
Right side



Left side



Front view



3-D view

Fig 2-4 RBFS in CFD simulation

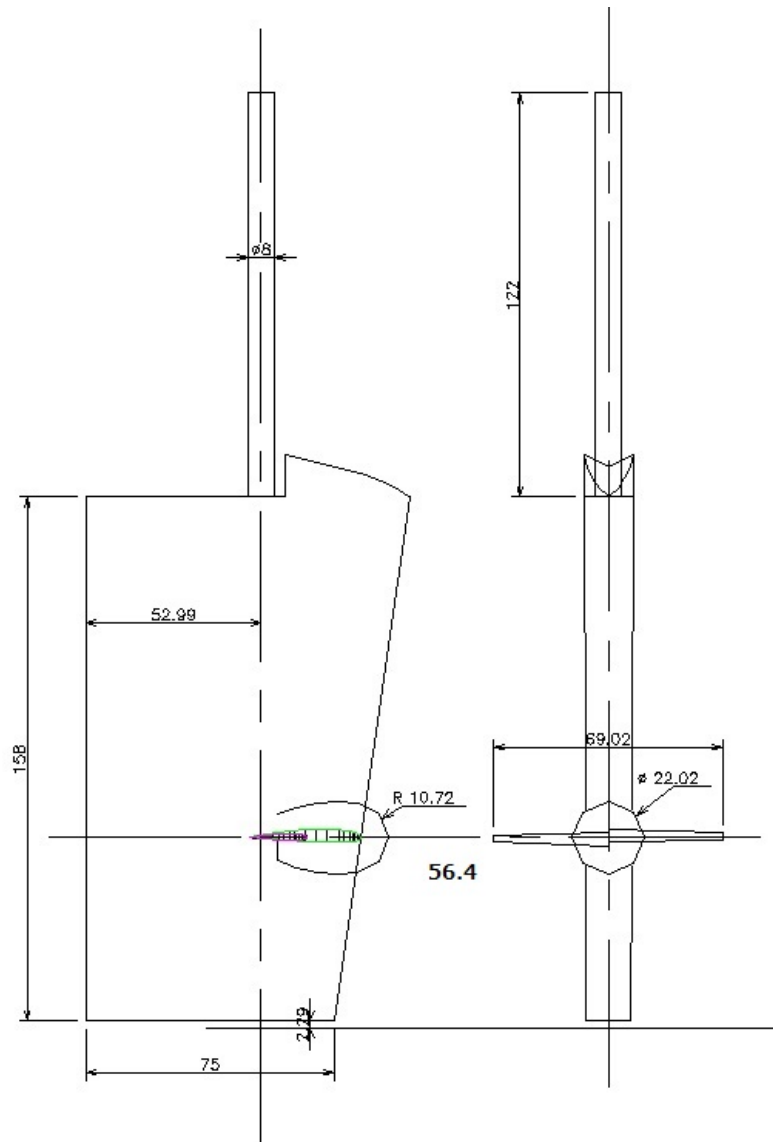


Fig 2-5 Sketch of rudder bulb-fins system



Fig 2-6 Scaled RBFS model



Fig 2-7 Scaled normal rudder model

Table 2-3 Main particulars of rudder

Type	Horn
Surface area of rudder (m ²)	273.3
Lat. area (m ²)	136.7
Turn rate (deg/s)	2.34

2.3 Test conditions

A real sea normally possess the characteristics of irregular wave, but irregular wave can be transformed by the combination of several types of regular wave. For the first time of challenge in waves, investigation of ESD's performance in the regular head wave was decided. A wide range of wavelengths ($\lambda/L = 0.6, 0.85, 1.1, 1.35, \text{ and } 1.6$) was covered in both computational and experimental analysis. In each type of wavelength, the wave amplitude is 3cm. In this study, the influence of wave height is not the main target and 6cm wave height was decided on at the very first time holding the CFD Workshop in Gothenburg in 2010 for the case of a ship without propeller conditions and many researchers also used this value in most of the KVLCC2's simulations. Therefore, I selected the same one for this study. There are 30 total simulations in two conditions; namely towing (without propeller) and self-propulsion (with propeller) for three cases; a ship without a rudder, a ship with a normal rudder and a ship with RBFS. The summary of all the simulated conditions was provided in Table 2-

4. The simulations considered two degree of freedom motions (heave and pitch). In the experiment, heave, pitch, and surge motions were taken into account.

Table 2-4 CFD simulation matrix

Wave conditions	Types of rudder	Test conditions (propeller)
$\lambda/L=0.6, A=3\text{cm}$	No rudder	w/o
		w/
	Conventional	w/o
		w/
	RBFS	w/o
		w/
$\lambda/L=0.85, A=3\text{cm}$	No rudder	w/o
		w/
	Conventional	w/o
		w/
	RBFS	w/o
		w/
$\lambda/L=1.1, A=3\text{cm}$	No rudder	w/o
		w/
	Conventional	w/o
		w/
	RBFS	w/o
		w/
$\lambda/L=1.35, A=3\text{cm}$	No rudder	w/o
		w/
	Conventional	w/o
		w/
	RBFS	w/o
		w/
$\lambda/L=1.6, A=3\text{cm}$	No rudder	w/o
		w/
	Conventional	w/o
		w/
	RBFS	w/o
		w/

(w/o = without propeller and w/ = with propeller, Conventional = conventional rudder, and RBFS = rudder-bulb-fins system)

Chapter -3- Methodology

3.1 Computational Fluid Dynamics (CFD) Method

3.1.1 Grid Generation

Grid generation is a part of pre-processing in CFD simulation, which occupies roughly 50% of the whole work. Hence, it is the most time-consuming part of the CFD work process. Mesh generation was carried out by Pointwise Grid generation software (Gridgen) and the necessary boundary conditions are set within the software³¹). The present grid composition used the same topology as the grid made by Sadat Hosseini et al (2013), which had been completely verified and validated for KVLCC2³²).

The structured grids are utilized together with multi-block overset techniques to reduce the grid generation complexity. The advantages of structured grids are high grid quality, fast calculation time, low memory consumption, and good equations solving system. On the other hand, it has the disadvantages of being difficult to generate mesh for complex geometries and high engineering time to generate it. Moreover, sometimes it is relatively hard to make the local refinement. The grid may consist of a combination of different cell types. In this study, pure hexahedron mesh is used. Each structured grid node can be defined by a unique index (i, j, and k). Consequently, it readily accommodates high-order discretization schemes so that the spatial accuracy can be enhanced³³).

The overset interpolation information between each block is defined in the SUGGAR library, which is originally developed by IIHR, the University of Iowa. Multi-block techniques use topological interconnections to connect the faces of the blocks. This can be done using overset or overlapping techniques, where the interpolation is applied to local cell volumes and faces. These interpolation schemes can be applied dynamically to form transient moving and sliding grids to account for the relative motions of the ship hull and the rotation of the propulsion system. Some solid surface interpolation points will be cut out by SUGGAR and those that will not be in the computation are defined as ghost cells and Panel Weights Programs are used to determine the ghost cell size for the whole domain.

The whole computational domain consists of eleven blocks in the case of the conventional rudder and 15 blocks (4 additional blocks; fin and tip blocks for port side and starboard side of rudder) in the computation of RBFS. The blocks in the simulation of the conventional rudder are hull boundary layer blocks (port and starboard), stern blocks (port and starboard), propeller block, hub blocks (port and starboard), rudder blocks (port and starboard),

Methodology

wake refinement block and background block. The propeller block is created for a body force propeller model. The purpose of making a wake refinement block is to be able to capture the better flow field resolution around the rudder, in which velocity fields are complicated and the gradients seem to be high. The background block is constructed appropriately extending to the far field to define the boundary conditions in that region.

The choice of grid topology is usually based on the nature of the geometry and on consideration of which part or features of the flow fields are important³³). In the present study, all the blocks are comprised of O-grid topology except the wake refinement and background blocks.

The total number of grid points within the boundary layer should be determined by the level of accuracy required, the selected turbulence model, and whether the wall functions are used or not³³). Since the wall function is not used in this research, the non-dimensional grid size normal to the hull surface is taken as 1×10^{-6} to capture the boundary layer and turbulence. A fine resolution cell expansion factor of 1.1 is used near the boundary layer of the wall so that the flow in that area can capture as accurately as possible, where the high-velocity gradients are expected. The grid is generated carefully around the free surface to capture the wavelength and wave height and also to avoid strong numerical dissipation on wave propagation. The grid points along the x-axis are nearly 80 points per wavelength and along the z-axis is about 15 points per wave amplitude.

The computational overlapping and combined grid blocks are illustrated in Fig 3-1. In Fig 3-2, the grid system around the rudder is illustrated. The detailed grid point without rudder blocks and grid topology is presented in Table 3-1. Table 3-2 shows the grid points of rudder blocks in detail. There are about 9 million grid points in total in the computation of RBFS. Nearly 1 million grid points are applied in making the rudder blocks of RBFS while there are about 0.3 million grid points in normal rudder blocks.

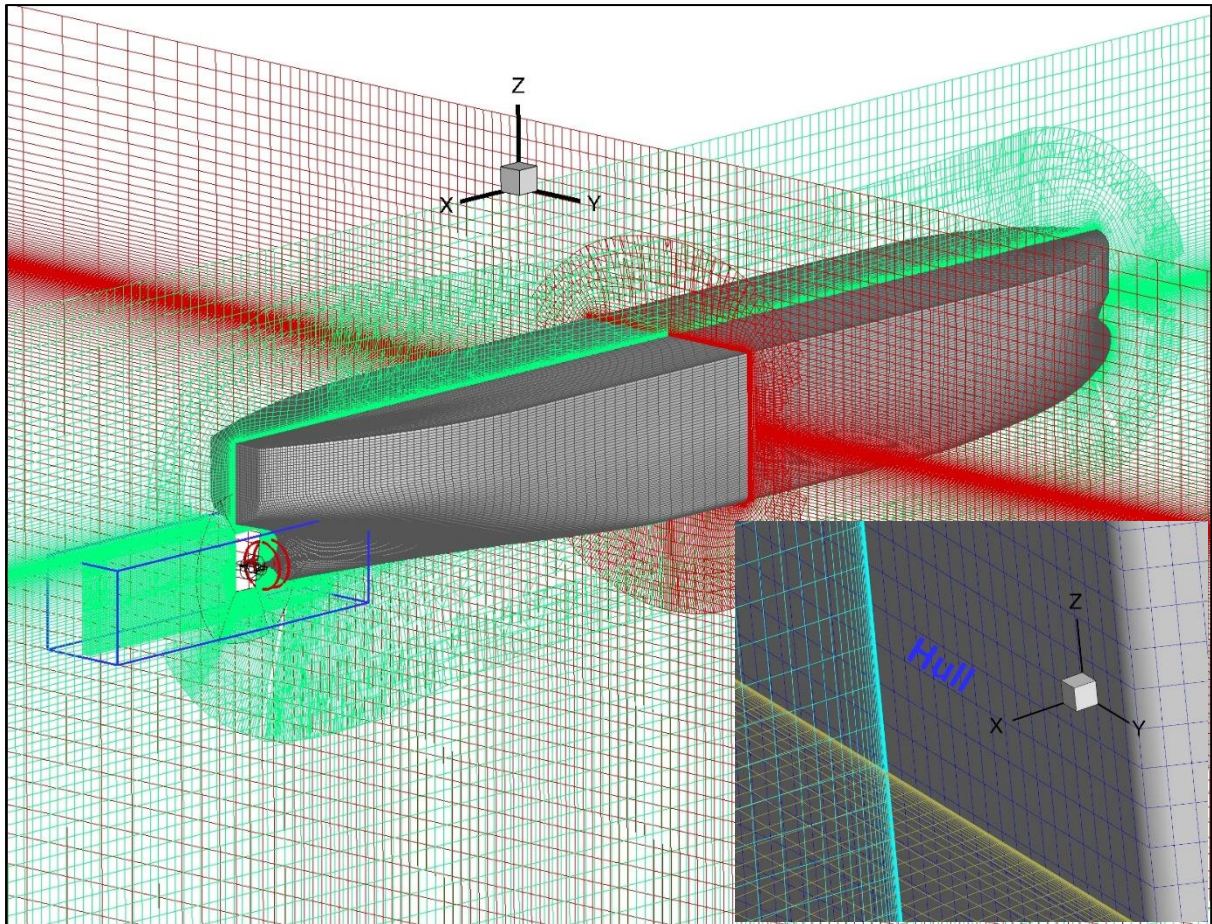


Fig 3-1 Overset grid system of KVLCC2

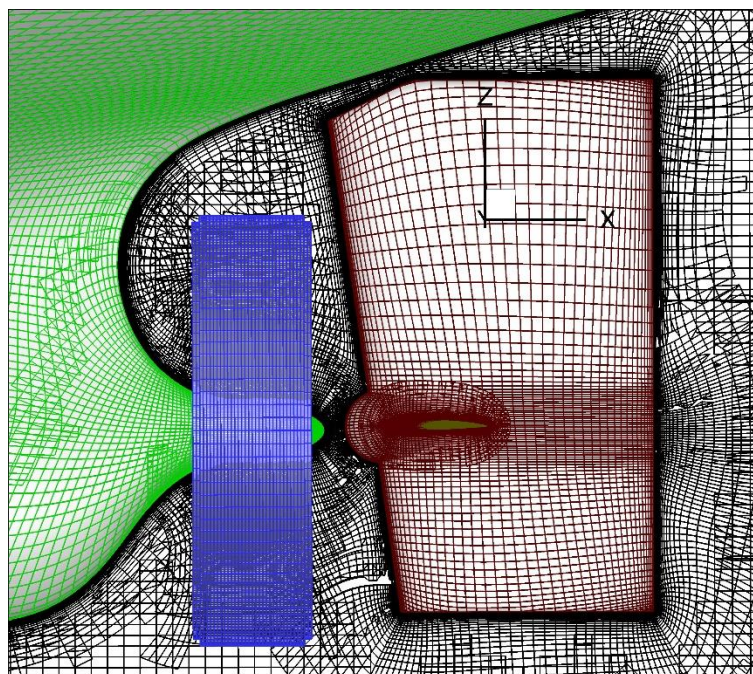


Fig 3-2 Overset grid system around a rudder

Table 3-1 Details grid without rudder

Block name	Topology	$i_{max} \times j_{max} \times k_{max}$	Grid points
Boundary Layer (stb)	O-grid	154×50×144	1,108,800
Boundary Layer (p)	O-grid	154×50×144	1,108,800
Stern bulb (stb)	O-grid	55×50×40	110,000
Stern bulb (p)	O-grid	55×50×40	110,000
Hub (stb)	O-grid	55×50×40	110,000
Hub (p)	O-grid	55×50×40	110,000
Propeller	O-grid	35×111×105	407,925
Background	H-grid	216×121×151	3,946,536
Wake Refinement	H-grid	151×81×81	990,711
Total grid number			8,002,772

Table 3-2 Details grid of rudders

Normal (Star)	44	43	70	132440
Normal (Port)	44	43	70	132440
Rudder (Starboard)	44	45	97	192060
Rudder (Port)	44	45	97	192060
Fin(Starboard)	101	42	56	237552
Tip	101	37	17	63529
Fin(Port)	101	42	56	237552
Tip	101	37	17	63529
Total number of grid in normal rudder				264,880
Total number of grid in RBFS				986,282

3.1.2 Computational domain and boundary conditions

The external flows, in which the fluid does not have the physical boundaries are involved in ship hydrodynamics. In that case, the computational domain representing the volume of fluid to be modelled should be enclosed by additional surfaces. In this research, the rectangular box-shaped computational domain was considered. The non-dimensional computational domain which described in Fig 3-3 with boundary conditions is a rectangular prism extending from $-0.5 < x < 2.35$, $-1 < y < 1$, $-1 < z < 0.22$ for $\lambda/L = 0.6, 0.85$, and 1.1 cases and $-1.5 < x < 2.35$, $-1 < y < 1$, $-1 < z < 0.22$ for $\lambda/L = 1.35$ and 1.6 cases in dimensionless coordinates based on ship length. The ship bow (FP) is fixed at $x/L=0$ and the stern (AP) is located at $x/L=1$. X-coordinate is taken as positive towards the aft of the ship. Y-coordinate is defined as positive towards the starboard direction and Z is positive in the upward direction which can be seen clearly either in Fig 3-3. The undisturbed free surface is located at $z/L=0$.

There are numerous boundary condition types, which can be grouped as domain truncation boundaries, physical boundaries, and computational boundaries in most of the CFD codes. In CFDSHIP-Iowa, twenty-six different boundary condition types are available. The boundary conditions used for the computations are listed in detail in Table 3-3. One of the domain truncation boundaries, the far field boundary conditions, is implemented for the top and bottom of the background domain. In the top of the background, far field BC type 2, in which the velocity is set by the input parameters and pressure and turbulence variables are zero gradient. The bottom of the background block is used as far field BC type 1 which sets the axial velocity component to input parameter and pressure to zero while all other variables are set as zero gradient. For the inlet, wave boundary conditions predicted from the linear potential flow solution, are applied as (Weymouth et al., 2005)³⁴. The exit boundary condition is assigned as an outlet.

After defining the domain truncation boundaries, the physical boundary and computational boundary conditions are designated. Since the symmetry wall is not used in this study, a zero gradient boundary condition is implemented for the sides of the background. The solid surfaces were defined as a no-slip wall or Navier-Stokes wall. Additionally, a rotating boundary condition for the hub is imposed. The rotational effect is introduced into the RANS code as user-defined boundary condition which is set on each grid point on the hub surface. This condition for a right-handed propeller is shown as a schematic in Fig 3-4 (a) for one axial section of the hub. The Reynolds-averaged velocity components on the hub surface (v and w)

Methodology

can be calculated by equation (6) and equation (7), where r_{hub} is the hub radius as shown in Fig 4-4 (a). The rotating velocity vectors (v and w) on the hub surface are illustrated in Fig 3-4 (b).

$$\zeta(x, t) = A \cos(kx - \omega_e t) \quad (2)$$

$$u(x, z, t) = \omega A e^{kz} \cos(kx - \omega_e t) \quad (3)$$

$$w(x, z, t) = \omega A e^{kz} \sin(kx - \omega_e t) \quad (4)$$

$$p(x, z, t) = \frac{\omega^2 A e^{kz}}{k} \cos(kx - \omega_e t) - \frac{\omega^2 A^2 e^{2kz}}{2} \quad (5)$$

$$v = 2\pi n r_{hub} \sin \theta \quad (6)$$

$$w = -2\pi n r_{hub} \cos \theta \quad (7)$$

Table 3-3 Boundary conditions

Location	Type	u	v	w	p	k_t	ω_t
Inlet	Wave	Eq. (3)	0	Eq. (4)	Eq. (5)	0	0
Outlet	Exit	$\nabla^2 u = 0$	$\nabla^2 v = 0$	$\nabla^2 w = 0$	$\nabla p = 0$	$\nabla k_t = 0$	$\nabla \omega_t = 0$
Sides	Zero Gradient	$\nabla u = 0$	$\nabla v = 0$	$\nabla w = 0$	$\nabla p = 0$	$\nabla k_t = 0$	$\nabla \omega_t = 0$
Top	Far field	u_∞	v_∞	w_∞	$\nabla p = 0$	$\nabla k_t = 0$	$\nabla \omega_t = 0$
Bottom	Far field	u_∞	$\nabla v = 0$	$\nabla w = 0$	0	$\nabla k_t = 0$	$\nabla \omega_t = 0$
Hull/stern	No-slip	0	0	0	$\nabla p = 0$	0	$60/Re\beta\Delta y^2$

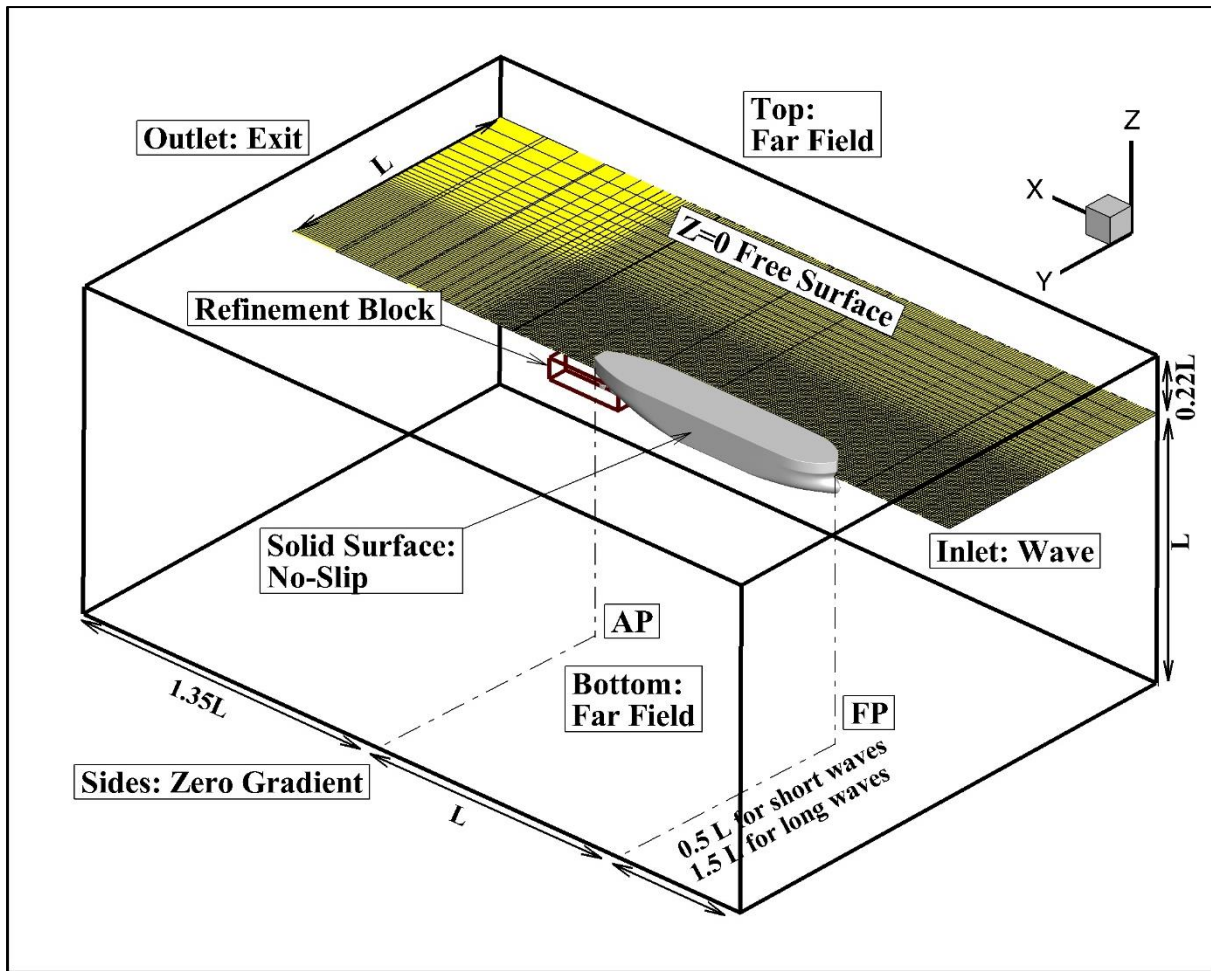


Fig 3-3 Computational domain and boundary conditions

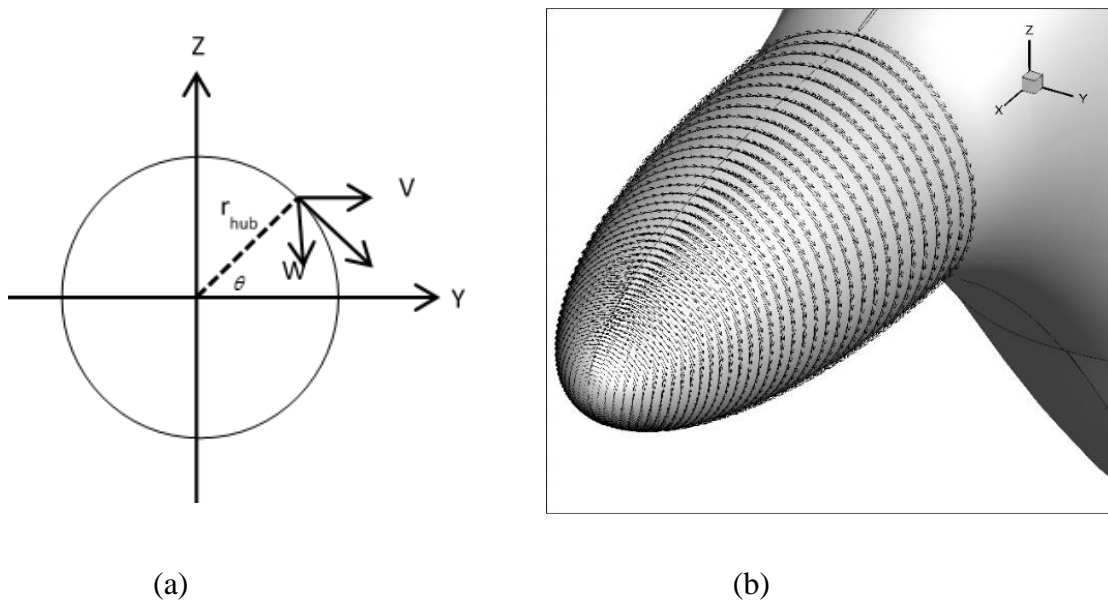


Fig 3-4 (a) Schematic of rotating hub boundary condition (b) Rotating vectors on hub

3.1.3 Overview of CFDSHIP-IOWA version 4.5

In this study, CFDSHIP-IOWA version 4.5 is used for computation of forces, moments, motions and so on³⁵). It is an incompressible unsteady Reynolds-averaged Navier-Stokes (URANS) or detached eddy simulation (DES) solver designed for ship hydrodynamics using structured multi-block and overset grids³⁶). A single-phase level-set approach is used for free-surface tracking and a semi-coupled air/water immersed boundary method is employed for two-phase computations. The functionalities of the code include 6DOF motions, turbulence modeling, moving control surfaces, multi-objects, advanced controllers, propulsion models, incoming waves and winds, bubbly flow, and fluid-structure interaction.

Originally designed to support both thesis and project research in the areas of resistance and propulsion, it has been successfully transitioned to Navy and university laboratories and industry, and has recently been extended to unsteady applications such as seakeeping and maneuvering. It was developed following a modern software-development philosophy, which was based upon open source, revision control, modular coding using Fortran 90/95, liberal use of comments, and an easy to understand architecture which enables model development by users.

The computation is performed for the ship-fixed case parallelization with MPI-based domain decomposition wherein each grid block is partitioned into sub-blocks by the user by specifying the number of times the grid needs to be split in I, J and K directions. In this study, the computations were carried out on the Toda Lab server of Osaka University, which contains seven CPUs with 124 cores (Intel Xeon E5). The whole domain was decomposed into 32 CPUs for parallel processing using one processor per block.

The code provides propeller modeling using simplified body-force or direct discretization and has a proportional-integral-differential (PID) controller to allow self-propulsion or auto-piloted simulations. The governing equations are discretized using finite difference schemes on body-fitted curvilinear grids. In the turbulence and momentum equations, the time derivatives are discretized using second order finite Euler backward difference, the convection terms are discretized with higher order upwind formula, and viscous terms are computed by second order central difference scheme. Projection method, a two-stage fractional step scheme, is employed to couple pressure and velocity field effectively. In order to solve the system of the discretized governing equations, between three and five inner iterations are run in each time step and solutions are considered to be converged once the error

for velocities, pressure, and level-set reach to less than 10^{-5} , 10^{-8} , and 10^{-5} respectively. ITTC recommends that non-dimensionalized time step must be smaller than 0.01 for one or two equation turbulence model. In this study, $0.005L/U$ time step is used and at least 6000 time steps were considered. The CFD work process for simulation of a fluid flow application is demonstrated in six distinctive phases as shown in Fig 3-5.

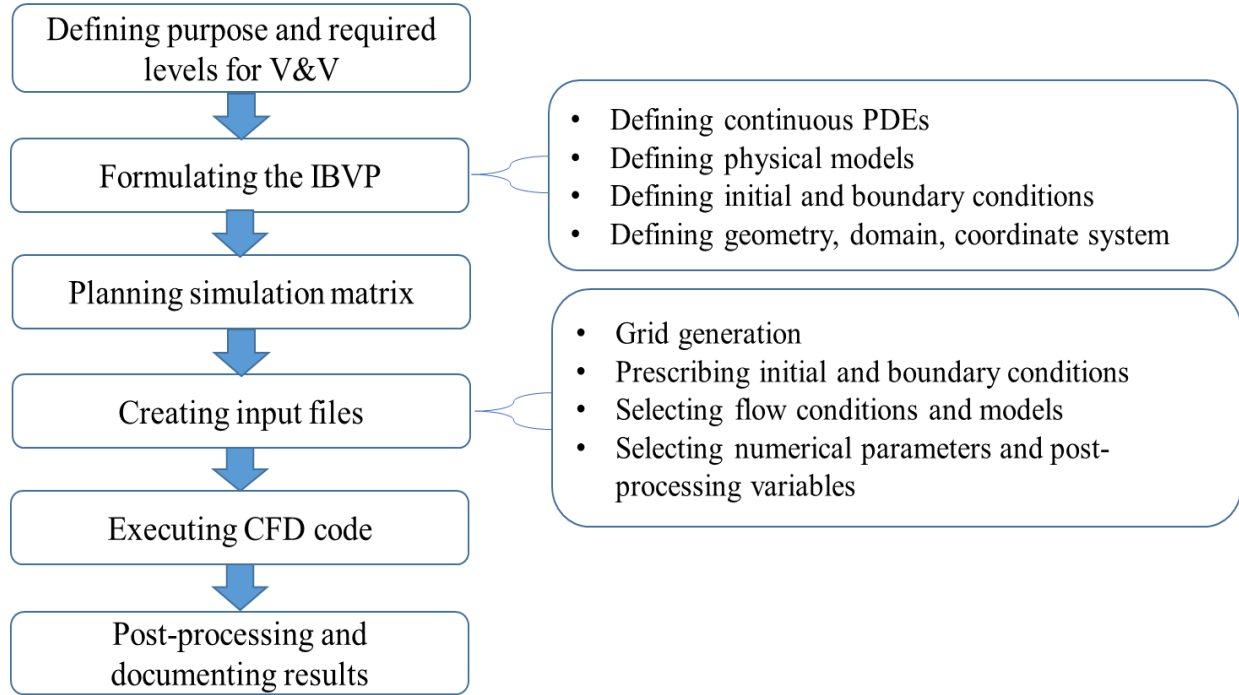


Fig 3-5 CFD process

3.1.4 Governing equations

The CFD code has been formulated to solve the RANS equations in either Cartesian or cylindrical-polar base coordinate systems. In addition, both systems may be in either absolute (i.e., earth-fixed inertial) or relative non-inertial (i.e., fixed to a moving body) reference frames. For Cartesian coordinates the continuous continuity and momentum equations in non-dimensional tensor form are as follows;

$$\frac{\partial U_i}{\partial x_i} = 0 \quad (8)$$

$$\frac{\partial U_i}{\partial t} + U_j \frac{\partial U_i}{\partial x_j} = -\frac{\partial \hat{p}}{\partial x_i} + \frac{1}{\text{Re}} \frac{\partial^2 U_i}{\partial x_j \partial x_j} - \frac{\partial}{\partial x_j} \overline{u_i u_j} + f_{b_i}^* \quad (9)$$

Where $U_i = (U, V, W)$ are the Reynolds-averaged velocity components,

$x_i = (x, y, z)$ are the independent coordinate directions,

Methodology

$\hat{p} = \left[\frac{p - p_\infty}{\rho U_0^2} + \frac{z}{Fr^2} \right]$ is the piezometric pressure coefficient,

$-\overline{u_i u_j}$ are the Reynolds stresses which are a two-point correlation of the turbulent fluctuations,

$f_{b_i}^*$ is the non-dimensional body-force vector ($= f_{b_i} L / \rho U_0^2$) where f_{b_i} is a force per unit volume which represents the effect of the propeller. All equations are non-dimensionalized by reference velocity U_0 , length L , and density ρ .

The Reynolds stress are directly related to the mean rate of strain through an isotropic eddy viscosity ν_t . In Cartesian coordinates, it can be written as equations (10). δ_{ij} is the Kronecker delta.

$$-\overline{u_i u_j} = \nu_t \left[\frac{\partial U_i}{\partial x_j} + \frac{\partial U_j}{\partial x_i} \right] - \frac{2}{3} \delta_{ij} k \quad (10)$$

$$\frac{\partial U_i}{\partial t} + U_j \frac{\partial U_i}{\partial x_j} = -\frac{\partial \hat{p}}{\partial x_i} + \frac{1}{Re} \frac{\partial^2 U_i}{\partial x_j \partial x_j} + \frac{\partial \nu_t}{\partial x_j} \left[\frac{\partial U_i}{\partial x_j} + \frac{\partial U_j}{\partial x_i} \right] + f_{b_i}^* \quad (11)$$

Substituting the Reynolds-stress term, the momentum equations in Cartesian coordinates become equation (11).

3.1.5 Turbulence model

In general, all the flows can be mathematically described with the Navier-Stokes equations. Nevertheless, there is a problem to solve turbulence flow which is an unsteady 3-D fluid motion with irregular, high-frequency spatial, and temporal fluctuations in flow quantities. If we want to solve a turbulent flow exactly, the smallest vortex element has to be resolved. As a result, the computational grid will be bigger with the high number of grid nodes, and the computational time will become extremely long. For this reason, I used a RANS model with two-equation Shear-stress transport (SST) $k-\omega$ model to solve turbulent flow. In the SST model, I did not use any wall functions since the grids in the boundary layer near the wall are fine enough.

In CFDSHIP-IOWA, eddy viscosity can be calculated using one of two models: Baldwin Lomax or the blended $k-\omega/k-\epsilon$, including an option for the shear stress transport (SST) model. The blended $k-\omega/k-\epsilon$ (SST) model has proven to be robust, applicable to complex geometries and flows, and fairly accurate. It is computationally economical and a workhorse for practical engineering computations³⁷. In nearly all circumstances, it is superior to $k-\epsilon$ models, which

Methodology

require complicated near-wall models that are difficult to implement in a general fashion. The governing equations for the eddy viscosity ν_t , turbulent kinetic energy k , and the turbulent specific dissipation rate ω are as follows;

$$\nu_t = \frac{k}{\omega} \quad (12)$$

$$\frac{\partial k}{\partial t} + \left(U_j - \sigma_k \frac{\partial \nu_t}{\partial x_j} \right) \frac{\partial k}{\partial x_j} - \frac{1}{R_k} \nabla^2 k + s_k = 0 \quad (13)$$

$$\frac{\partial \omega}{\partial t} + \left(U_j - \sigma_\omega \frac{\partial \nu_t}{\partial x_j} \right) \frac{\partial \omega}{\partial x_j} - \frac{1}{R_\omega} \nabla^2 \omega + s_\omega = 0 \quad (14)$$

where the source terms, effective Reynolds numbers, and turbulence production are defined as

$$s_k = R_k (-G + \beta^* \omega k) \quad (15)$$

$$s_\omega = R_\omega \left[-\gamma \frac{\omega}{k} G + \beta \omega^2 + 2(1 - F_1 \sigma_{\omega 2}) \frac{1}{\omega} \frac{\partial k}{\partial x_j} \frac{\partial \omega}{\partial x_j} \right] \quad (16)$$

$$R_k = \left(\frac{1}{1/\text{Re} + \sigma_k \nu_t} \right) \quad (17)$$

$$R_\omega = \left(\frac{1}{1/\text{Re} + \sigma_\omega \nu_t} \right) \quad (18)$$

$$G = \tau_{ij} \frac{\partial U_i}{\partial x_j} = \nu_t \left[(U_y + V_x)^2 + (U_z + W_x)^2 + (V_z + W_y)^2 + 2U_x^2 + 2V_y^2 + 2W_z^2 \right] \quad (19)$$

$$F_1 = \tanh \left[\left\{ \min \left[\max \left(\frac{\sqrt{k}}{0.09 \omega \delta}, \frac{500}{\text{Re} \delta^2 \omega} \right); \frac{4 \sigma_{\omega 2} k}{CD_{k\omega} \delta^2} \right] \right\}^4 \right] \quad (20)$$

$$CD_{k\omega} = \max \left(2 \sigma_{\omega 2} \frac{1}{\omega} \frac{\partial k}{\partial x_j} \frac{\partial \omega}{\partial x_j}; 10^{-20} \right) \quad (21)$$

$$\nu_t = \frac{0.31k}{\max(0.31\omega, \Omega F_2)} \quad (22)$$

$$F_2 = \tanh \left[\max \left(\frac{2\sqrt{k}}{0.09\omega y}, \frac{500}{y^2 \omega} \right)^2 \right] \quad (23)$$

The blending function F_1 was designed to be 1 in the sublayer and logarithmic regions of boundary layers and gradually switch to zero in the wake region to take advantage of the

strengths of the $k-\omega$ and $k-\varepsilon$ models, i.e., $k-\omega$ does not require near-wall damping functions and uses simple Dirichlet boundary conditions and the $k-\varepsilon$ does not exhibit sensitivity to the level of free stream turbulence as does the $k-\omega$ model. The SST model accounts for transport of the principal turbulent stresses and has shown improved results for flows with adverse pressure gradient.

3.1.6 Free surface

CFDSHIP-IOWA uses a surface tracking approach for modeling the free surface. The free surface detection is computed by the level set method. The standard level set method for incompressible free surface viscous flows is originated about 1995 which is well known as two-phase level set method in which the solution is obtained in both fluids. In this computation, only one phase will be taken into account to get the solution and it is known as single phase level set method. The 3D level set function ϕ is defined in the whole domain with its value related to the distance to the interface. The sign of ϕ is arbitrarily set to negative in air and positive in water and the iso-surface $\phi=0$ represents the free surface. Since the free surface is considered a material interface, then the equation for the level set function is:

$$\frac{\partial \phi}{\partial t} + \frac{\partial(\phi U_i)}{\partial X_i} = 0 \quad (24)$$

And from the level set function, the normal can be computed as

$$n = -\frac{\nabla \phi}{|\nabla \phi|} \quad (25)$$

The boundary conditions for the velocity at the interface is

$$\nabla U \cdot n = 0 \quad (26)$$

In addition, a zero normal gradient for both k and ω is used at the free surface as

$$\nabla k \cdot n = 0 \quad (27)$$

$$\nabla \omega \cdot n = 0 \quad (28)$$

3.1.7 Body force propeller model

The body force propeller is the time-averaged influence of the propeller on the fluid in the propeller region. The body force field can be computed by means of potential theory based propeller models. There are two main types of propeller models; prescribed and interactive models. In prescribed model, body force field is calculated only once and inserted into RANS solver. In interactive model, propeller and RANS codes are run in turn to iterate towards a solution. In this study, Osaka University propeller model^{38, 39)} is applied. It was developed at Toda Lab, Osaka University, is used to predict the propeller performance using the total output

velocity predicted by CFD at propeller plane. In this propeller model, the propeller blade which has radius, R is split into sections of width, dr , forming blade element with the radial distance, r from the center of the propeller. Fig 3-6 shows the blade element theory for thrust and torque calculation for one blade element.

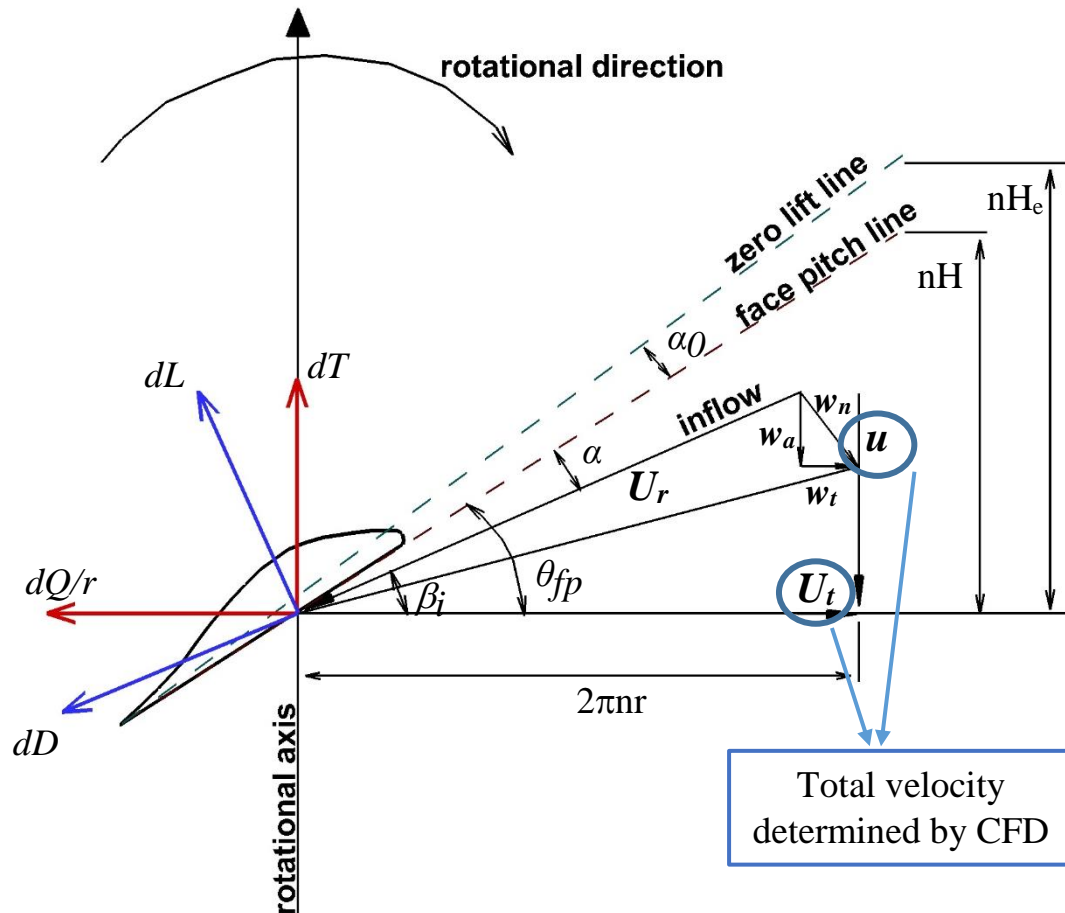


Fig 3-6 Sketch of blade element theory

The resultant velocity at each radial segment is obtained by equation (29). From that resultant velocity, lift force (L) and drag force (D) can be calculated by equation (34) and (35). Two dimensional sectional drag coefficient of the propeller blade is assumed to be 0.02. The effective pitch (H_e) is taken as 1.08 times of the geometric pitch of the propeller (H). Velocities (including propeller induced effect) on the propeller blade are calculated within RANS code. Finally, the body-forces acting in radial and angular direction on the propeller plane are computed by equation (38) and (39). In sequence, the body forces acting in y and z direction are obtained by $Fb_y = Fb_\theta \cos \beta_i$ and $Fb_z = Fb_\theta \sin \beta_i$ where β_i is propeller hydrodynamic pitch angle. The overall thrust (T) and torque (Q) of the rotor are obtained by integrating the

individual contribution of each element along the radius of the propeller using equation (40) and (41).

$$U_r = \sqrt{u^2 + (2\pi nr - U_t)^2} \quad (29)$$

$$\beta_i = \tan^{-1}\left(\frac{u}{2\pi nr - U_t}\right) \quad (30)$$

$$C_L = 2\pi k_1 \sin(\alpha + \alpha_0) \quad (31)$$

$$C_D = 0.02 \quad (32)$$

$$k_1 = 1.07 - 1.05\left(\frac{c_{0.7R}}{R}\right) + 0.375\left(\frac{c_{0.7R}}{R}\right)^2 \quad (33)$$

$$dL = \frac{1}{2} C_L U_r^2 c(r) \quad (34)$$

$$dD = \frac{1}{2} C_D U_r^2 c(r) \quad (35)$$

$$dT = dL \cos \beta_i - dD \sin \beta_i \quad (36)$$

$$dQ = (dL \sin \beta_i + dD \cos \beta_i) \cdot r \quad (37)$$

$$Fb_x = \frac{dT \cdot N}{\Delta x \cdot 2\pi r} \quad (38)$$

$$Fb_\theta = \frac{dQ \cdot N}{\Delta x \cdot 2\pi r^2} \quad (39)$$

$$T = \int_0^{2\pi} \int_{R_B}^R Fb_x \Delta x r dr d\theta \quad (40)$$

$$Q = \int_0^{2\pi} \int_{R_B}^R Fb_\theta \Delta x r^2 dr d\theta \quad (41)$$

where u is axial velocity including induced velocity in CFD code, U_t is tangential velocity including induced velocity in CFD code, n is non-dimensional number of revolutions of the propeller, w_a is axial induced velocity, w_t is tangential induced velocity, w_n is total induced velocity, β_i is hydrodynamic pitch angle, r_e is radius of the representative blade section, Δx is grid spacing in axial direction at body force point and N is number of blades.

3.2 Experimental Fluid Dynamic (EFD) Method

The experimental fluid dynamic study on the RBFS's performance was performed by Mwangi (2021)⁴⁰. The experiments were carried out in the mid-sized towing tank of Osaka University as presented in Fig 3-7. A towing carriage having 7.4m in length and 7.8m in width outfits on the upper part of the tank. The dimensions of towing tank are 100m in length, 7.8m in width, and 4.35m in depth. The towing carriage runs a speed range of 0.01 to 3.5m/s applied for towing the model ship and the SPIV system during the experiments. A plunger-type wave generator which is used to generate both regular and irregular waves of up to 500mm wave height and 0.5 to 15m wavelengths was outfitted at the rear of the basin. The towing tank is equipped with a wave dampening beach which is raised during running an experiment and lowered immediately after a run in order to settle the waves for the succeeding run. In general, a waiting time interval of about fifteen to thirty minutes is necessary to proceed with the subsequent run. In addition to the dampening beach, the towing tank has a fixed small gridiron beach at the end to absorb waves.

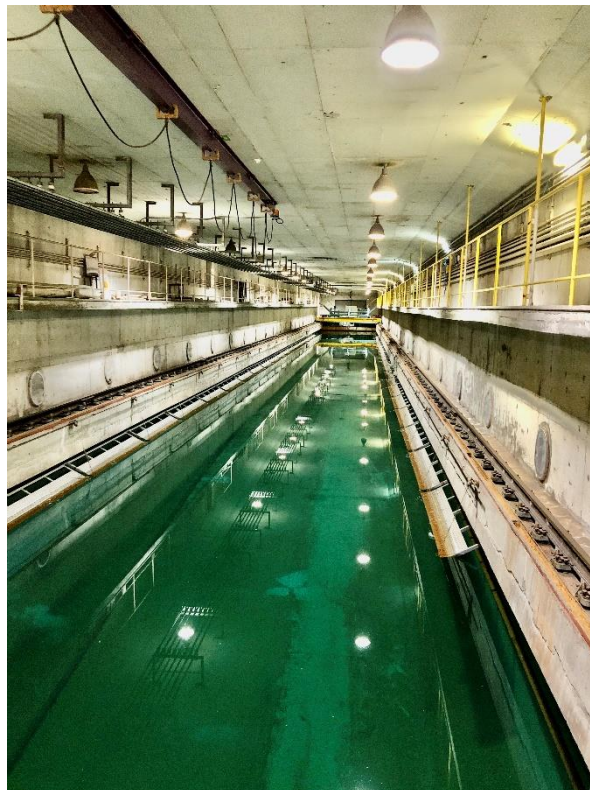


Fig 3-7 Towing tank of Osaka University

The 3.2m long KVLCC2 tanker model shown in Fig 3-8 was used in this experiment at fully loaded condition. The four-bladed MOERI propeller model with a diameter of 0.0986m was used for the self-propulsion experiments. In the motions and force measurement, the right-

Methodology

handed propeller was used while both the right and left hand propellers were used during SPIV measurement in order to measure the flow field in the transverse plane upstream of the propeller. The reason of using both propellers is that the measurement of the flow field on the starboard side cannot be done due to the obstruction of the laser sheet and the camera focus by the hull during the SPIV measurement⁴⁰. 16.5 rps of propeller revolution rate was used in the self-propulsion test. Fig 3-9 shows the propeller models.



Fig 3-8 KVLCC2 tanker model (Mwangi, 2021)



Fig 3-9 Propeller models (Mwangi, 2021)

The motions and force measuring experiments were performed at fully loaded conditions in five wavelengths ($\lambda/L = 0.6, 0.85, 1.1, 1.35, \text{ and } 1.6$). Three degree of freedom motions (heave, pitch and surge), thrust, torque, and resistance were measured. The SPIV flow field measurements were conducted at two transverse planes; upstream of the propeller and downstream of the rudder in three wavelengths ($\lambda/L = 0.6, 1.1, \text{ and } 1.6$). The phases for the SPIV measurement were decided at the wave gauge which was installed at 3.62 m ahead of FP.

Methodology

A four-pulse program code was used to send signals to the SPIV system for recording images at four phases (0, 90, 180 and 270 degrees) for $\lambda/L=0.6$. In the case of $\lambda/L=1.1$ and 1.6, images were recorded at six phases (0, 60, 120, 180, 240 and 300 degrees respectively) using a six-pulse program code⁴⁰.

Various devices were used to measure wave elevation, force in the x- direction, heave, pitch and surge motions, as well as thrust and torque alongside the flow field. Table 3-4 gives a summary of the measured contents and measuring devices.

Table 3-4 List of Measuring parameters and devices

Measured parameters	Measuring devices
Resistance, F_x (N)	Dynamometer
Heave (cm)	Potentiometer
Pitch (deg)	Potentiometer
Surge (cm)	Potentiometer
Incident wave amplitude (cm)	Servo-type wave height meter
Thrust (N)	Self-propelled dynamometer
Torque (Nm)	Self-propelled dynamometer

Chapter -4- Results and Discussions

4.1 Ship motion analysis

A ship moving on the surface of a sea experiences six types of motion, three linear motions and three rotational motions. It can be categorized into two distinct groups of motion; rotational motions and translational motions. Pitching, rolling, and yawing are defined as rotational motions. In translational motions, there are three types of motions; heaving, swaying, and surging. The purpose of investigating the motion responses is to confirm whether the ESD can make huge changes or adverse effects on the ship's operation compared to the normal condition. The prediction of these six degree of freedom (DOF) motions is available in CFDSHIP-Iowa.

In this code, the 6DOF equations of motion of a ship are described by translations concerning the static location of the center of gravity on the earth system, and by the rotations in terms of the Euler angle. Forces and moments are calculated by integrating the forces on the solid surfaces and the forces and moments generated by the propeller models and gravity force. The gravity and fluid forces and moments are predicted in the earth fixed system and then transported into the ship fixed system where the propulsive forces and moment are combined. The integration process can be done numerically using either an explicit or implicit predictor-corrector approach in CFDSHIP-Iowa³⁵).

In this study, the ship hull was considered as a rigid body with two degrees of freedom so that only heave and pitch motions can be predicted. These motions are two main features in the vertical movement system of the ship. In the numerical simulation, time history data and motion responses relative to the ship's center of gravity corresponding to the wave crest at FP were obtained by using a second-order implicit integration mode. In the case of EFD, the measurements were conducted at a wave gauge meter mounted at 3.62m ahead of FP. EFD measurement data was shifted to the FP from the wave gauge meter in order to perform validation.

4.1.1 Time history of motions

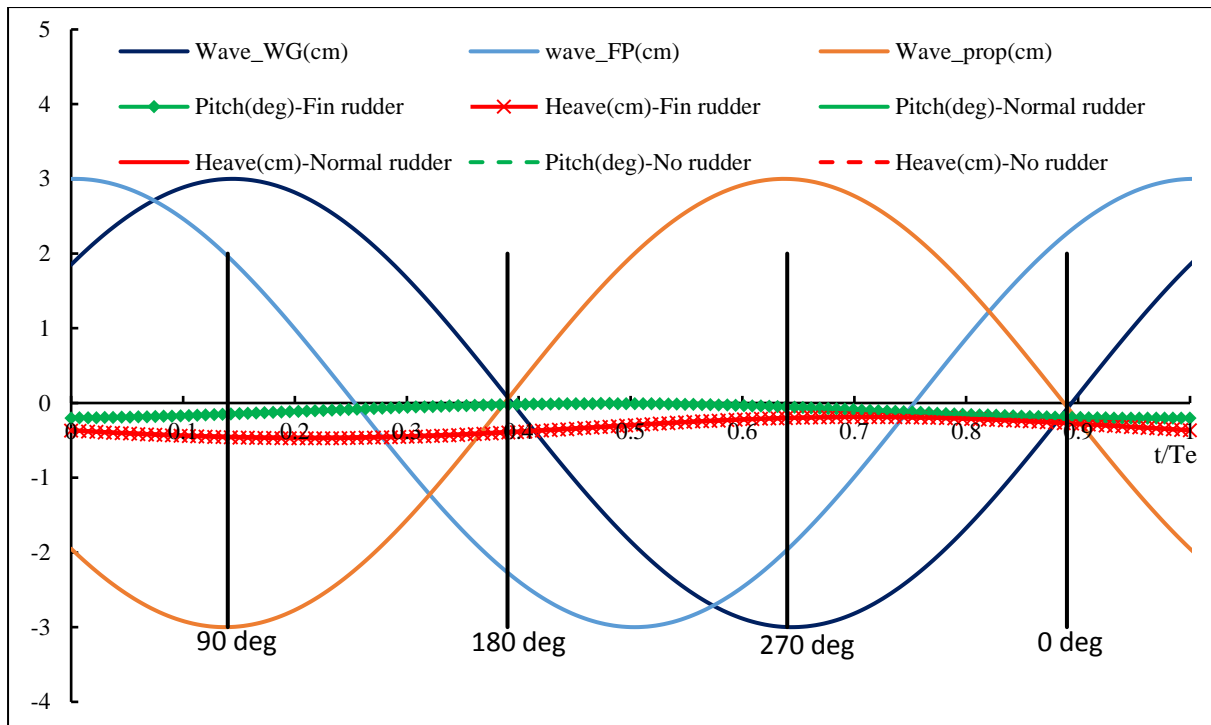
Fig 4-1, 4-2, and 4-3 provide the information on the comparison of heave and pitch motions between three cases; ship without rudder, ship with normal rudder, and ship with RBFS, in CFD for three wavelengths ($\lambda/L = 0.6, 1.1, \text{ and } 1.6$). Heave motion in cm and pitch motion in degree are defined on the Y-axis and non-dimensionalized one encounter period are set on the X-axis. A group of red colored lines represents the heave motions whilst the set of

green colored lines describes the pitch motions computed in three cases. The dotted line shows the motion data of the ship without a rudder. The solid line and the solid line with marker reveal the results of the ship with normal rudder and RBFS cases.

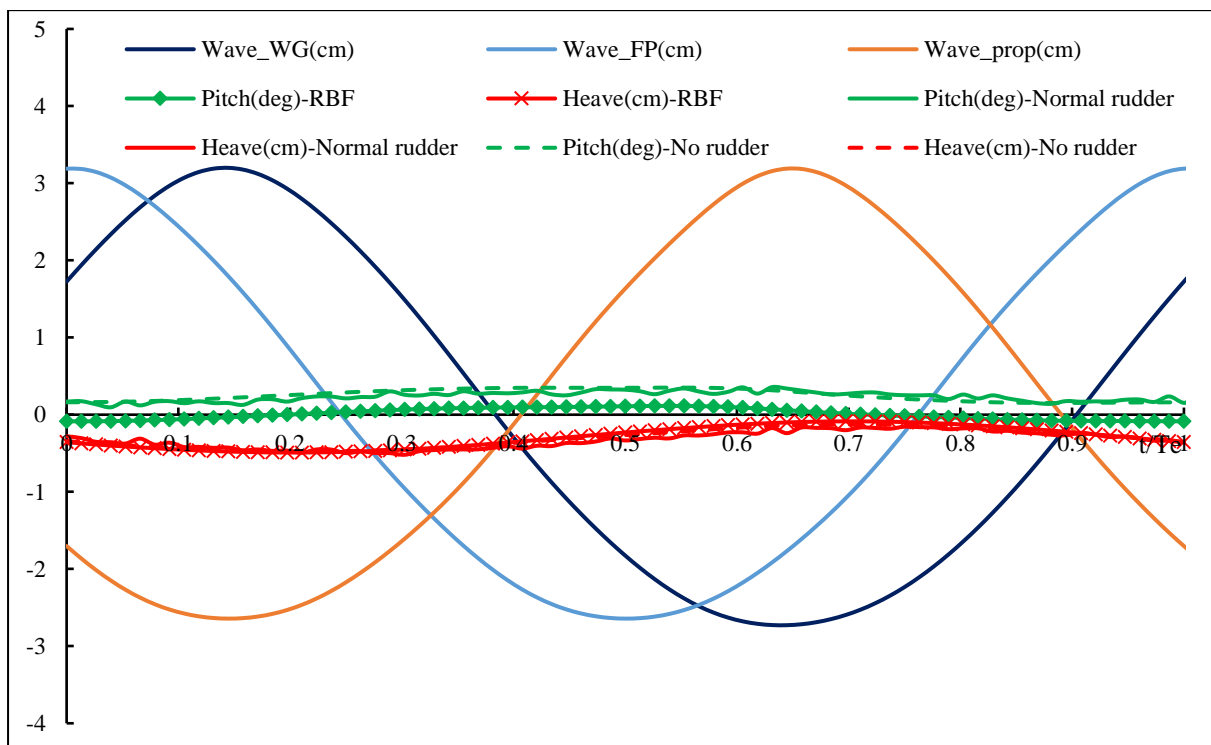
The time histories of incident wave elevations at the bow, wave gauge, and propeller section were calculated by using equation (42) and illustrated with pale blue, dark blue, and orange colors respectively.

$$\zeta = A \cos (kx - \omega_e t) \quad (42)$$

where ζ is the wave elevation and A is wave amplitude and k is wave number ($2\pi/\lambda$) and x is longitudinal position and ω_e is encounter frequency and t is time. The vertical lines (90, 180, 270, 360 deg, and so on) show the phases of a wave at wave gauge, in which the flow field measurements were performed. The experimentally measured data of heave and pitch motions in various wavelengths over one encounter period, T_e , is properly demonstrated in Fig 4-1 (b), 4-2 (b), and 4-3 (b) for validation purpose.



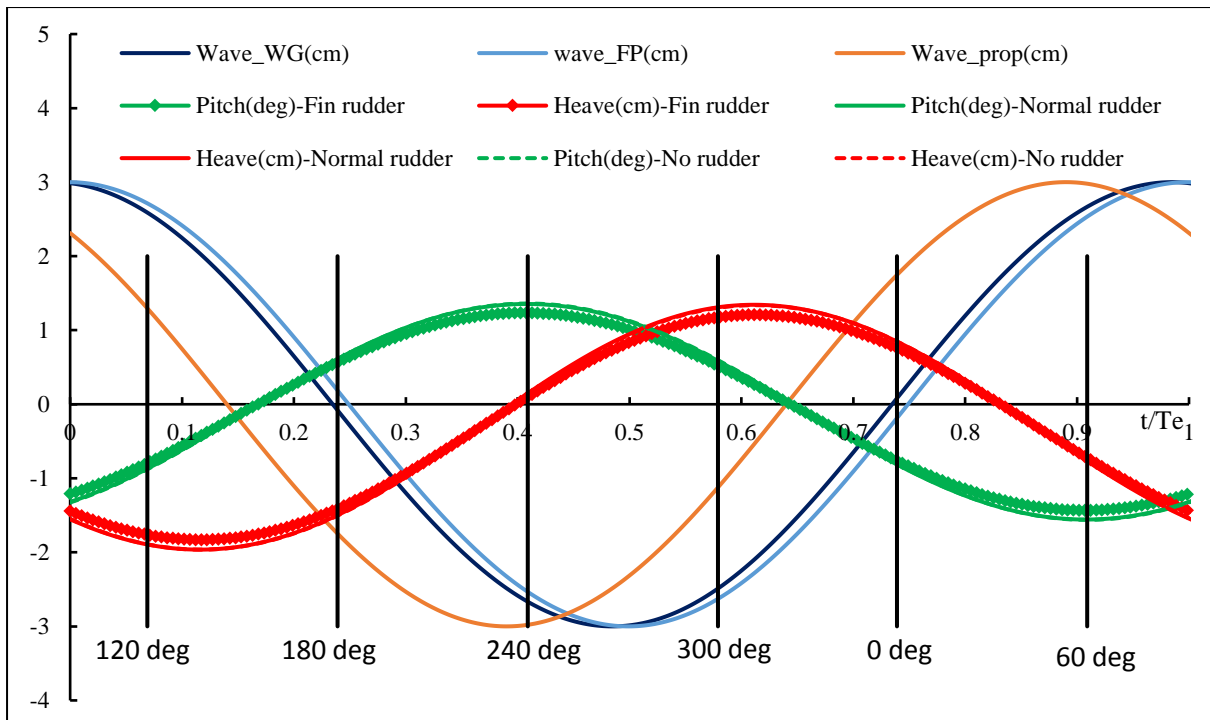
(a) CFD Simulation



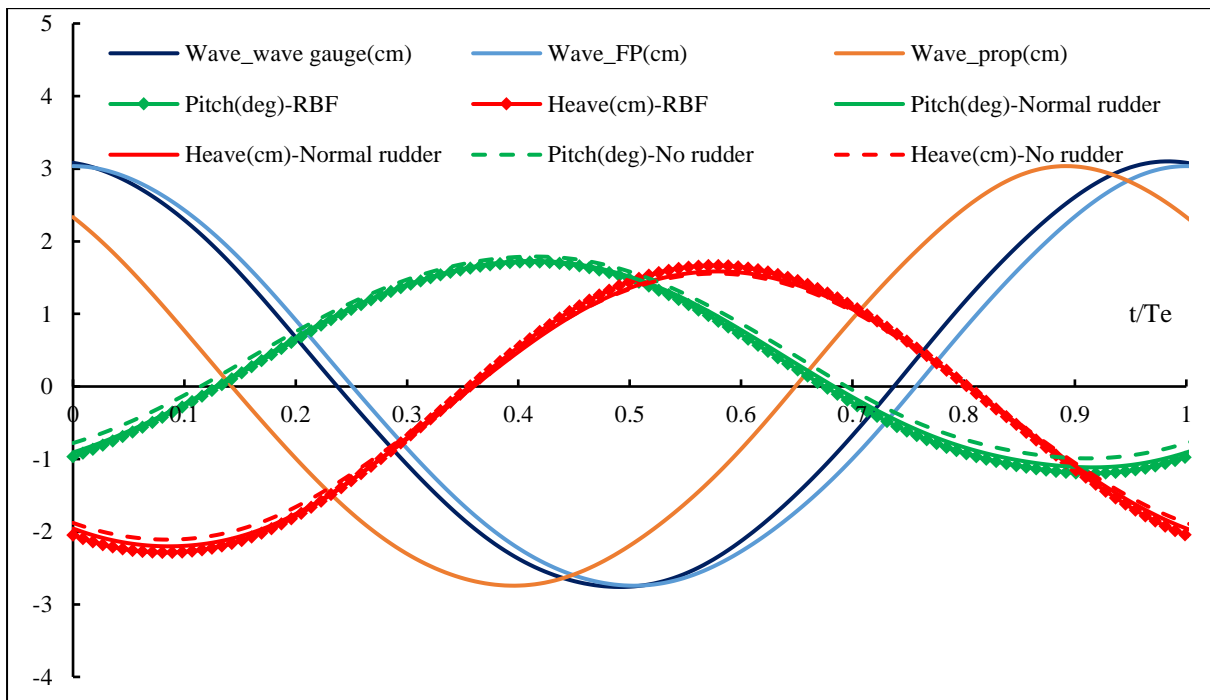
(b) EFD

Fig 4-1 Comparison of heave and pitch motion time histories at $\lambda/L=0.6$

[Wave_WG means wave at wave gauge, Wave_FP is wave at forward perpendicular, and Wave_prop represents as wave at propeller plane]



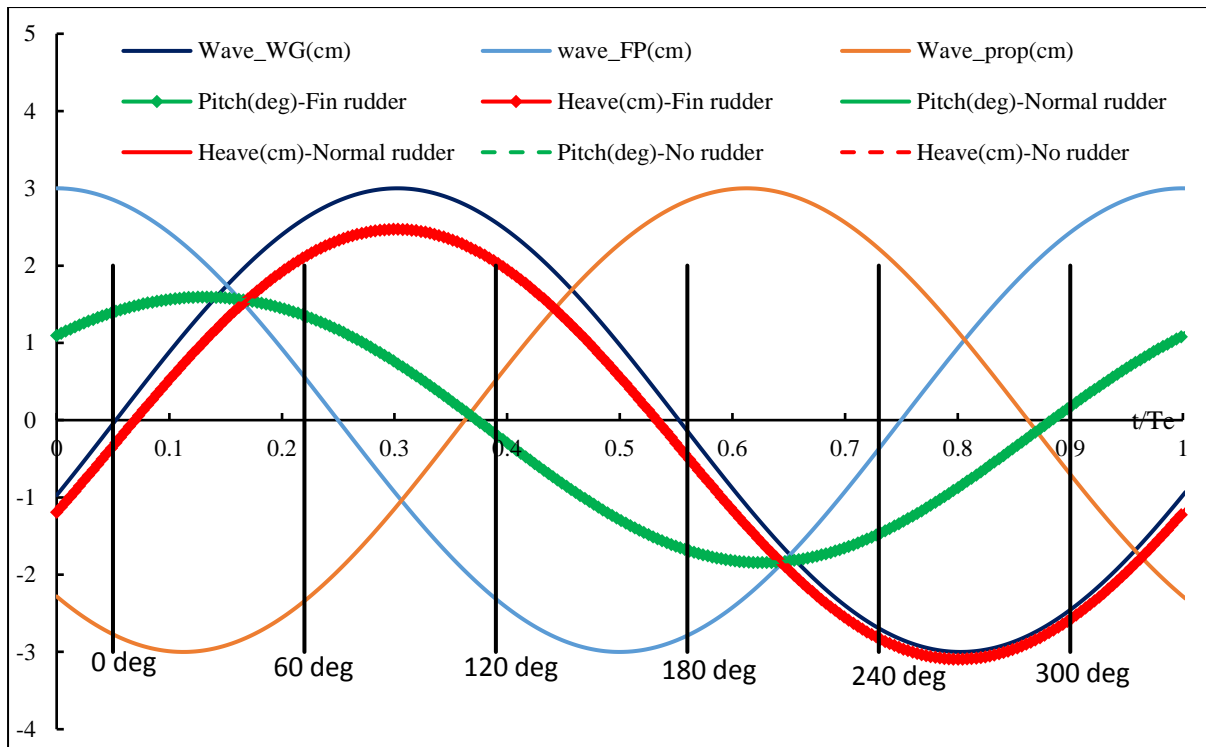
(a) CFD simulation



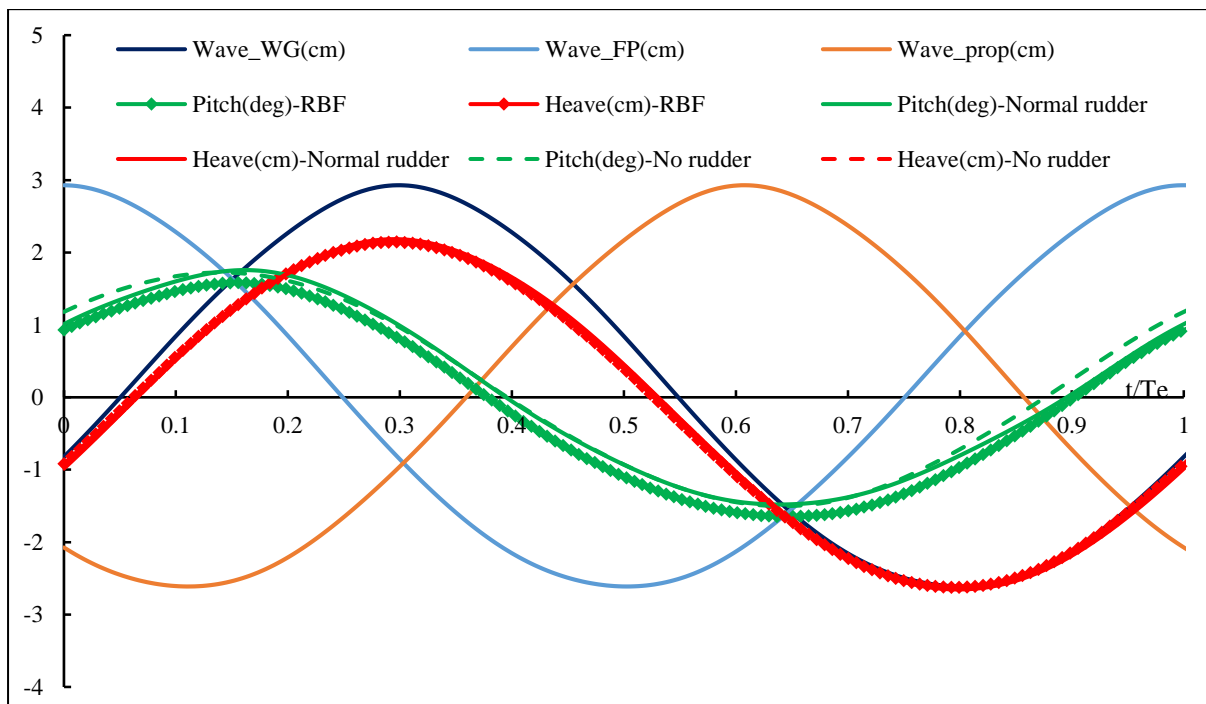
(b) EFD

Fig 4-2 Comparison of heave and pitch motion time histories at $\lambda/L=1.1$

[Wave_WG means wave at wave gauge, Wave_FP is wave at forward perpendicular, and Wave_prop represents as wave at propeller plane]



(a) CFD simulation



(b) EFD

Fig 4-3 Comparison of heave and pitch motion time histories at $\lambda/L=1.6$

[Wave_WG means wave at wave gauge, Wave_FP is wave at forward perpendicular, and Wave_prop represents as wave at propeller plane]

The heave motion oscillated harmonically over a period of time in both computation and experiment. In the short wave ($\lambda/L=0.6$), the fluctuation of motion was very small and increased considerably at medium wavelength, $\lambda/L = 1.1$. The largest heave motion was observed at a long wave, $\lambda/L = 1.6$. The results of the two types of rudder in both methods were almost the same from the point of view of phase lag and amplitude. As a consequence, the lines are coincided with each other, especially in the short wave and long wave. The computed heave motion time histories showed a good agreement with that of EFD. CFD under-predicted the heave motion in $\lambda/L = 1.1$. On the other hand, it over-predicted a little bit in other wavelengths. There was a small phase difference between EFD and CFD in both rudders at $\lambda/L=1.1$.

Similar to the heave motion, the pitch motion travels harmonically with time in all wave conditions. In the same manner as heave motion, the pitch motion time history of both normal rudder and RBFS had the same pattern in both methods. It means that the RBFS does not have any effect on ship motions. The CFD predicted well the trend of pitch motion as EFD and had good agreement with EFD in most wavelengths. Nevertheless, the underprediction of CFD is fairly large in $\lambda/L = 1.1$ where the ship length and wavelength are almost the same and the largest added resistance and the resonance occurs. The possible error might be that the grid size and time step make it difficult to capture the wave crest or trough at the exact location and time in computation since the number of time steps cannot be an integral number in one wave encounter period and the number of grid points per wavelength and height cannot be integral number as well. In EFD, the exact distance between the wave meter mounted on the front end of the carriage and the ship's center of gravity was hard to measure due to the towing tank structure.

4.1.2 First harmonic amplitude and phase

The comparison of the first harmonic of heave amplitude, z_1/A and corresponding phase, z_{e1} and mean value, z_0 between the normal rudder and RBFS in CFD and EFD are shown in Fig. 4-4. The motion responses in the time domain were obtained from the CFD code. In all wave conditions, the convergence of the motions was observed after 2000 iterations. Fourier transformation of those converged region of motion history was performed. The heave amplitude was dimensionalized by the wave amplitude, A . The mean heave value is calculated in centimeters and the first harmonic phase is in degree unit. The phase lag in this study is the difference between a phase of wave at CG and a phase of motions. The increase of the non-dimensionalized heave amplitude of motions with the increment of the wavelength was observed in all cases up to $\lambda/L=1.35$. The amplitude was closed to zero in short wavelengths

($\lambda/L = 0.6$ and 0.85) and increased abruptly to one in medium and long wavelengths where the ship's motion was quite large. The peak value was investigated at $\lambda/L = 1.35$. The first harmonic heave phase showed zero phase lag in long wave ($\lambda/L = 1.6$) which means the ship moved in the same way of the wave movement. The phase lag decreased slowly to minus 60 degree for medium wave then reaching to plus 30 degree at short wave ($\lambda/L = 0.6$). In all wavelengths, the mean heave value of the two kinds of rudder was the same around -0.3cm which was equal to the sinkage in calm water. There was no large difference between the heave motion response of the two types of rudder in both CFD and EFD. The CFD simulation predicted the same trend of z_1/A of EFD in all wave conditions. However, CFD under predicted with 6%D at $\lambda/L = 1.1$ and over predicted a bit for $\lambda/L = 1.35$. The prediction of phase lag and mean value of heave motion by CFD showed a good agreement with EFD in all wavelengths except the over prediction of mean value at $\lambda/L = 1.1$.

Fig. 4-5 gives the information about the first harmonic amplitude of pitch θ_1/A_k and corresponding phase $\theta_{\epsilon 1}$ and mean value θ_0 of both normal rudder and RBFS calculated in CFD and EFD. The pitch amplitude was dimensionalized by wave slope, A_k . The mean value and the first harmonic phase lag are described as degree unit. The non-dimensionalized pitch amplitude increased with increasing wavelength and hit the peak at a long wavelength. The first harmonic phase lag at $\lambda/L = 1.6$ was 60 degree and decreased steadily with decreasing of wavelength until it reached to $\lambda/L = 0.85$ then rose to 120 degree at $\lambda/L = 0.6$. The average value of pitch motion, θ_0 was around -0.1 degree in all wave conditions. The amplitude and phase lag of pitch between the normal rudder and fin rudder with bulb were predicted the similar value in CFD whereas there was a huge difference at some wavelength in EFD. It is necessary for further experiments to investigate or explore the problems existing at those wavelengths in EFD. The CFD predictions followed closely the EFD trend in the majority of cases but CFD under-predicted the amplitude of both motions at $\lambda/L = 1.6$.

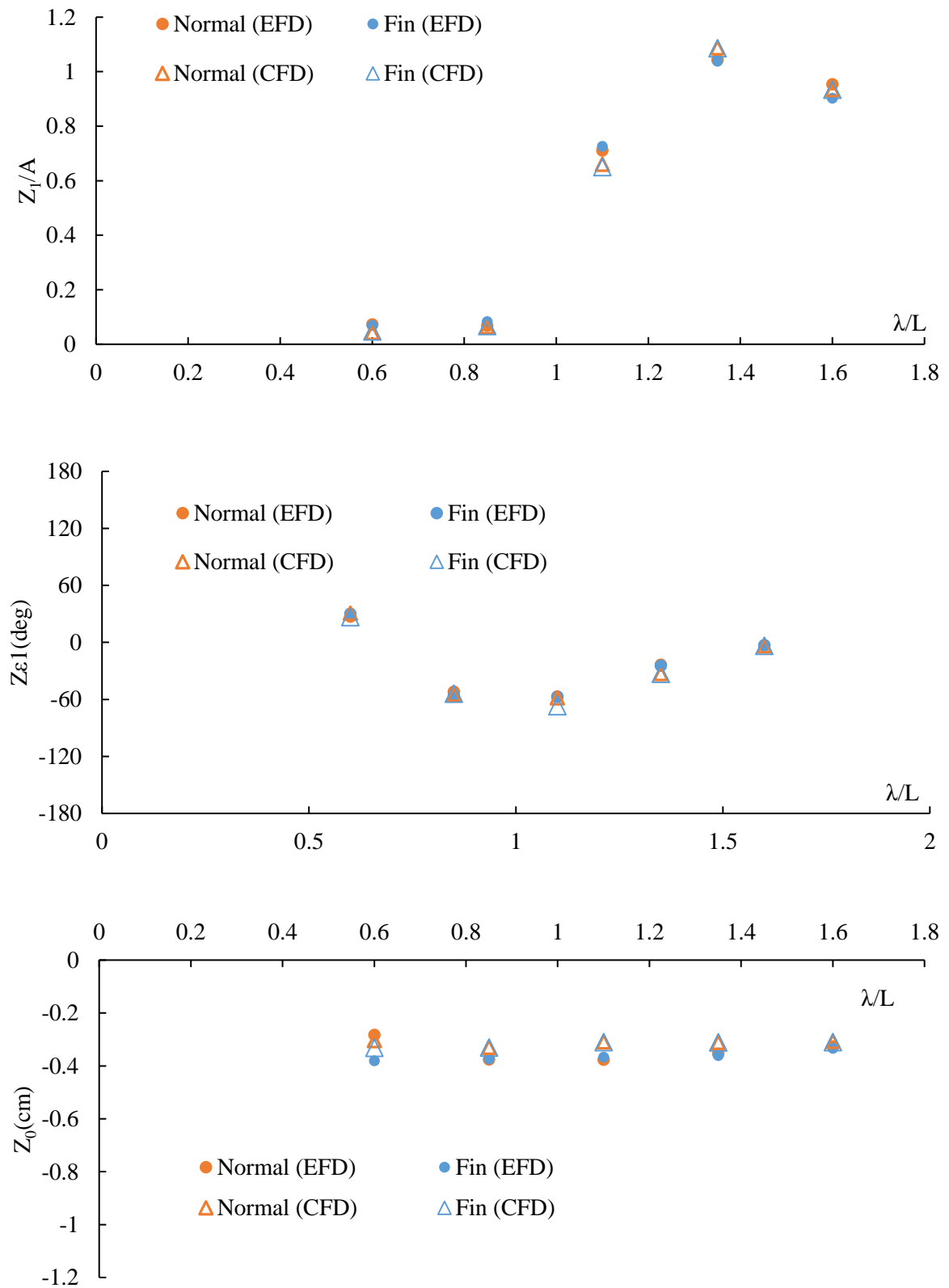


Fig 4-4 First harmonic amplitude, phase lag, and mean value of heave motion
 (Normal: normal rudder and Fin: rudder with RBFS)

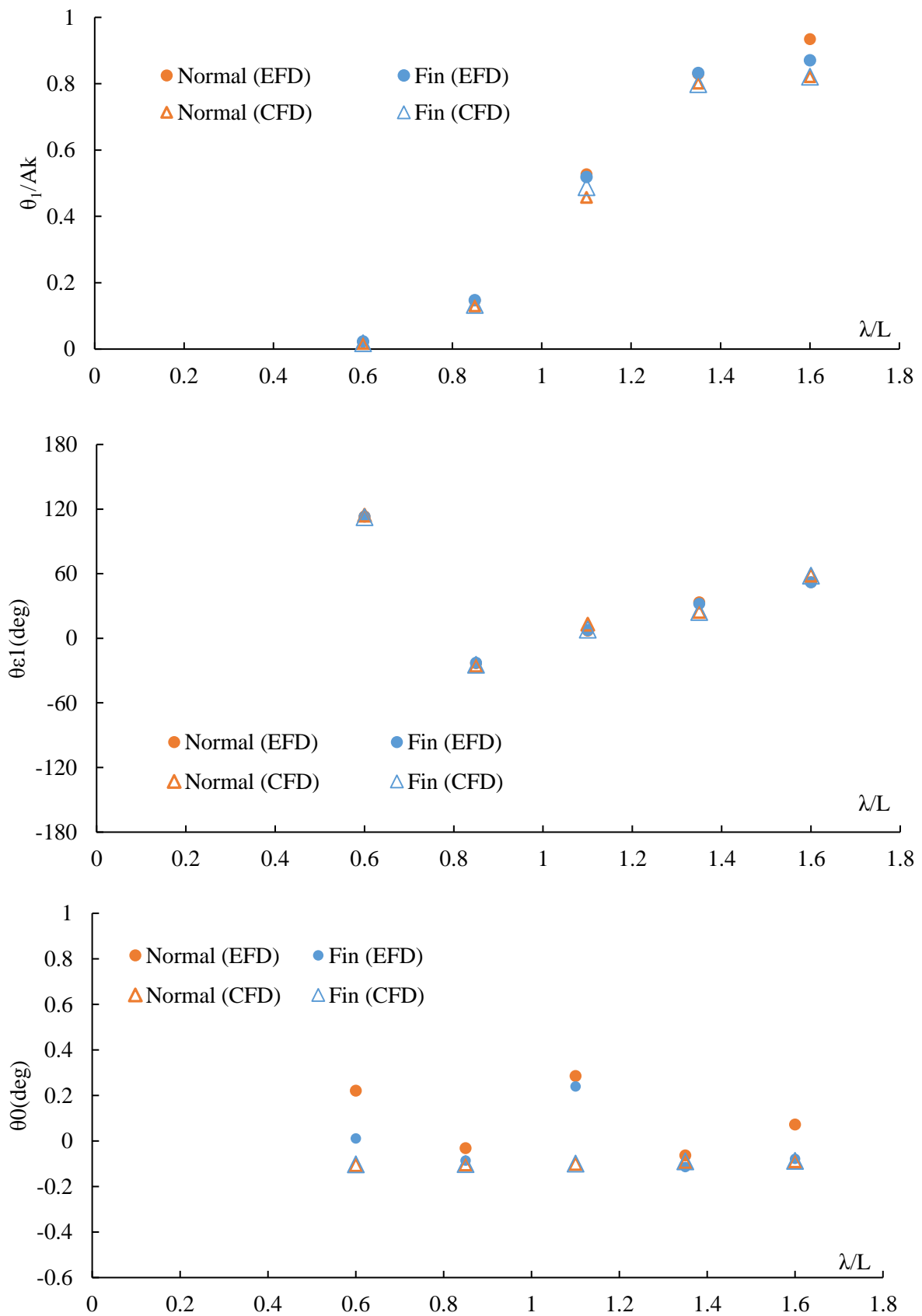


Fig 4-5 First harmonic amplitude, phase lag and mean value of pitch motion

(Normal: normal rudder and Fin: rudder with RBFS)

4.2 Flow Field Analysis

4.2.1 Flow field measurements

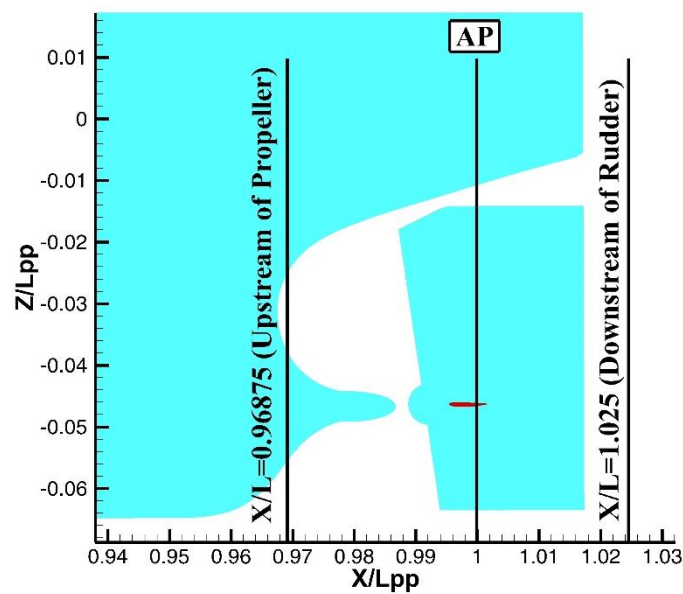
When a vessel moves on the water surface, wake waves are caused going both fore and aft. This causes the propeller to work in a non-uniformed water flow, that's called a wake field. A vessel, under its motion through the water, makes a wake field in the sense of an uneven flow velocity distribution occurring in the stern's region. Therefore, it is essential to predict the wake fields behind the ship to see the nature of the flow field in the ship's stern. To make use of the wake field data, it is necessary to be defined in a suitable format. There are three principal methods: the velocity ratio, Taylor and Froude methods. In this study, the velocity ratio method was mainly used. In the velocity ratio method, the iso-velocity contours are expressed as a proportion of the ship speed (U or V_s) relative to the far-field water speed in each direction (u , v , or w).

The measurement and analysis of the complex flow fields around the ship's stern play an important role in the design of energy-saving devices since the physical mechanism of ESDs can be fully understood from this analysis. The measuring or computing positions were selected according to the configuration of the propeller, rudder, and ESD. In CFD simulation, the flow field predictions for three cases, a ship without a rudder, with a normal rudder, and with RBFS were performed in a moderate range of wavelength ($\lambda/L=0.6, 1.1, \text{ and } 1.6$) with the same amplitude at three transverse planes along with the ship's length, single longitudinal plane, and one horizontal plane as illustrated in Fig 4-6.

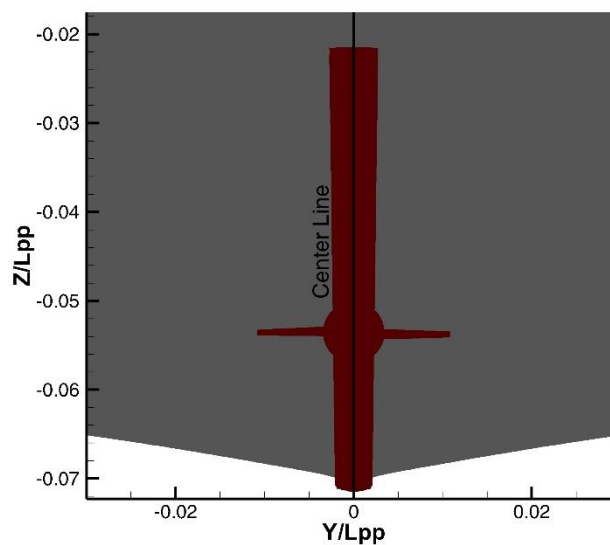
The first transverse section where wake field was computed is an $x/L=0.96875$ plane, which is 10 cm ahead of AP to check the similarity of the wake field at the upstream of the propeller. The second transverse plane is an $x/L=1$ section, which is AP's position to examine the flow field passing through the rudder fins and behind the rudder bulb. The last transverse section is an $x/L=1.025$ plane, which is downstream of the rudder to confirm the effect of RBFS on the wake field behind the propeller and rudder. The longitudinal plane, where the wake field was investigated is at $y/L=0$ in order to see the characteristics of the viscous flow field along the ship's stern. Finally, the wake field analysis was done at the horizontal plane along the center line of the propeller shaft, which is crossing through the rudder bulb and fins as demonstrated in Fig 4-6. This plane cannot be defined as the exact value of coordinate since the ship is moving up and down in wave conditions.

The SPIV flow field measurement was carried out at only two transverse planes as shown in Fig 4-7 to validate the computational results. One plane is 10 cm ($x/L=0.9688$) upstream of AP and the other plane is 8cm ($x/L=1.025$) downstream of AP in order to check the pattern of the velocity field before and after the RBFS.

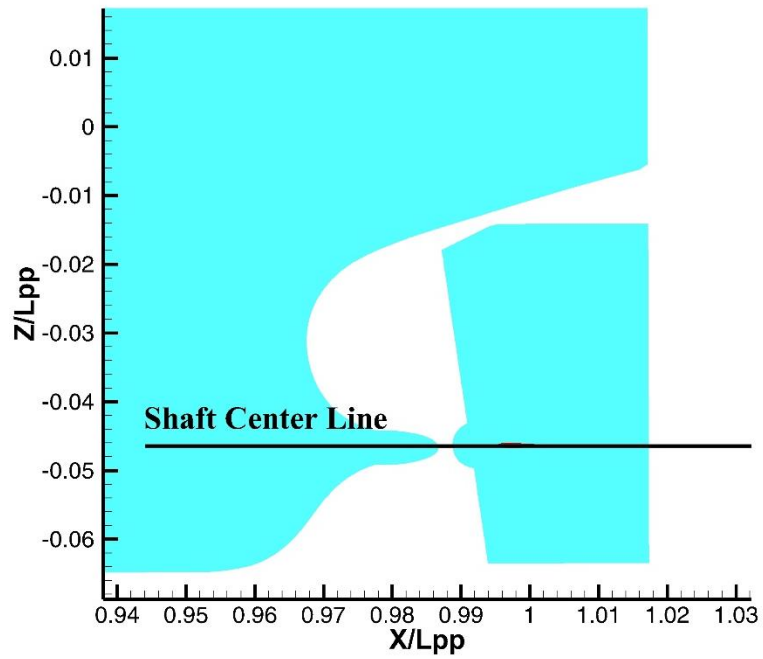
The phase-averaged flow field measurements were carried out in four phases (0deg, 90deg, 180deg, and 270deg) in $\lambda/L=0.6$ and six phases (0deg, 60deg, 120deg, 180deg, 240deg, and 300deg) in $\lambda/L=1.1$ and 1.6 to see the way of transforming the velocity field over one encounter period. These phases were allocated by the wave data measured at the wave gauge meter installed 3.33m ahead of the ship's bow.



(a) Transverse sections



(b) Longitudinal plane



(c) Horizontal plane

Fig 4-6 Positions of flow field computed in CFD

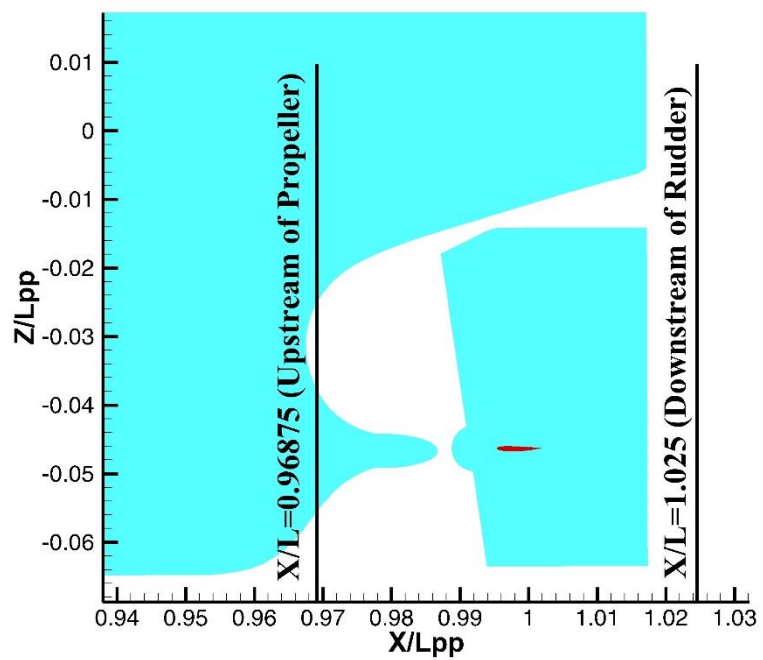


Fig 4-7 Two transverse position of flow field measured in experiment

4.2.2 Flow field at $x/L=0.96875$

To understand the detailed inflow characteristics of a propeller, the flow field comparison between a ship with a normal rudder and with RBFS at a non-dimensionalized distance of $x/L = 0.96875$ which is about 4 cm before the propeller plane as presented in Fig 4-8 was performed in three wavelengths ($\lambda/L=0.6, 1.1, \text{ and } 1.6$). The purpose of drawing the propeller upstream flow field is to confirm the similarity of velocity field between a ship with a normal rudder and RBFS.

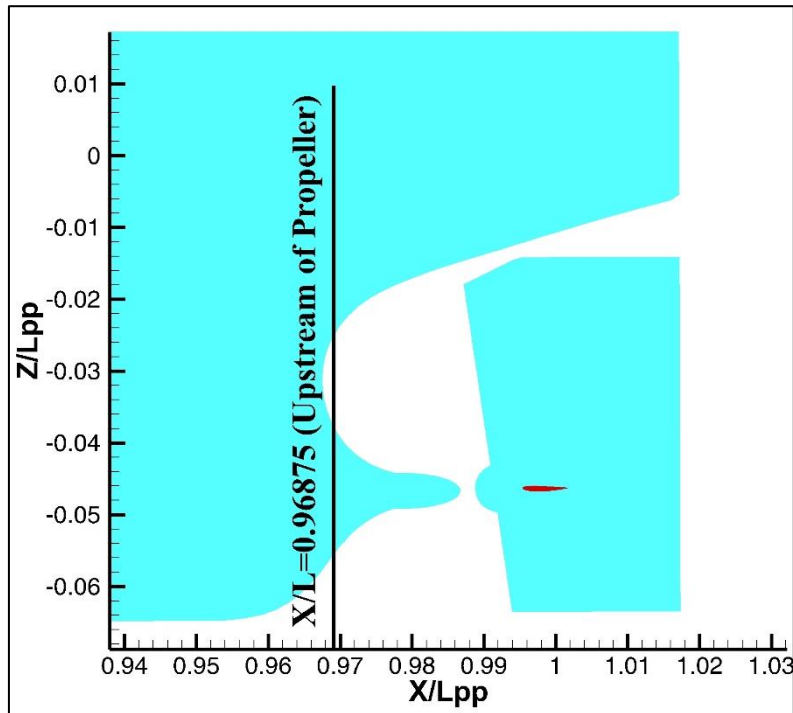


Fig 4-8 Transverse $x/L=0.96875$ plane of the velocity field measurement

The computation and measurement were carried out at four phases (0deg, 90deg, 180deg, and 270deg) in $\lambda/L = 0.6$. Fig 4-9 provides the predicted flow field by CFD and the flow field measurement in the experiment. The pictures of CFD simulation are demonstrated in left column and EFD's pictures are in right column. The left figure represents the normal rudder and the opposite side is for RBFS. X-coordinate is positive pointing towards the aft of the ship. Y-coordinate is positive toward starboard and Z is positive in upward direction. The y and z axes are non-dimensionalized by the ship length between the perpendiculars (L_{pp}). The wake field colored with non-dimensionalized axial velocity contour (u/V_s) is demonstrated together with the cross-flow velocity vector ($v/V_s, w/V_s$). u, v, and w are velocity components in x, y, and z directions.

In the phase-averaged velocity field at all phases, the boundary layer around the stern due to the friction of the hull and the hook-shaped vortex flow could be captured, note that the

velocity is total velocity including propeller induced velocity. The wake does not shift very much relative to the propeller shaft. It means that the ship's vertical motion is relatively small since $\lambda/L=0.6$ is a short wavelength. It has been already confirmed in the section on motion analysis. The wake fields in both port and starboard sides were almost symmetric. The flow tends to move down near the stern tube while moving upward far from the hull surface. The rotational flow was found in the upper portion of the propeller plane. In CFD simulation, low-speed contour and very small scale viscous vortex under the stern tube could be depicted in detail. Compared to the boundary layer near the hull and stern tube measured in the experiment, it was observed that CFD predicted the larger boundary layer. There was no significant difference in inflow velocity of the propeller between the normal rudder and RBF in both CFD and EFD.

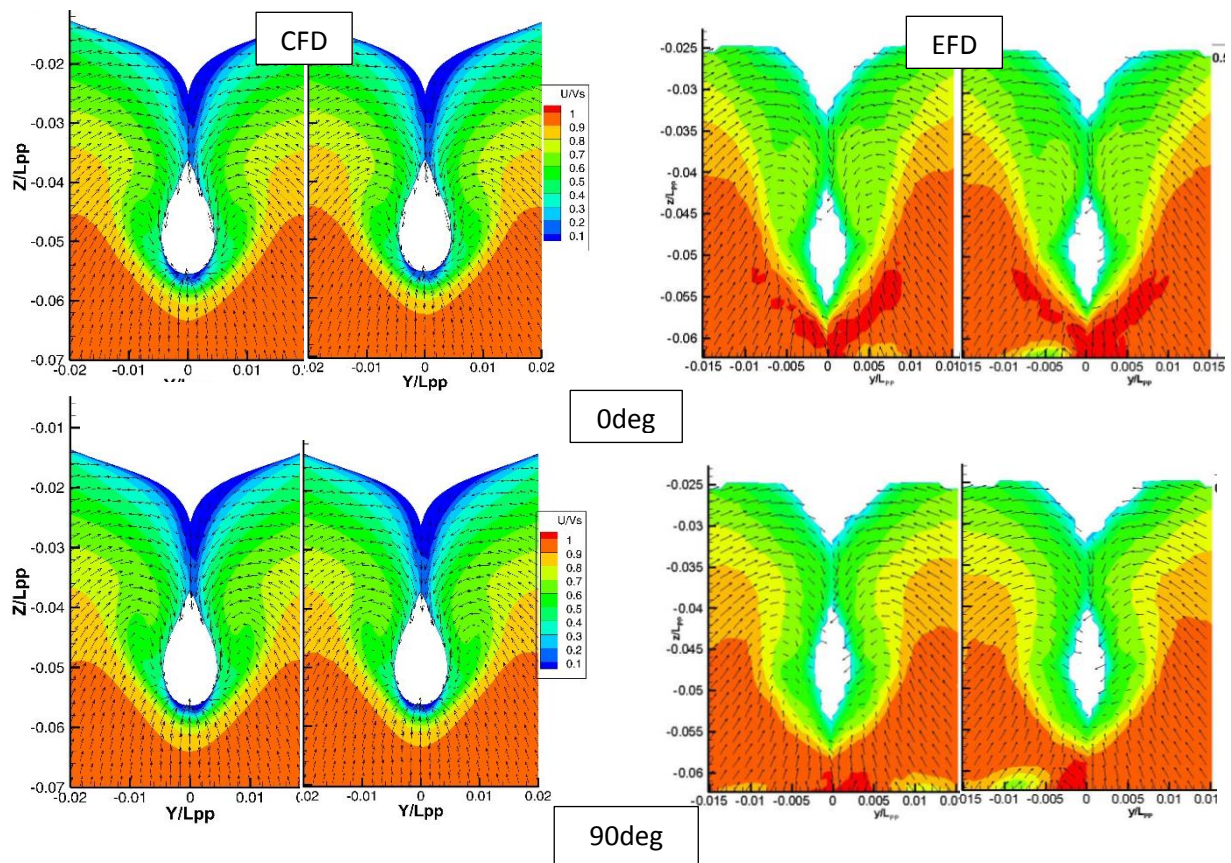


Fig 4-9 Comparison of flow field at $x/L=0.96875$ in $\lambda/L=0.6$

(Left: normal rudder and right: RBFS)

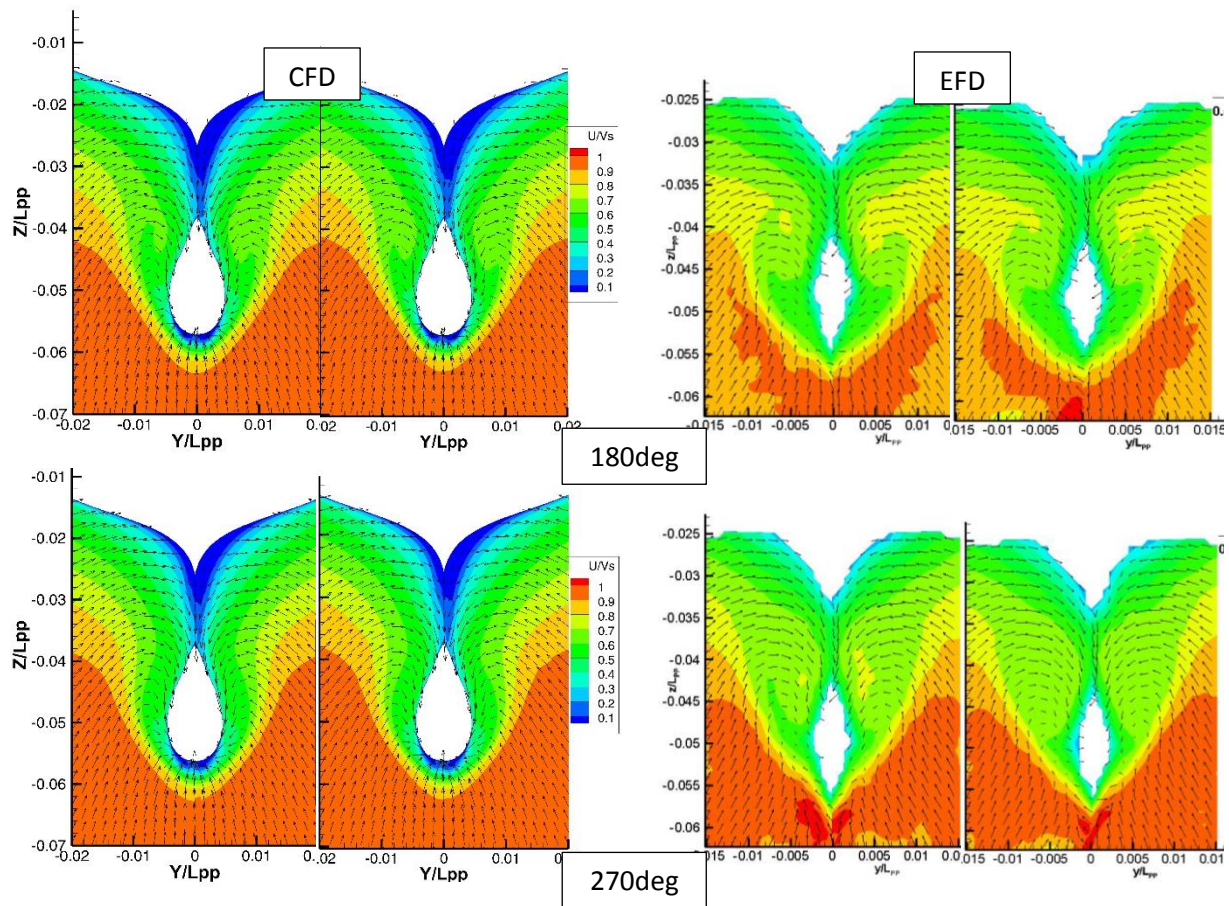


Fig 4-9 (continued)

The prediction and measurement of wake field were carried out at six phases (0deg, 60deg, 120deg, 180deg, 240deg, and 300deg) in $\lambda/L = 1.1$. Fig 4-10 provides the predicted flow field by CFD and the flow field measurement in the experiment. The pictures of CFD simulation are demonstrated in left column and EFD's pictures are in right column. The left figure represents the normal rudder and the opposite side is for RBFS. X-coordinate is positive pointing towards the aft of the ship. Y-coordinate is positive toward starboard and Z is positive in upward direction. The y and z axes are non-dimensionalized by the ship length between the perpendiculars (Lpp). The wake field colored with non-dimensionalized axial velocity contour (u/V_s) is demonstrated together with the cross-flow velocity vector ($v/V_s, w/V_s$). u, v, and w are velocity components in x, y, and z directions.

Similar to short wavelength, the boundary layer around the stern due to the friction of the hull and the hook-shaped vortex flow could be captured in the phase-averaged velocity field at all phases. The wake shift markedly relative to the propeller shaft. It means that the ship's vertical motion is relatively large since $\lambda/L=1.1$ is a medium wavelength. It has been already confirmed in the section on motion analysis. The wake fields in both port and starboard sides

were almost symmetric. The flow tends to move down near the stern tube while moving upward far from the hull surface. The rotational flow was found out in the upper portion of the propeller plane. In CFD simulation, low-speed contour and very small scale viscous vortex under the stern tube could be depicted in detail. Compared to the boundary layer near the hull and stern tube measured in the experiment, it was observed that CFD predicted the larger boundary layer. There was no significant difference in inflow velocity of the propeller between the normal rudder and RBF in both CFD and EFD.

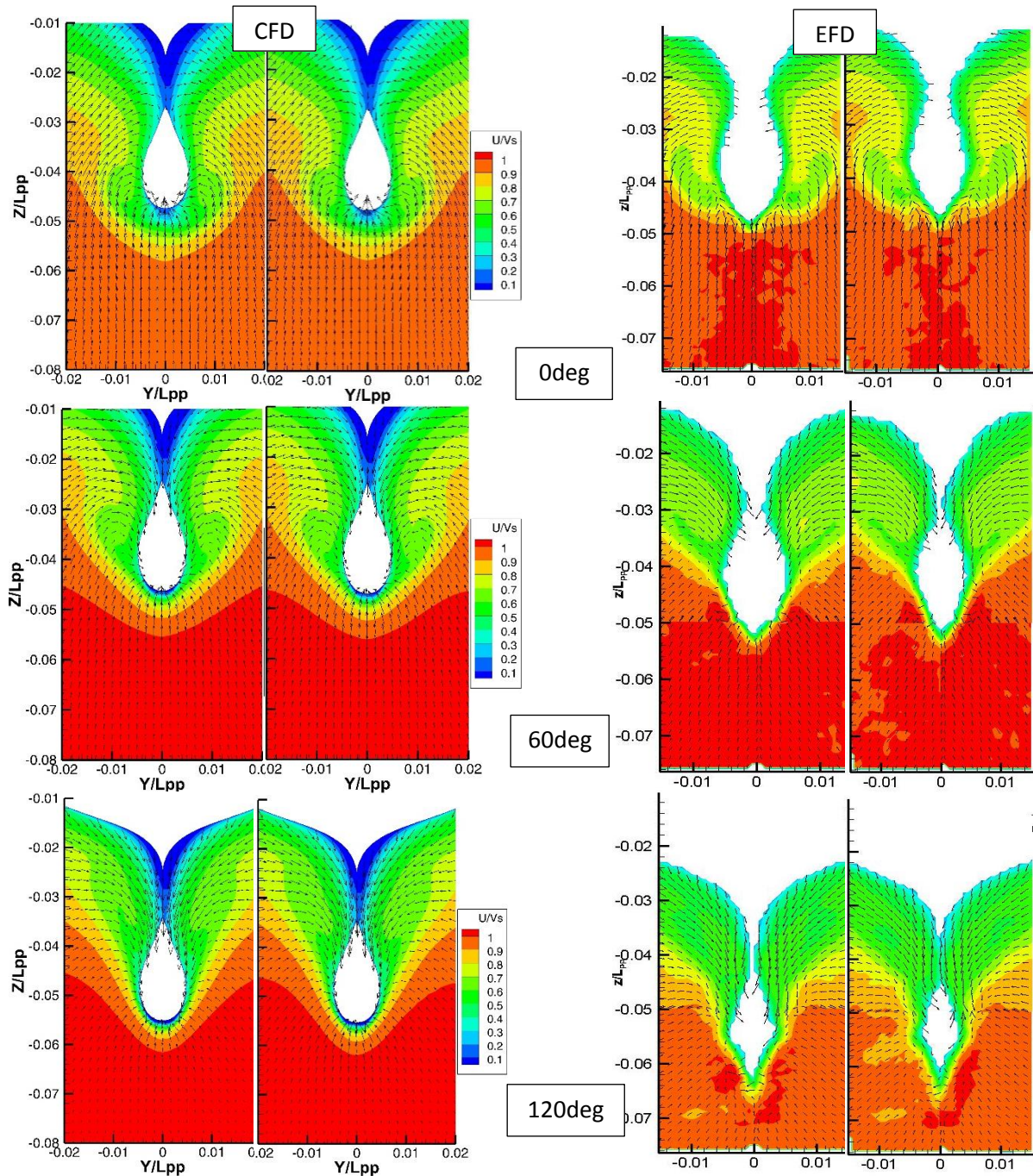


Fig 4-10 Comparison of flow field at $x/L=0.96875$ in $\lambda/L=1.1$

(Left: normal rudder and right: RBFS)

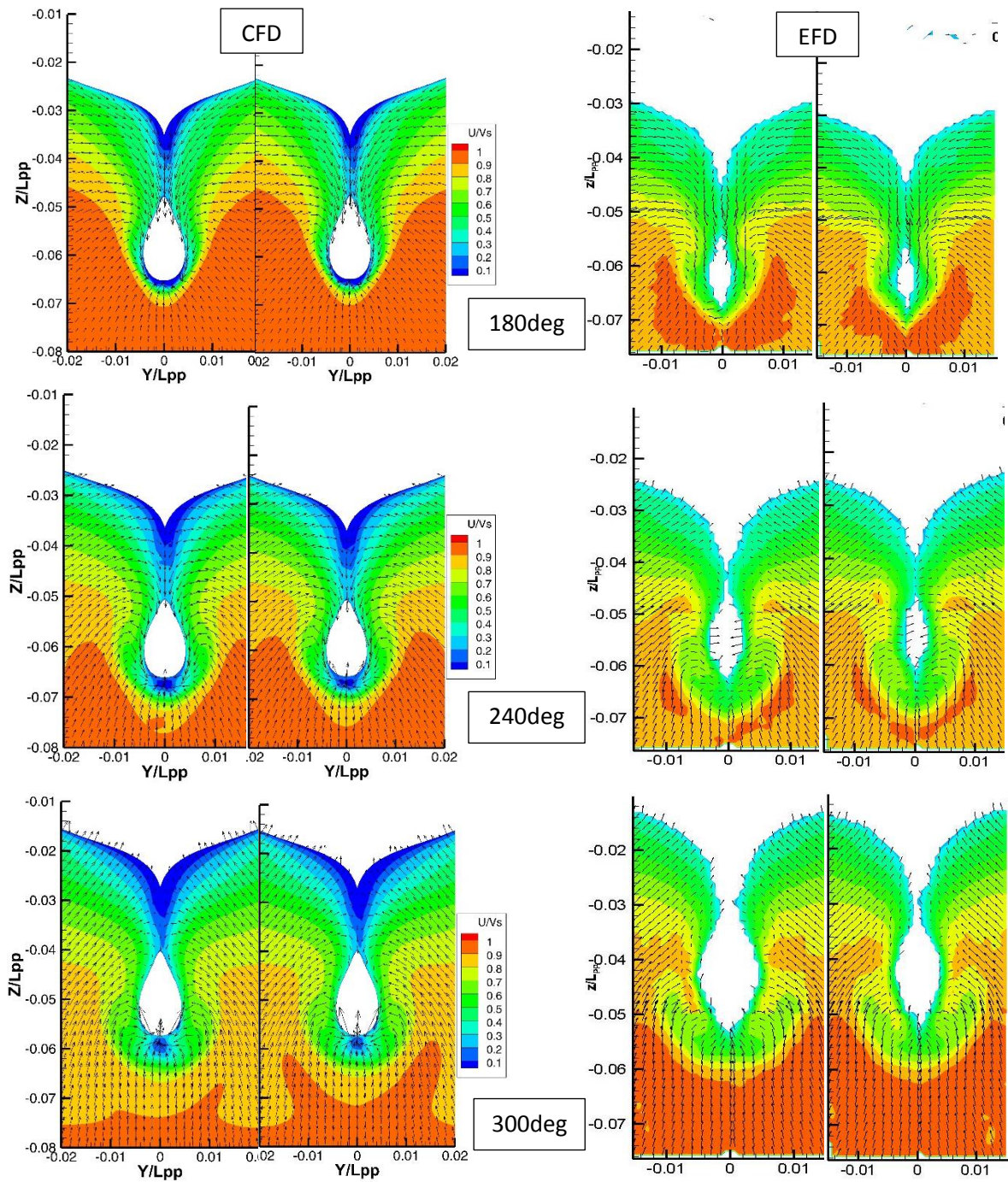


Fig 4-10 (continued)

The computation and measurement were carried out at six phases (0deg, 60deg, 120deg, 180deg, 240deg, and 300deg) in $\lambda/L = 1.6$. Fig 4-11 gives the demonstration of the predicted flow field by CFD and the flow field measurement in the experiment. The pictures of CFD simulation are demonstrated in left column and EFD's pictures are in the right column. The left figure represents the normal rudder and the opposite side is for RBFS. X-coordinate is positive pointing towards the aft of the ship. Y-coordinate is positive toward starboard and Z is positive in upward direction. The y and z axes are non-dimensionalized by the ship length between the

perpendiculars (L_{pp}). The wake field colored with non-dimensionalized axial velocity contour (u/V_s) is demonstrated together with the cross-flow velocity vector ($v/V_s, w/V_s$). $u, v,$ and w are velocity components in $x, y,$ and z directions.

The similar nature and feature of wake field of both rudder cases were predicted in long wavelength compared to the short and medium wavelengths. In contrast to the short wavelength case, the wake shift steadily relative to the propeller shaft in $\lambda/L=1.6$. It means that the ship's vertical motion becomes large since $\lambda/L=1.6$ is a long wavelength. It has been already confirmed in the section of motion analysis. In CFD simulation, low-speed contour and very small scale viscous vortex under the stern tube could be depicted in detail. Compared to the boundary layer near the hull and stern tube measured in the experiment, it was observed that CFD predicted the larger boundary layer. There was not significant difference in inflow velocity of the propeller between the normal rudder and RBF in both CFD and EFD.

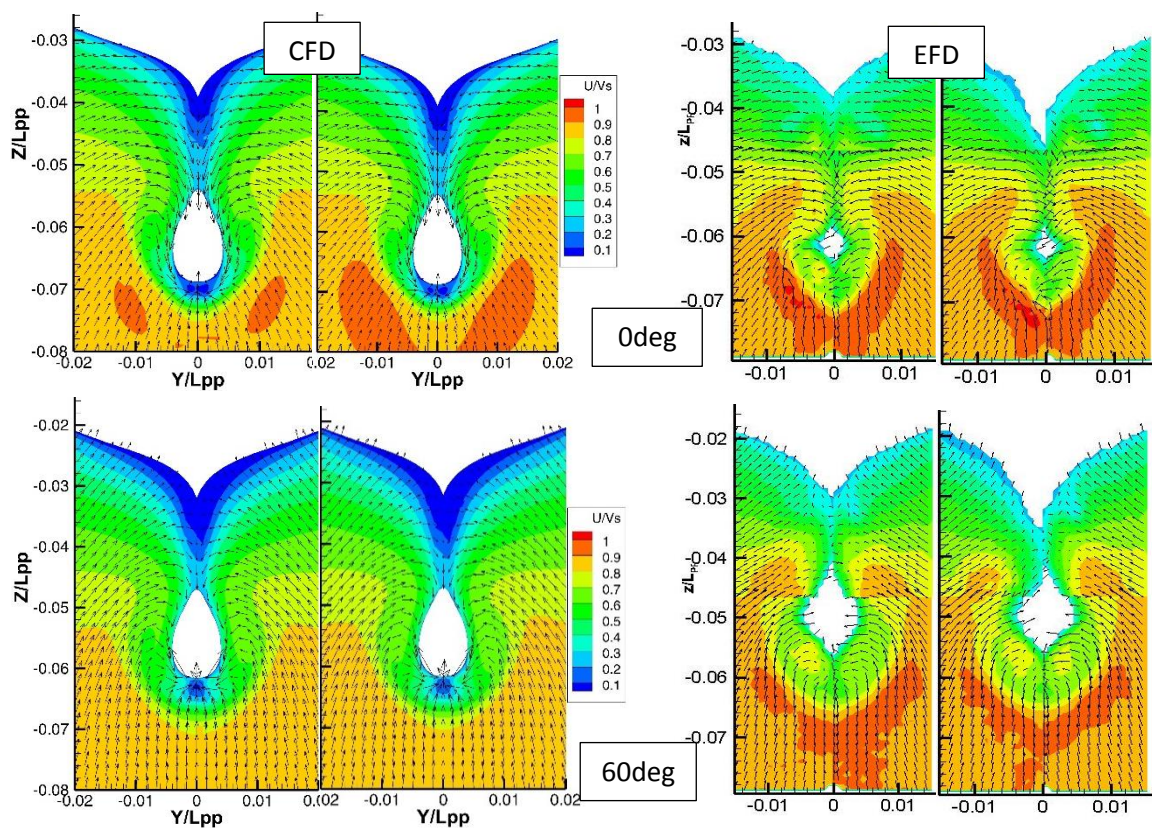


Fig 4-11 Comparison of flow field at $x/L=0.96875$ in $\lambda/L=1.6$

(Left: normal rudder and right: RBFS)

Results and Discussions

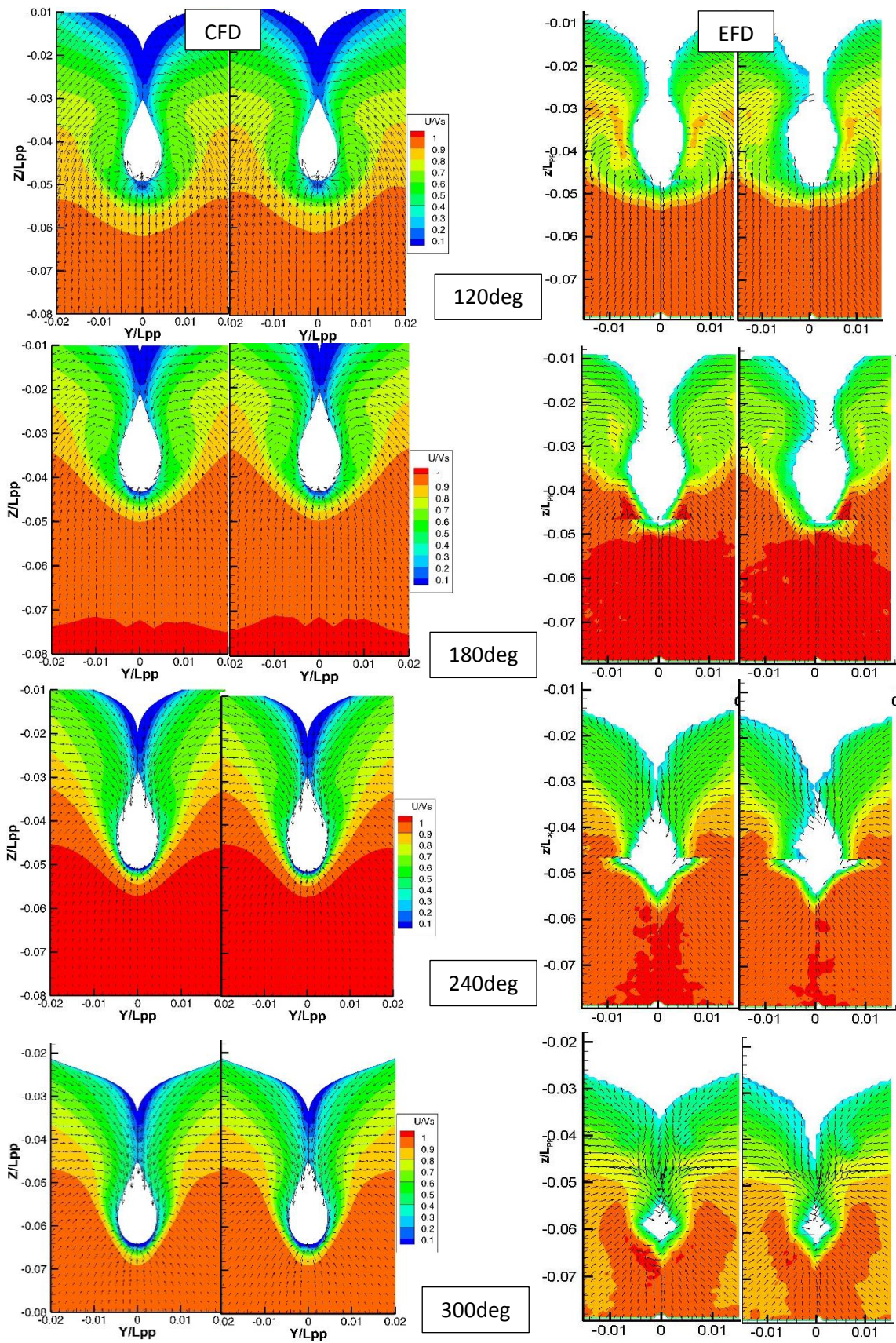


Fig 4-11 (continued)

4.2.3 Flow field at $x/L=1.0$

The analysis of flow visualizations the downstream of the propeller provides interesting details about the complex interaction between the propeller slipstream, the rudder, and bulb-fins system. The propeller induced flow field makes the rudder operate with a span wise non uniform distribution of the hydrodynamic load. To examine this phenomenon and the effectiveness of RBFS on the wake field, the phase-averaged velocity fields in three wavelengths ($\lambda/L=0.6, 1.1, \text{ and } 1.6$) were computed at $x/L=1.0$, which is an AP's position cross-sectioning the rudder fins as depicted in Fig 4-12. The small red colored line in the figure is the tip profile of the rudder fin.

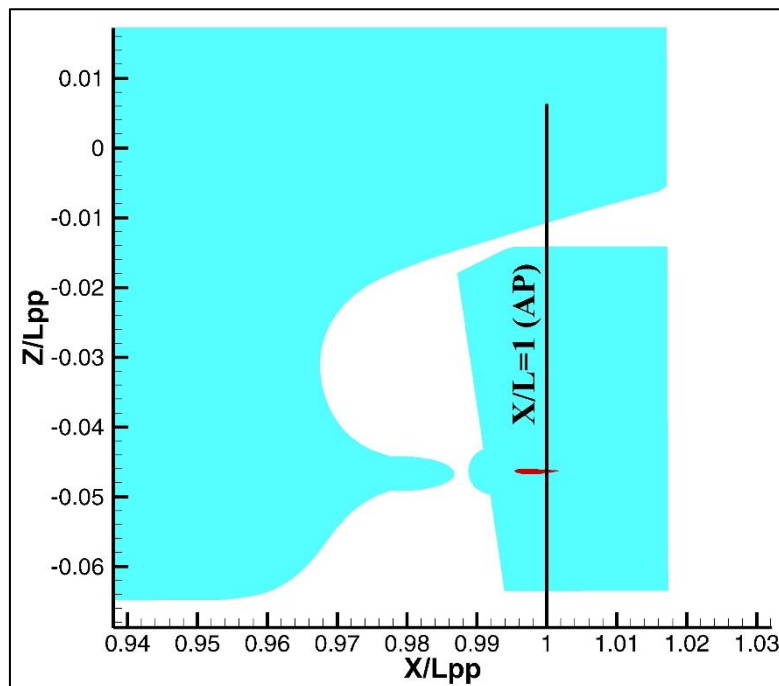


Fig 4-12 Transverse $x/L=1.0$ plane of flow field computation

Fig 4-13 shows the axial velocity contour (u/U) and cross-flow vectors ($v/U, w/U$) at $x/L=1$ for $\lambda/L=0.6$, short wave condition. The computed results of RBFS are presented in the left figures and the right figures show results of a conventional rudder. The wake fields were drawn in four phases (0deg, 90deg, 180deg, and 270deg) over one encounter period. Phase 0deg means that the wave is crossing up the zero line at the position of wave gauge meter as described in Fig 4-1.

The axial velocities were accelerated by the propeller to 1.6 times of ship's speed. The upward flow in the outer area of the flow field was observed in every single phase. On the port side of the rudder, the upward flow was strong inside the radius of the propeller and the downward flow was strong near the rudder surface. On the starboard side of the rudder, the

downward flow was found both inside the radius of the propeller and near the rudder surface. The hub vortex would tend to move toward the left side, i.e. portside, in the upward flow. That was owing to the propeller that rotates clockwise as viewed from the stern side. The vertical ship motion was relatively small in both types of the rudder. The movement and altering of the shape of velocity contour were quite small from each phase to another. The range of the high-speed contour was marginally wider in the RBFS than in the normal rudder. The hub vortex's size was shrunk a bit by rudder blub on the port side. That was an advantage of preventing cavitation and vibration of the rudder. Under the rudder fin on the starboard side, the small-scaled flow separation was observed. It may proceed the increasing of pressure drag.

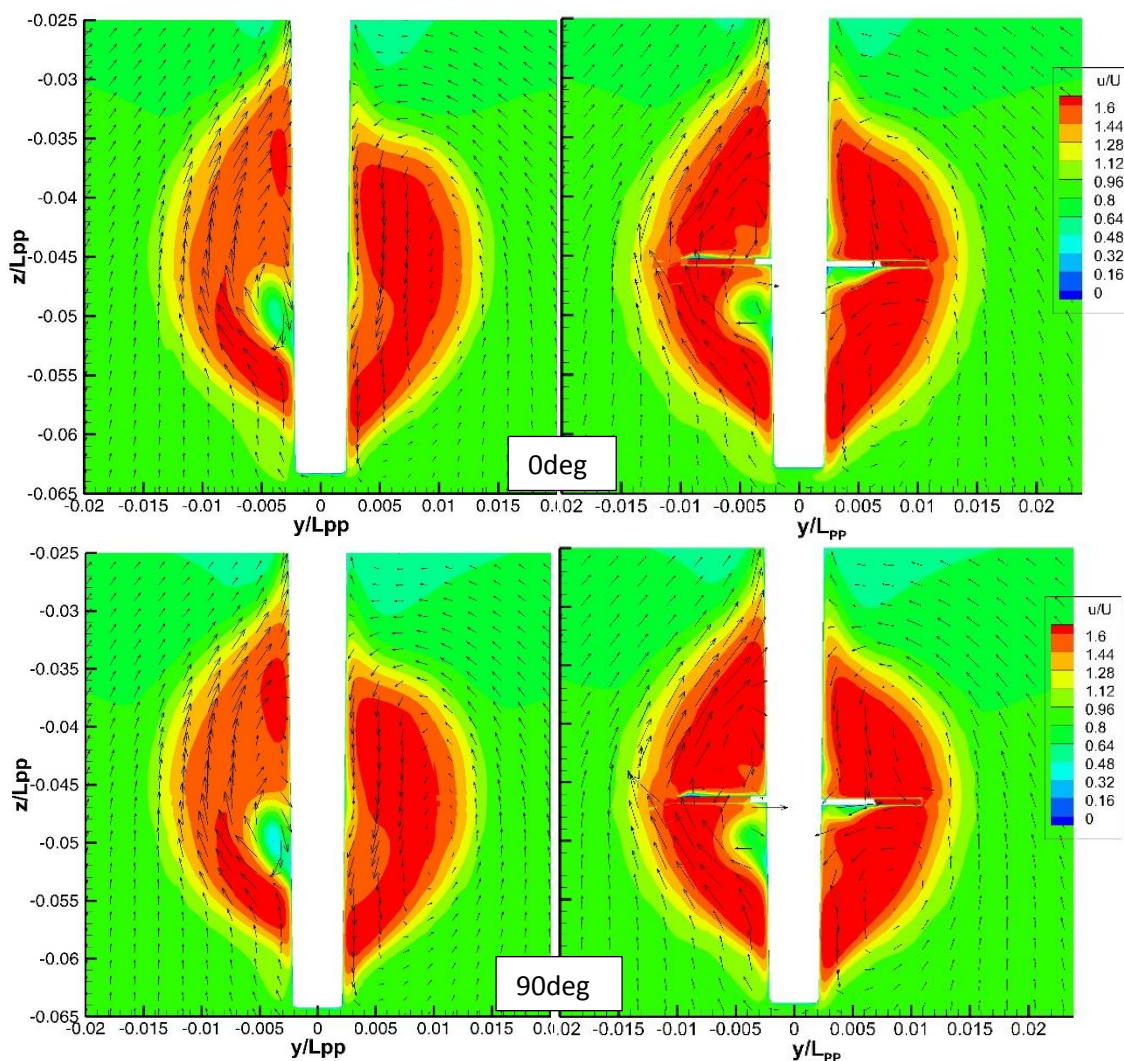


Fig 4-13 Comparison of flow field at $x/L=1.0$ in $\lambda/L=0.6$

(Left: normal rudder and right: RBFS)

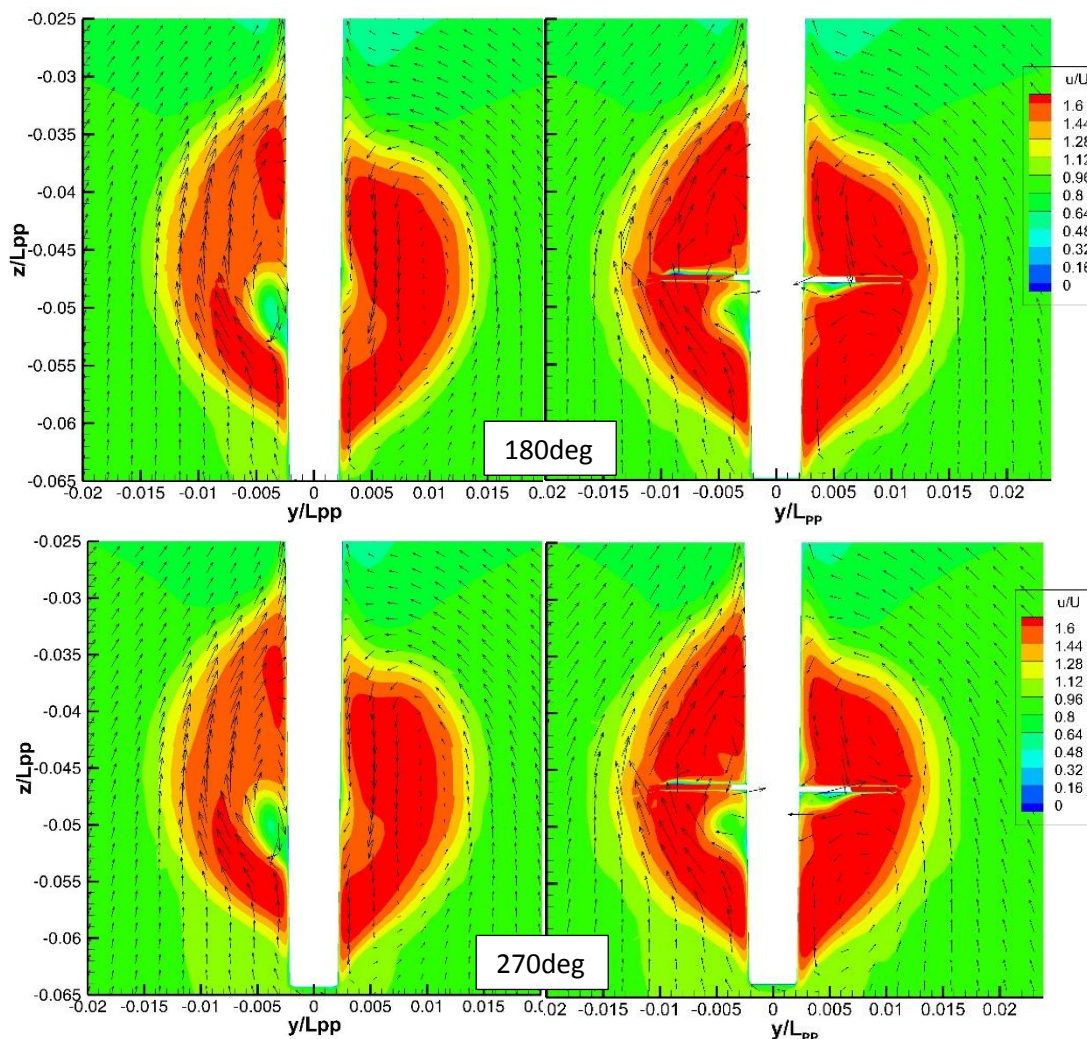


Fig 4-13 (continued)

Fig 4-14 gives illustration of the axial velocity contour (u/U) and cross flow vectors (v/U , w/U) at $x/L=1$ for $\lambda/L=1.1$, medium wave condition. The computed results of RBFS are presented in the left figures and the right figures show results of a conventional rudder. The wake fields were drawn in six phases (0deg, 60deg, 120deg, 180deg, 240deg, and 300deg) over one encounter period. Phase 0deg means that the wave is crossing up the zero line at the position of wave gauge meter as described in Fig 4-2.

In $\lambda/L=1.1$, propeller accelerated the axial velocity up to 1.6 times of ship speed as short wavelength case. Compared to the previous wavelength, the characteristics of wake field of both types of rudder were almost similar. The vertical ship motion could be seen clearly in both types of rudder. The movement and altering the shape of velocity contour were observed in each phase. Consequently, the rudder fins were encountered the rising, falling and swirling flows in the downstream of the propeller and from that phenomena, the additional thrust may

be generated. The high speed wake field was nearly circular-shaped in short wavelength but it changed to the oval-shaped in $\lambda/L=1.1$ due to the vertical movement of ship. The range of this contour is marginally wider in the RBFS than in the normal rudder. The hub vortex's size was shrunk a bit by rudder blub on the port side in the same way of short wavelength. In the port side rudder fin, the small-scaled flow separation was observed especially in the 120deg and 180deg phases. It may proceed the increasing of pressure drag.

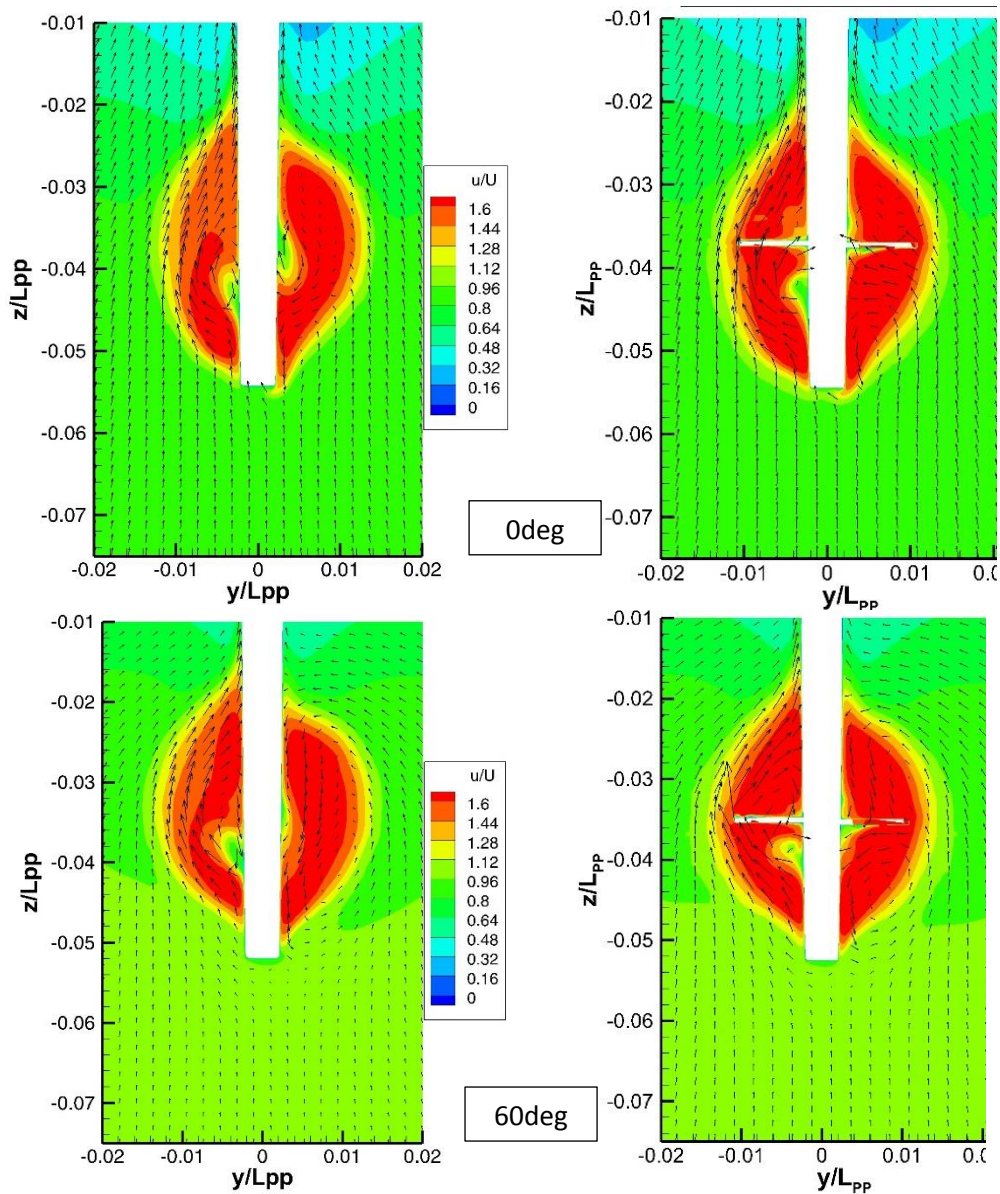


Fig 4-14 Comparison of flow field at $x/L=1.0$ in $\lambda/L=1.1$
 (Left: normal rudder and right: RBFS)

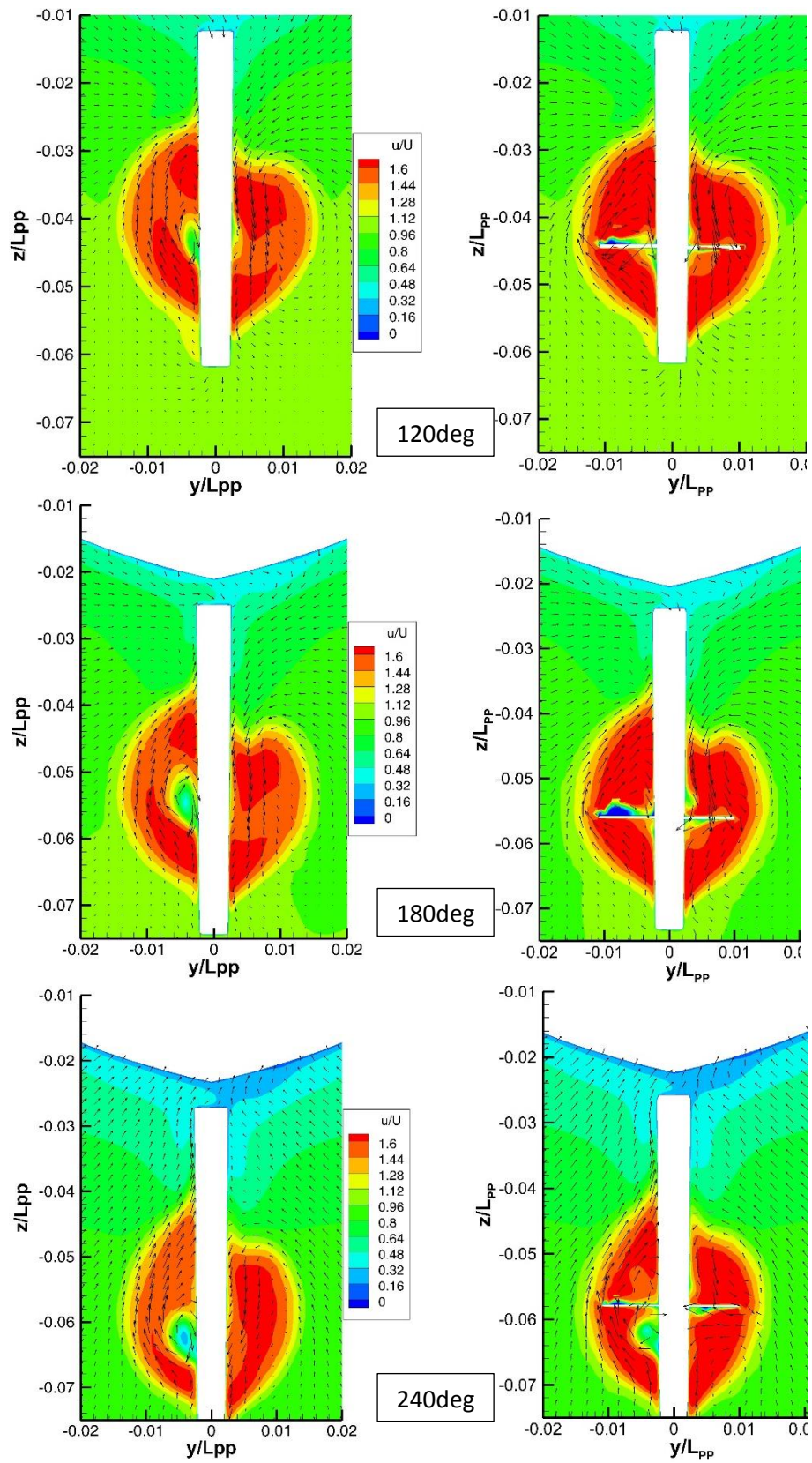


Fig 4-14 (continued)

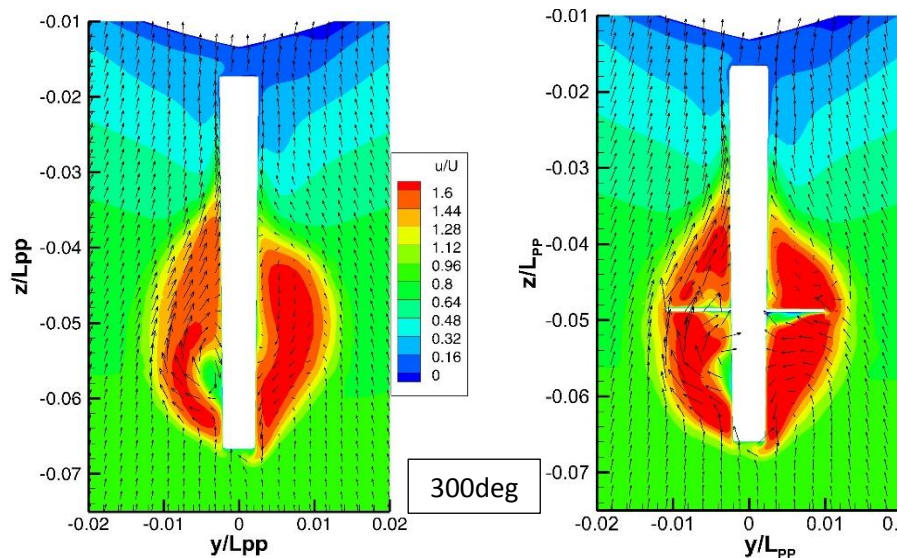


Fig 4-14 (continued)

Fig 4-15 provides illustration of the axial velocity contour (u/U) and cross flow vectors (v/U , w/U) at $x/L = 1$ for $\lambda/L = 1.6$, long wave condition. The computed results of RBFS are presented in the left figures and the right figures show results of a conventional rudder. The wake fields were drawn in six phases (0deg, 60deg, 120deg, 180deg, 240deg and 300deg) over one encounter period. Phase 0deg means that the wave is crossing up the zero line at the position of wave gauge meter as described in Fig 4-3.

The axial velocities were accelerated by the propeller to 1.6 times of ship speed. The upward flow in the outer area of the flow field was observed in each and single phase. At the port side of the rudder, the upward flow was strong inside the radius of propeller and the downward flow was strong near the rudder surface. In the starboard side of the rudder, the downward flow was found both inside the radius of propeller and near the rudder surface. The hub vortex would tend to move toward the left side, i.e. portside, in the upward flow. That was owing to the propeller that rotates clockwise as viewed from the stern side. The vertical ship motion could be seen clearly in both types of rudder. The movement and altering the shape of velocity contour were observed in each phase. Consequently, the rudder fins were encountered the rising, falling and swirling flows in the downstream of the propeller and from that phenomena, the additional thrust may be generated. The range of the high speed contour is marginally wider in the RBFS than in the normal rudder. The hub vortex's size was shrunk a bit by rudder blub on the port side. That was an advantage of preventing cavitation and vibration of rudder. In the port side rudder fin, the small-scaled flow separation was observed especially in the 0deg and 300deg phases. It may proceed the increasing of pressure drag.

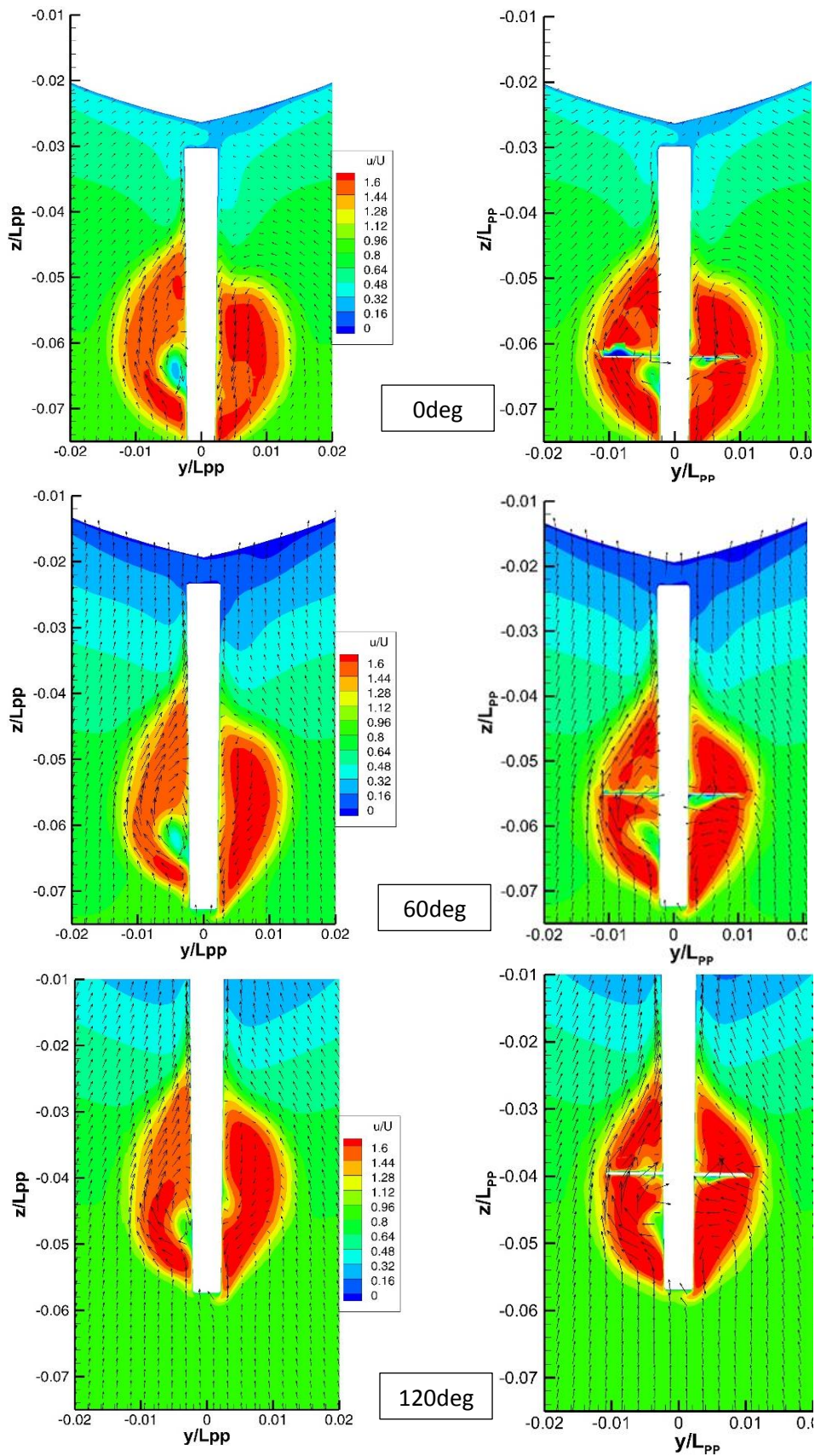


Fig 4-15 Comparison of flow field at $x/L=1.0$ in $\lambda/L=1.6$

(Left: normal rudder and right: RBFS)

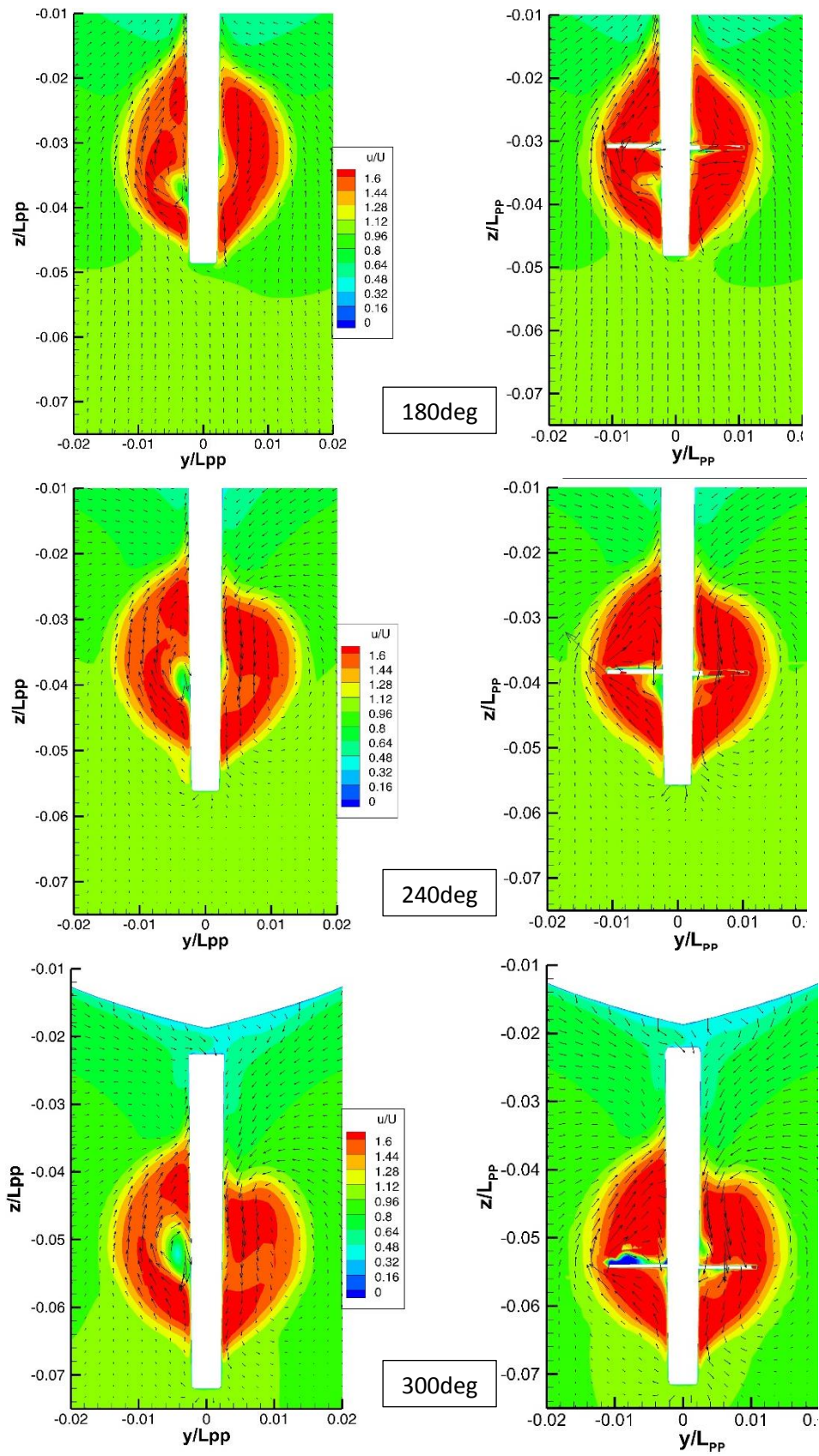


Fig 4-15 (continued)

4.2.4 Flow field at $x/L=1.025$

The viscous wake dynamics downstream of the rudder is one of the primary concerns of this research to see how much RBF can alter the wake field and is effective. For this reason, the axial velocity profile was computed in three wavelengths ($\lambda/L=0.6, 1.1, \text{ and } 1.6$) at $x/L=1.025$, which is the downstream of the rudder as described in Fig 4-16. The related SPIV flow field measurement of KVLCC2 with both normal rudder and RBFS in that plane was carried out by Mwangi (2021) and the comparison with these measured data was implemented in this study.

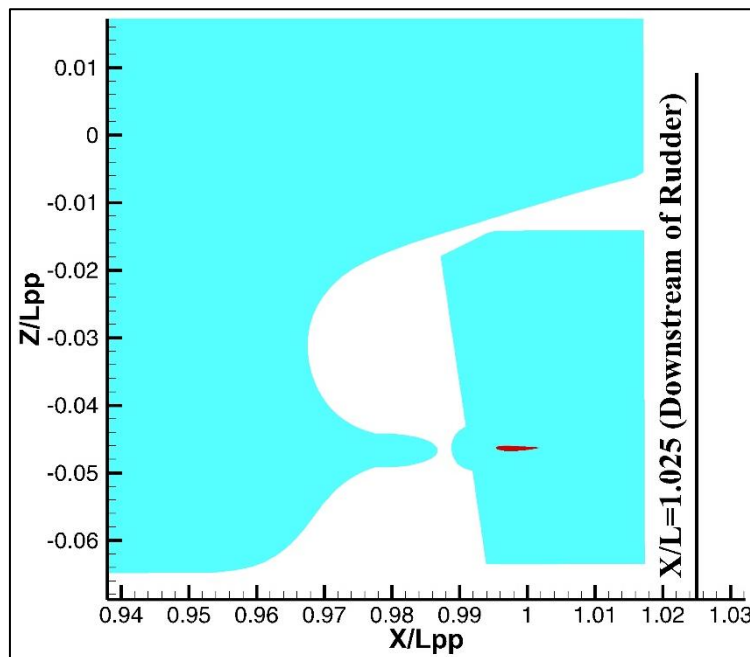


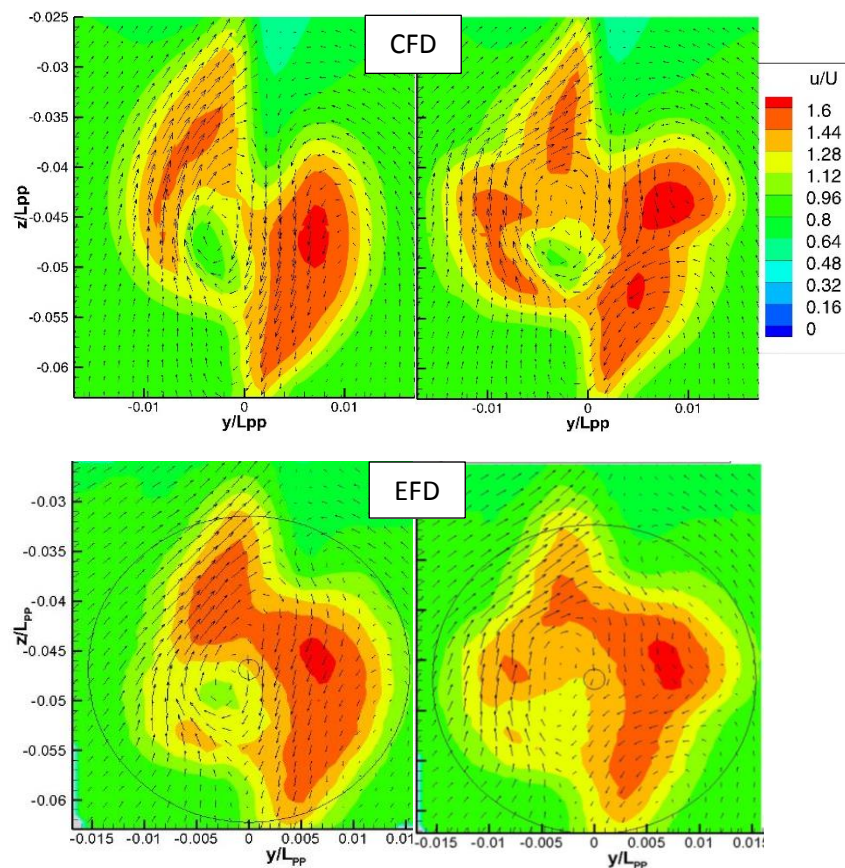
Fig 4-16 Transverse $x/L=1.025$ plane of flow field measurements

The comparison of the wake field fluctuation at $x/L = 1.025$, which is 8cm behind the AP, in $\lambda/L=0.6$ can be seen in Fig 4-17. The flow field figures are composed of the axial velocity contour (u/U) and cross-flow vectors (v/U and w/U). The left figure represents a normal rudder and the opposite one shows the RBFS. The measured phases were divided equally into four phases starting from 0deg to 270deg with an increment of 90 degree over one encounter period as shown in Fig 4-1.

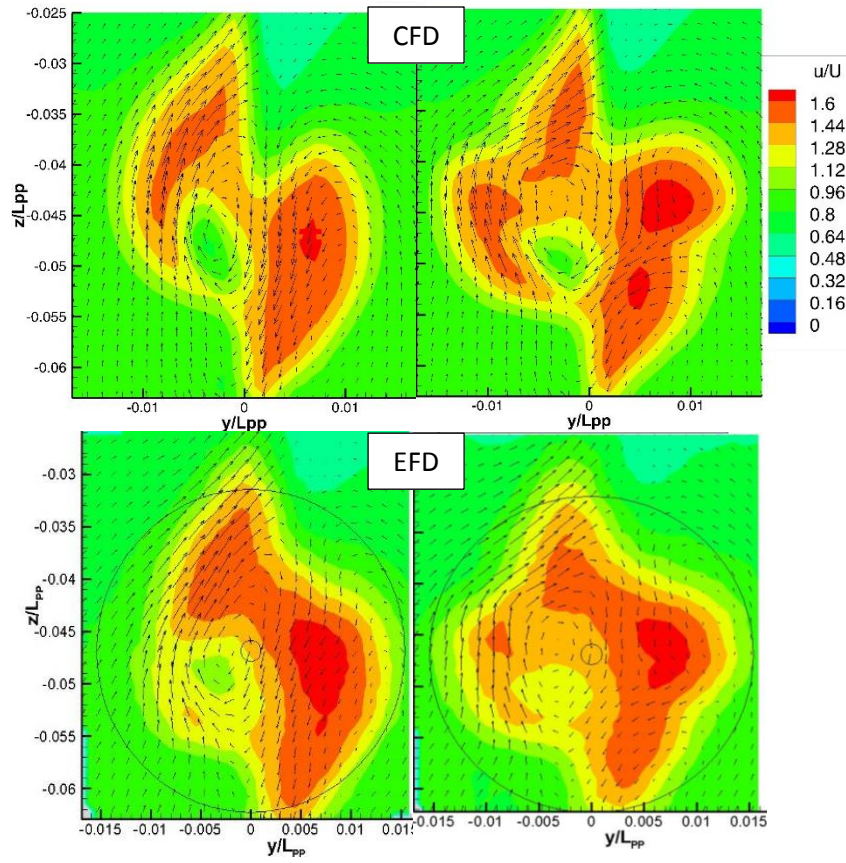
According to the small motion of a ship in the short wave, movement of the velocity contour and transformation of its shape was small in all phase diagrams. Compared to wake field in the section of $x/L=1.0$, the speed of the axial velocity became weak as the water particles moved away from the ship and propeller. The downward flow was found on the starboard side of the rudder and the flow moved upward on the port side because of the clockwise rotation of the propeller. It seems that the range of high-speed axial velocity contour

was slightly larger in the RBFS than in a conventional rudder. Compared to its smooth and round shape on a normal rudder, the shape on RBFS was twisted dramatically by the fin and the concaved shape was formed on both sides corresponding to the fin position. The propeller hub vortex was observed in both types of the rudder. Its strength and velocity around its core in the RBFS case became weak and small owing to the rudder bulb. By attenuating the hub vortex, it may reduce the vortex resistance and further improve the propulsion performance of a vessel.

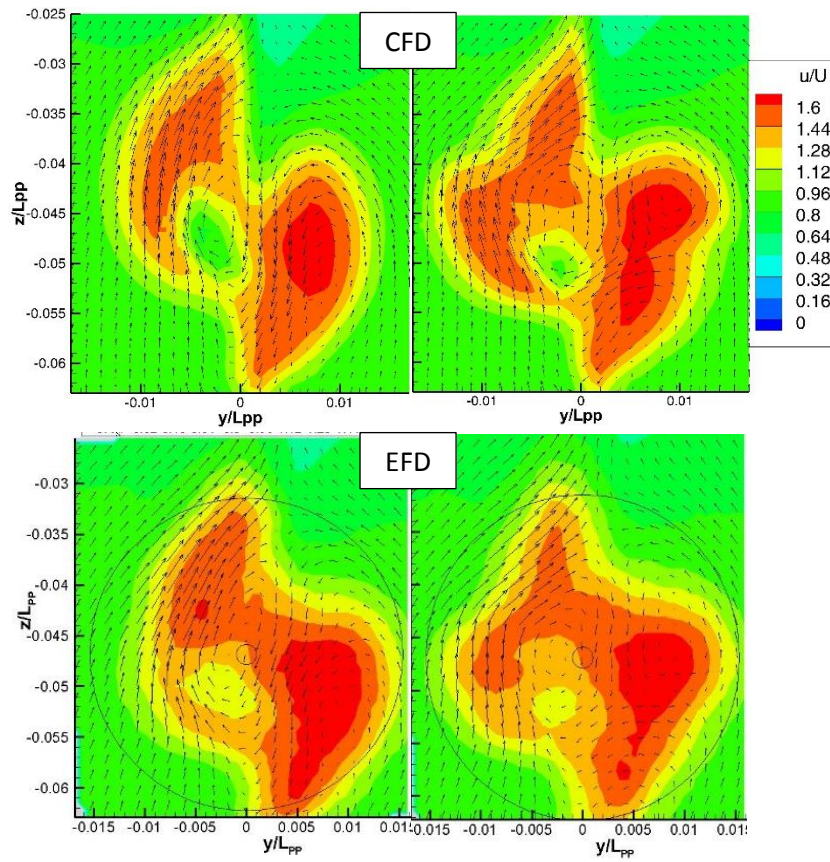
The CFD captured well the flow field characteristic in all cases in the same way as EFD measurement. In CFD simulation, the dissipation of the vortex was a bit higher due to the thin time-averaged vortex ring sheet in NS code from short term averaged body force. The velocity downstream of the propeller was lower because the resolution of the grid in that region was relatively larger as compared with the propeller grid. Therefore, the flow field of the present computations was slightly slower than the measured results.



(a) 0deg phase



(b) 90deg phase



(c) 180deg phase

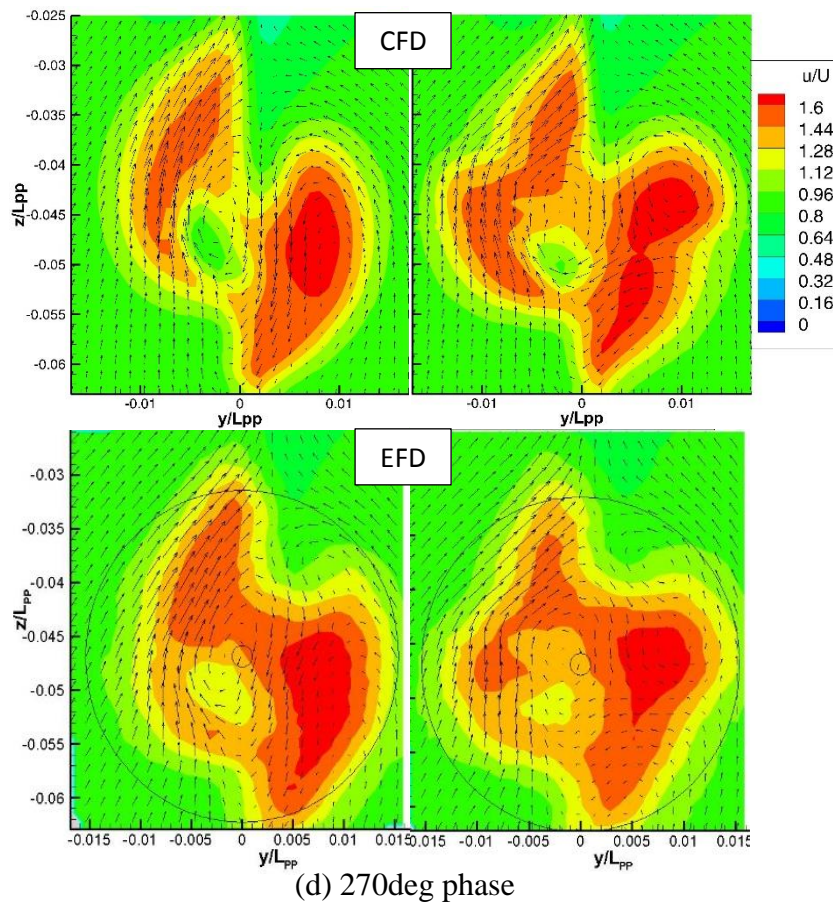


Fig 4-17 Comparison of flow field at $x/L=1.025$ in $\lambda/L=0.6$
(Left: normal rudder and right: RBFS)

The wake field fluctuation at $x/L = 1.025$, which is 8cm behind the AP, in $\lambda/L=1.1$ is compared in Fig 4-18. The flow field figures are composed of the axial velocity contour (u/U) and cross-flow vectors (v/U and w/U). The CFD results are illustrated in the left column and the measured results are shown in the right column. The left figure represents a normal rudder and the opposite one shows the RBFS. The measured phases were divided equally into six phases starting from 0deg to 300deg with an increment of 60 degree over one encounter period as shown in Fig 4-2.

Owing to the large motion of a ship in the medium wave, movement of the velocity contour and transformation of its shape could be seen clearly in each phase diagram. The change of wake field from one phase to another was relatively prominent in the contrast to that of short wavelength. Compared to wake field in the section of $x/L=1.0$, the speed of the axial velocity became weak as the water particles moved away from a ship and a propeller. The downward flow was found in the starboard side of the rudder and the flow moved upward in the port side because of the clockwise rotation of the propeller. It seems that the range of high-

speed axial velocity contour was slightly larger in the RBFS than in a conventional rudder. Compared to its smooth and round shape on a normal rudder, the shape on RBFS was twisted dramatically by the fin and the concaved shape was formed on both sides corresponding to the fin position. The propeller hub vortex was observed in both types of the rudder. Its strength and velocity around its core in the RBFS case became weak and small owing to the rudder bulb. By attenuating the hub vortex, it may reduce the vortex resistance and further improve the propulsion performance of a vessel.

Compared to the experimental measurement, CFD captured well the flow field characteristic in all cases. In CFD simulation, the dissipation of the vortex was a bit higher due to the thin time-averaged vortex ring sheet in NS code from short term averaged body force. The velocity downstream of the propeller was lower because the resolution of the grid in that region was relatively larger as compared with the propeller grid. Therefore, the flow field of the present computations was slightly slower than the measured results in $\lambda/L=1.1$.

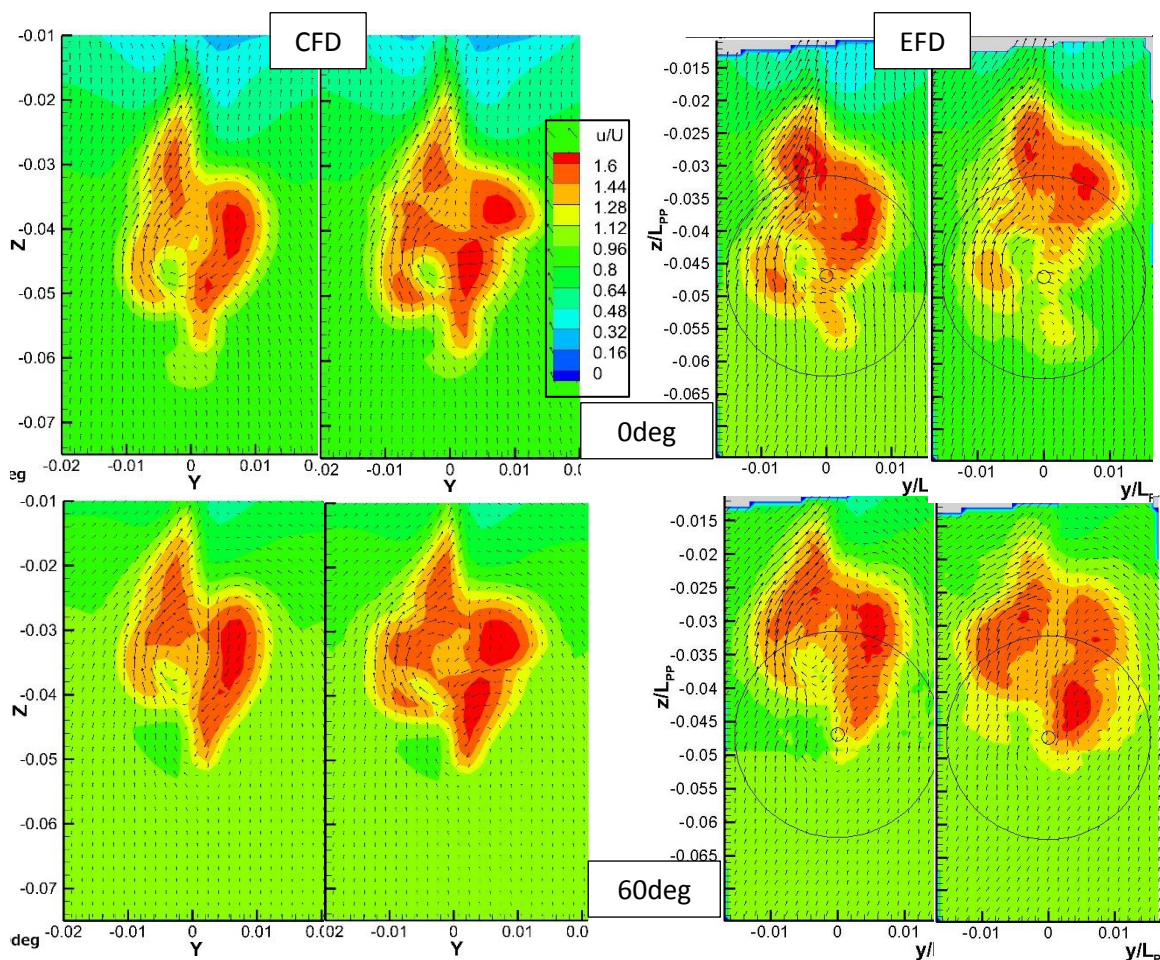


Fig 4-18 Comparison of flow field at $x/L=1.025$ in $\lambda/L=1.1$

(Left: normal rudder and right: RBFS)

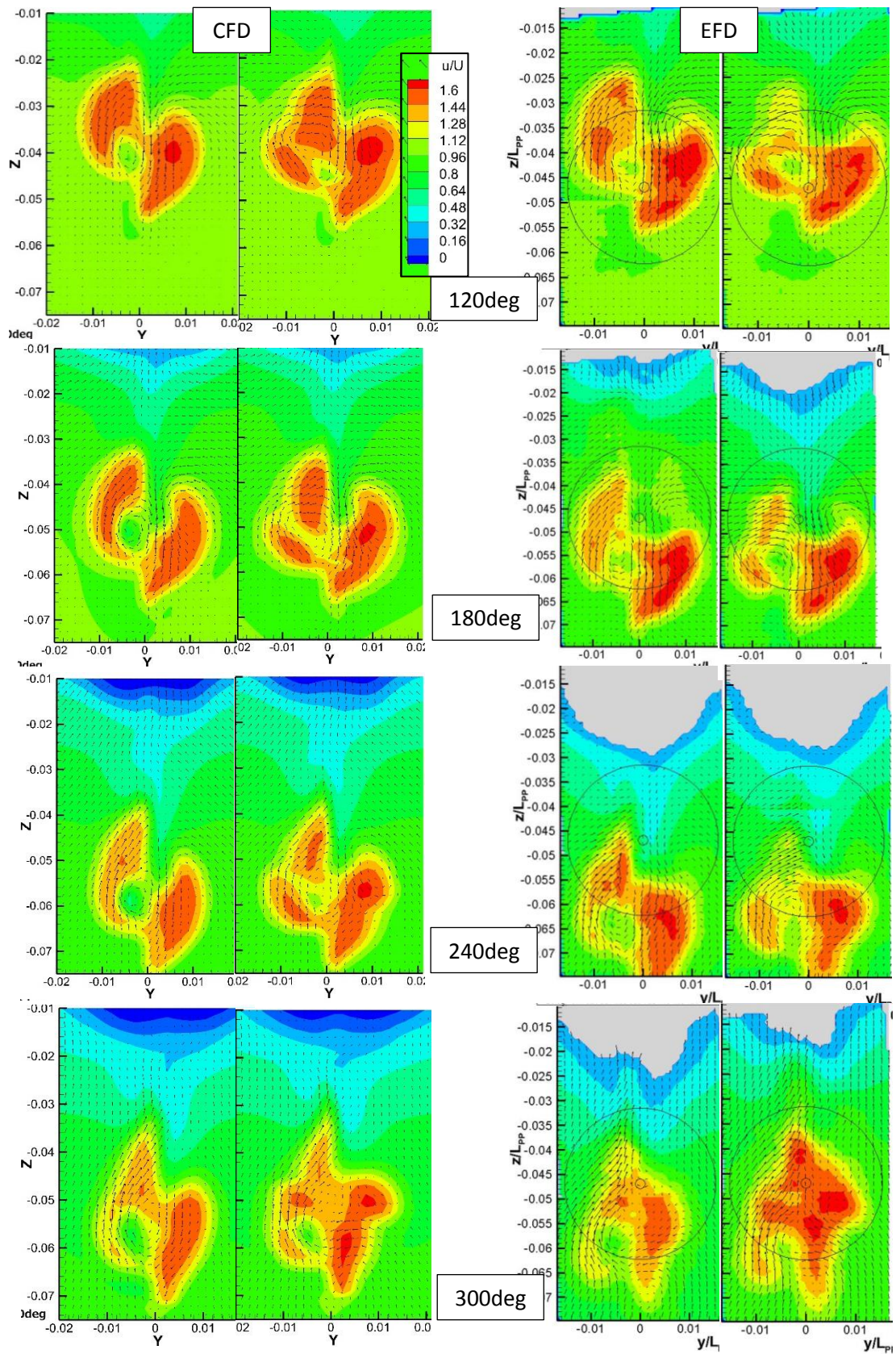


Fig 4-18 (continued)

The comparison of the wake field fluctuation at $x/L = 1.025$, which is 8cm behind the AP, in $\lambda/L=1.6$ was presented in Fig 4-19. The flow field figures are composed of the axial velocity contour (u/U) and cross-flow vectors (v/U and w/U). The CFD results are illustrated in the left column and the measured results are shown in the right column. The left figure represents a normal rudder and the opposite one shows the RBFS. The measured phases were divided equally into six phases starting from 0deg to 300deg with an increment of 60 degree over one encounter period as shown in Fig 4-3.

Due to the strong vertical motion of a ship in the long wave, movement of the velocity contour and transformation of its shape could be seen clearly in each phase diagram. Its change from one phase to another was largest in $\lambda/L=1.6$. Compared to wake field in the section of $x/L=1.0$, the speed of the axial velocity became weak as the water particles moved away from the ship and propeller. The downward flow was found on the starboard side of the rudder and the flow moved upward on the port side because of the clockwise rotation of the propeller. It seems that the range of high-speed axial velocity contour was slightly larger in the RBFS than in a conventional rudder. Compared to its smooth and round shape on a normal rudder, the shape on RBFS was twisted dramatically by the fin and the concaved shape was formed on both sides corresponding to the fin position. The propeller hub vortex was observed in both types of the rudder. Its strength and velocity around its core in the RBFS case became weak and small owing to the rudder bulb. By attenuating the hub vortex, it may reduce the vortex resistance and further improve the propulsion performance of a vessel.

In long wavelength case, CFD captured well the flow field characteristic in all cases in the same way as measurement. In CFD simulation, the dissipation of the vortex was a bit higher due to the thin time-averaged vortex ring sheet in NS code from short term averaged body force. The velocity downstream of the propeller was lower because the resolution of the grid in that region was relatively larger as compared to the propeller grid. Therefore, the flow field of the present computations was slightly slower than the measured results in $\lambda/L=1.6$.

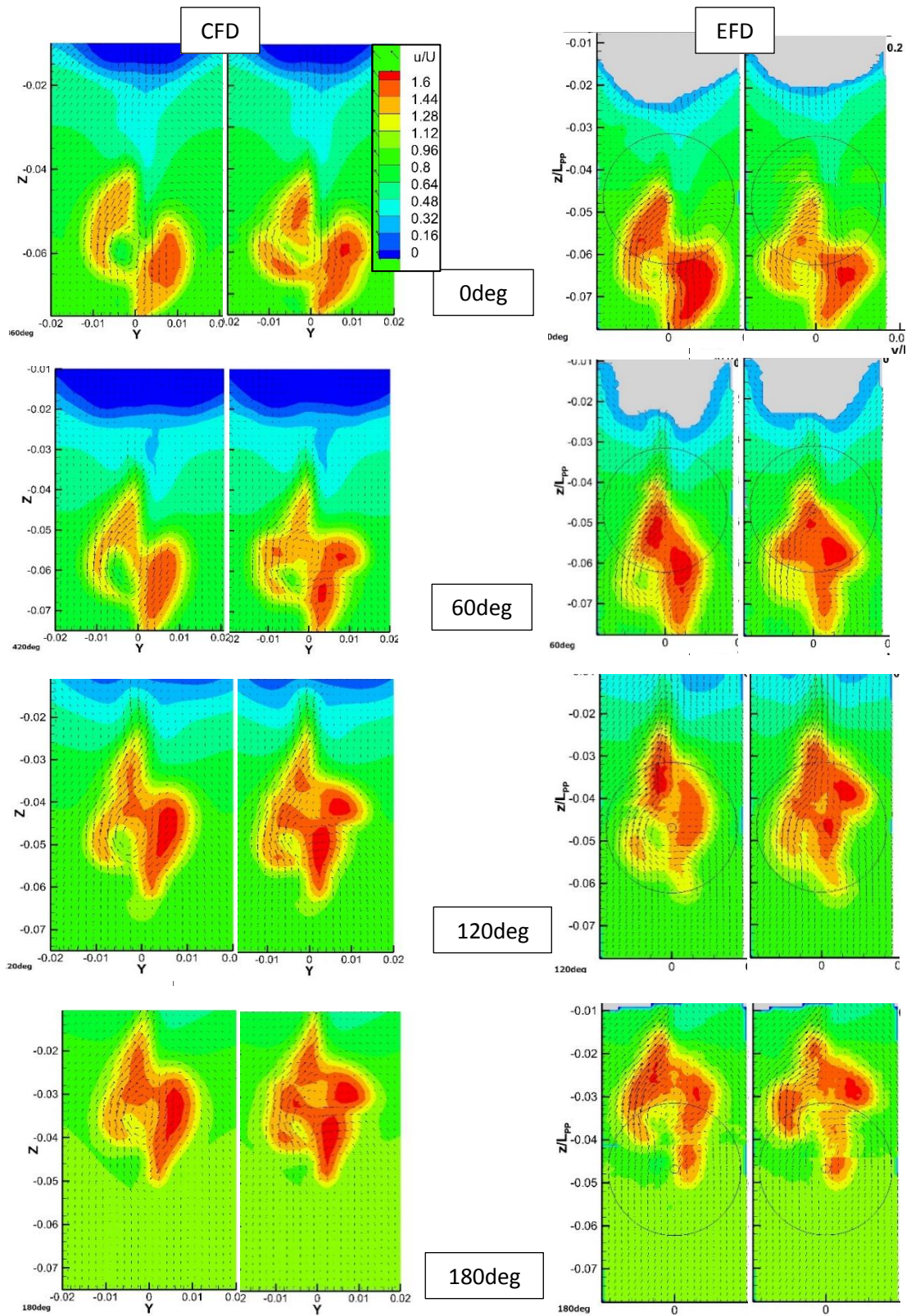


Fig 4-19 Comparison of flow field at $x/L=1.025$ in $\lambda/L=1.6$

(Left: normal rudder and right: RBFS)

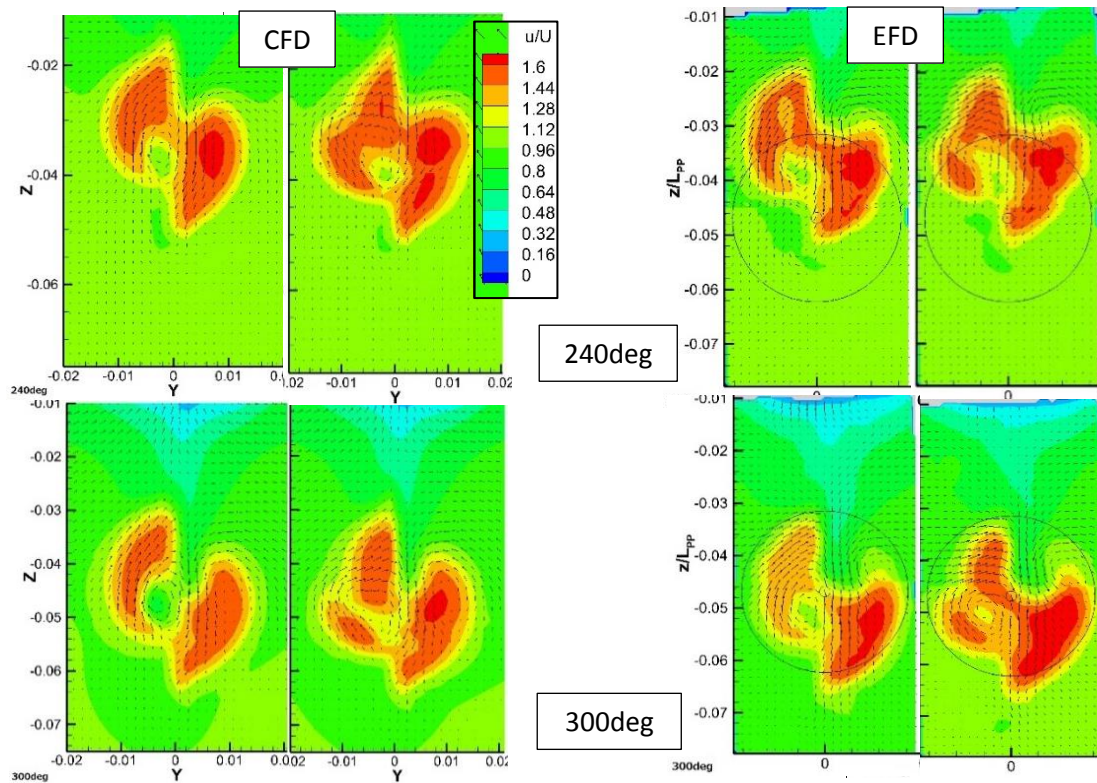


Fig 4-19 (continued)

4.2.5 Flow field at $y/L=0$

To scrutinize the nature of wake field along with the ship's stern and the hub vortex the downstream of the propeller, the longitudinal axial velocity profile was computed in three wavelengths ($\lambda/L=0.6, 1.1, \text{ and } 1.6$) at $y/L=0$ that is a center plane of a ship as demonstrated in Fig 4-20. The investigation of the viscous flow field at that cross-section was carried out only in the CFD simulation but not in the experiment.

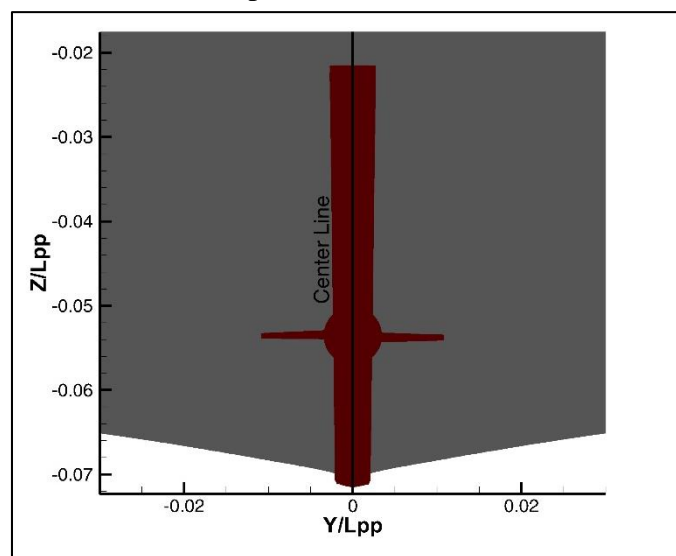


Fig 4-20 Longitudinal $y/L=0$ plane of flow field predicted

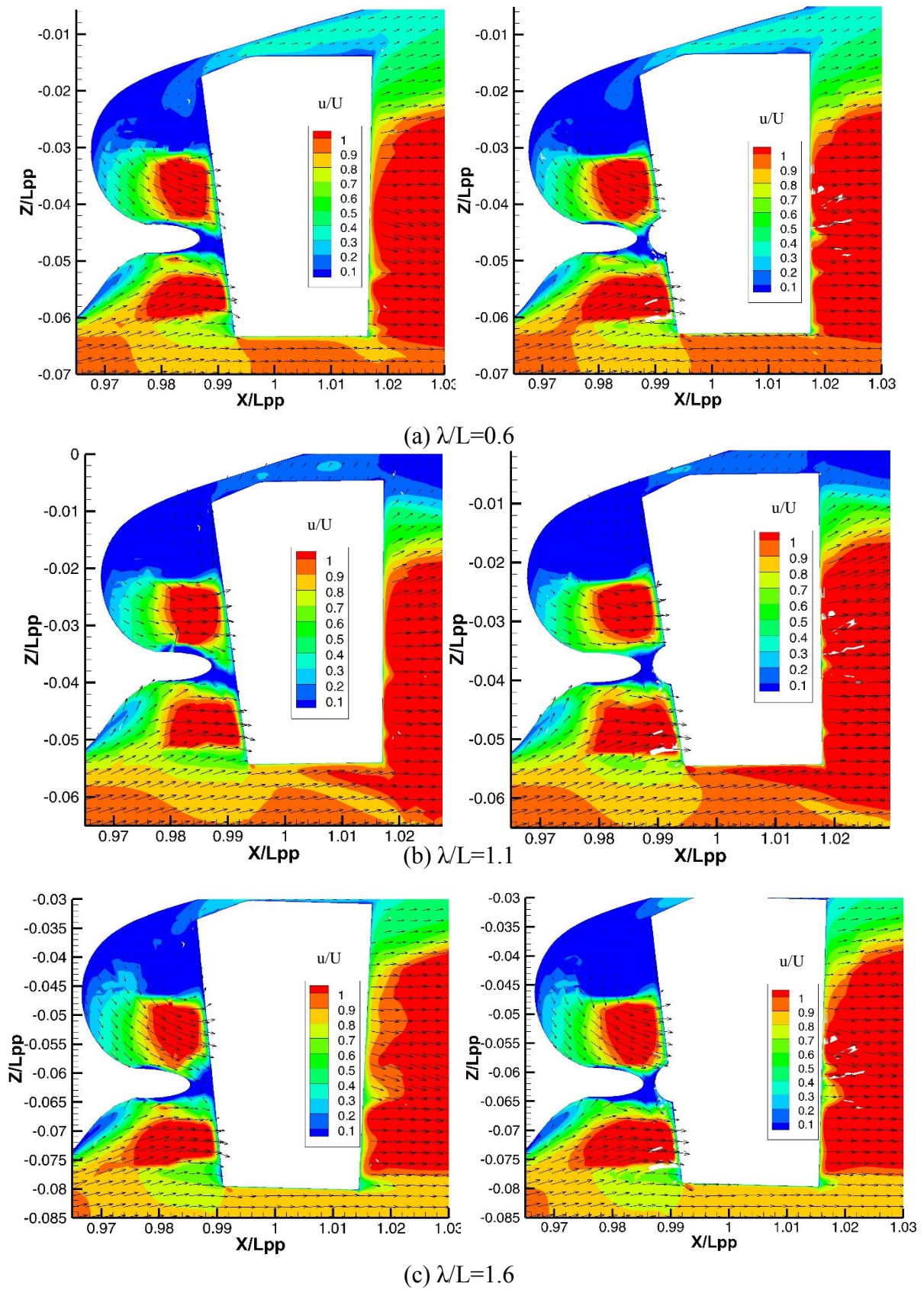


Fig 4-21 Comparison of flow field at $y/L=0$

(Left: normal rudder and right: RBFS)

Fig 4-21 reveals the comparison of wake field between normal rudder and RBFS at $y/L=0$ in $\lambda/L=0.6, 1.1, \text{ and } 1.6$. The flow field figures feature the axial velocity contour (u/U) and cross flow vectors (u/U and w/U). The left figure represents a normal rudder and the opposite one shows the RBFS. The flow field was computed at phase 0deg , which is the zero crossing up of wave at wave gauge in each wavelength.

The direction of the axial velocity followed the curvature of the surface. The hub vortex moved and deformed to a shape that resembles that of the rudder profile (RBF or conventional rudder). This phenomenon, due to the effect of viscosity, is accompanied by the diffusion of vorticity from the vortex filaments and that within the rudder boundary. It could be seen that the flow was accelerated to enhance the effectiveness of the rudder while the rudder was behind the propeller slipstream. The area of the high-speed region was inconsiderably wider in RBFS than in a normal rudder in all wavelengths.

4.2.6 Flow field at horizontal plane

The wake field analysis was performed horizontally along the center line of the propeller shaft, which is crossing through the rudder bulb and fins as demonstrated in Fig 4-22, in $\lambda/L=0.6, 1.1, \text{ and } 1.6$. This plane cannot be defined with the single exact value of coordinate for all wave cases since the ship's vertical movement is different in each wave case. A small red colored part is a tip profile of the rudder fin.

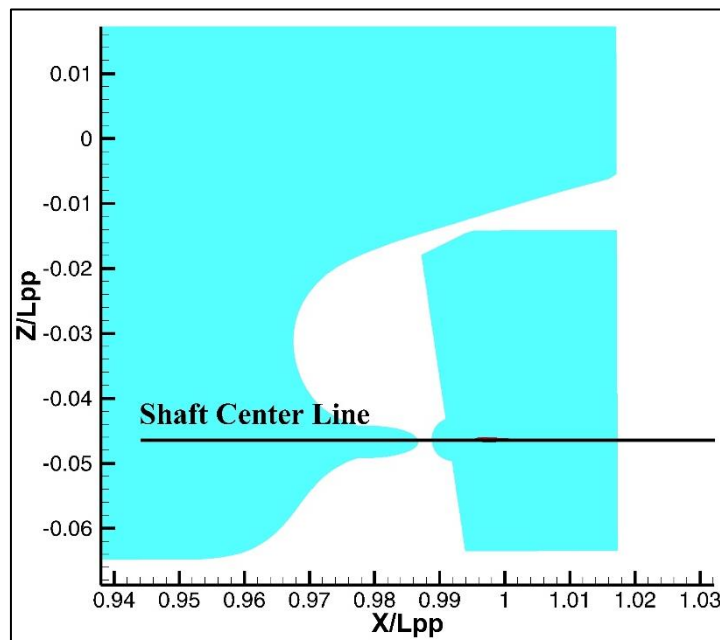


Fig 4-22 Horizontal plane of flow field computed

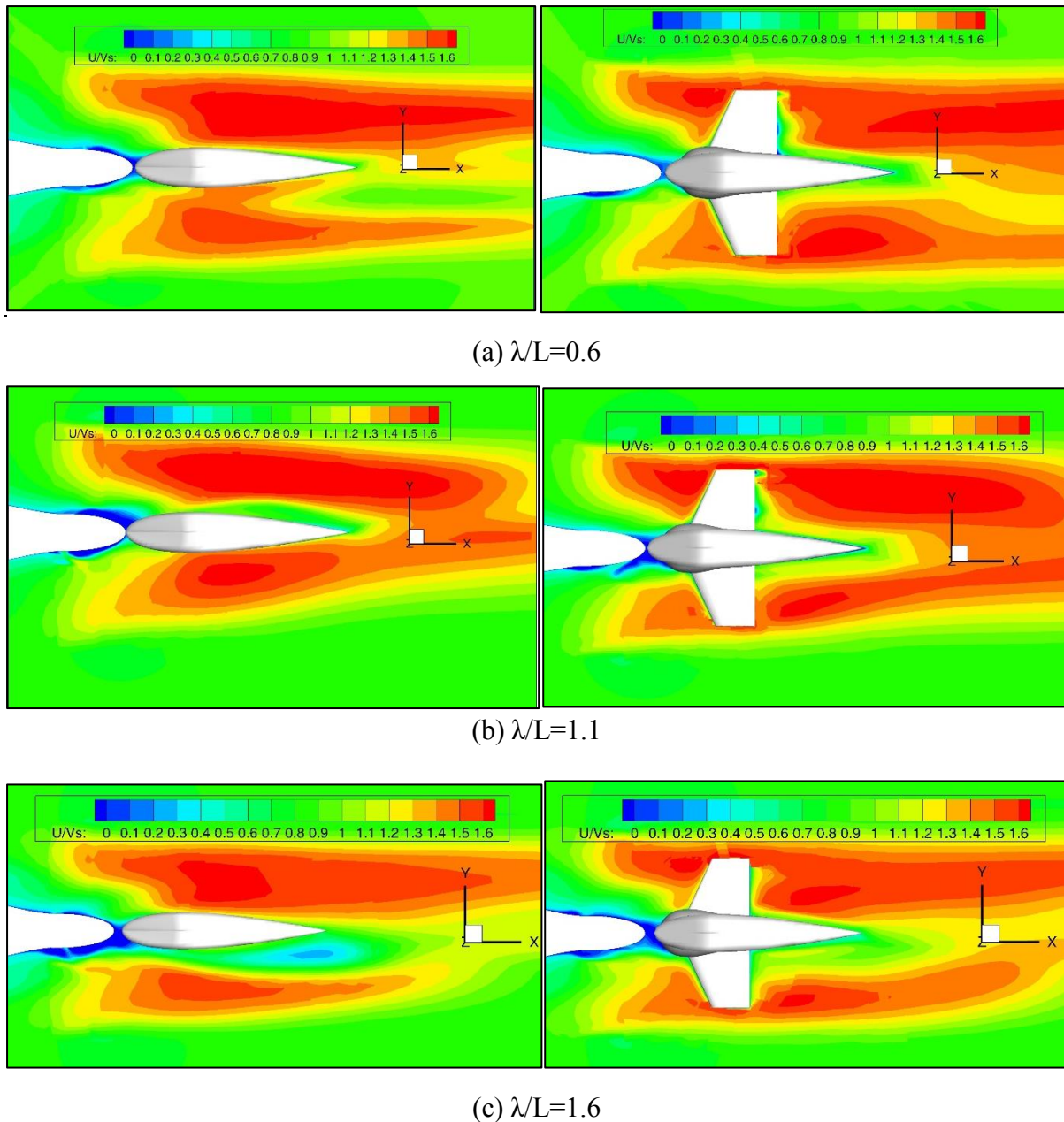


Fig 4-23 Comparison of flow field at horizontal plane

(Left: normal rudder and right: RBFS)

Fig 4-23 provides the comparison of wake field between the normal rudder and RBFS at the horizontal plane passing through the rudder bulb and fin in $\lambda/L=0.6, 1.1,$ and 1.6 . The flow field figures feature the axial velocity contour, U/V_s where U is the axial velocity component and V_s means ship's speed, 0.7967m/s . The left figure represents a normal rudder and the right picture shows the RBFS. The flow field in Fig 4-24 was computed at phase 0deg , which is the zero crossing up of wave at wave gauge in each wavelength.

The velocity field was larger on the starboard side than on the port side in both types of the rudder as a consequence of the clockwise rotation of a propeller. In RBFS, the axial

velocity was stronger downstream of the rudder due to the rudder fin in all wavelengths. The flow separation or reverse flow was detected in the port side of the normal rudder in $\lambda/L=1.6$. This separation was improved by the rudder bulb and fin, and thereupon, it seemed that the erosion due to two-phase flow and cavitation of the rudder might be prevented. There was a small-scaled flow separation at the trailing edge of the starboard side rudder fins, increasing the pressure drag. This fact was pointing that the rudder fin on the starboard side was needed to modify.

4.2.7 Visualization of vortex

The difference in flow velocity between the upper and lower surface of the propeller blade brings about a strong downward flow from the trailing edge of the blade. The downward flow of each blade accommodates a strong hub vortex. As a consequence of the hub vortex, the propulsion energy of the propeller declines to some extent. To know how the rudder bulb and fins take back the loss of the propulsion energy, the visualization of a vortex is one of the most interesting things. To understand the vortex structure, Q-Criterion is used. Q criterion is a method of vortex identification and measurement of a local balance between shear strain rate and vorticity magnitude. Q-Criterion is calculated according to the equation (43).

$$Q = \frac{1}{2} (\|\Omega_{ij}\|^2 - \|S_{ij}\|^2) \quad (43)$$

where the non-dimensional shear strain-rate is $S_{ij} = \frac{1}{2} (\frac{\partial U_i}{\partial x_j} + \frac{\partial U_j}{\partial x_i})$ and the vorticity tensor is $\Omega_{ij} = \frac{1}{2} (\frac{\partial U_i}{\partial x_j} - \frac{\partial U_j}{\partial x_i})$.

In this study, a Q value of 500 was used to visualize the vortex in three wavelengths ($\lambda/L=0.6, 1.1, \text{ and } 1.6$) at $t/Te=0$. In Fig 4-24, in the region where the designated Q value was matched, iso-surface was created and colored with axial velocity contour (u/U). The left figure shows RBFS and the right figure demonstrates the vortex in a conventional rudder.

Only the real propeller geometry can predict the tip vortex shedding. Nevertheless, the ring-shaped vortex system could be seen upstream of the rudder as a result of a body-force propeller model. There was no difference in the vortex system upstream of the rudder in all wave conditions. The propeller hub vortex could be visualized since the effect of the rotating hub was considered in a body force model. The hub vortex on the port side of both rudders was stronger than the starboard side's one owing to the clockwise rotation of the propeller. In addition, the rudder fin tip vortex was occurred in RBFS. In Fig 4-24, it was clearly observed

that the rudder fin on the starboard side eliminated overwhelmingly the strength of the hub vortex, which might lead to poor separation, excessive pressure drop, and erosion due to two-phase flow, and causing cavitation of downstream of a propeller. Therefore, RBFS may prevent those adverse consequence in the propulsion system and improve the propulsive performance.

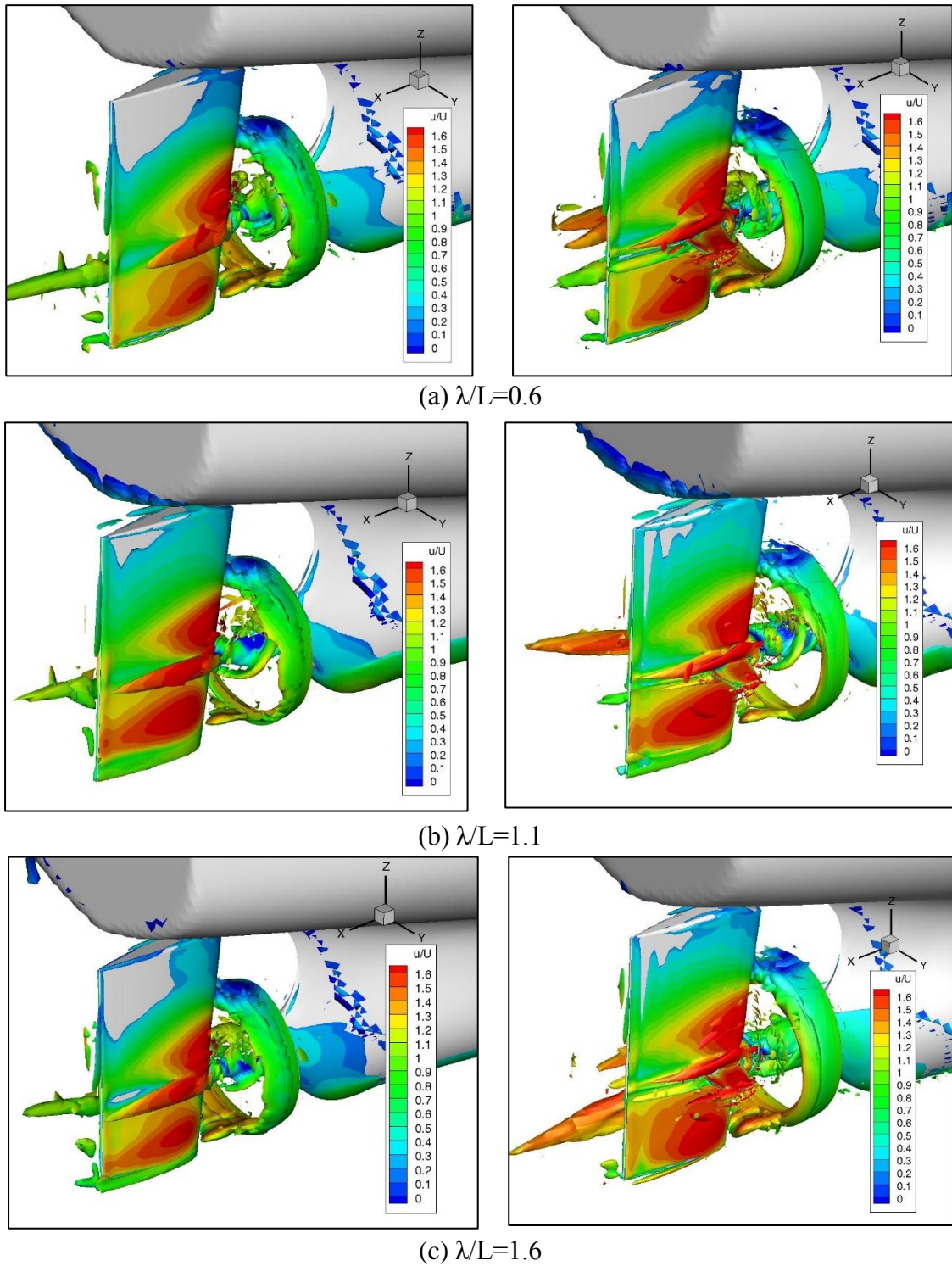


Fig 4-24 Illustration of Q-criterion for $Q=500$ colored by the axial velocity contours

(Left: normal rudder and right: RBFS)

4.3 Self-propulsion analysis

In fact, the propulsion system interacts with the ship hull and the flow field is generally changed by the hull and the propulsor. The propulsion system changes, in turn, the flow field behind a ship's hull. The hydrodynamic aspects of ship propulsion, that is, that part of ship propulsion which is affected by the flow of the water particles around the stern of the ship and through the propeller are discussed in this part of thesis. Hence, the propulsion analysis was performed to determine the power requirements and to supply wake and thrust deduction. Another purpose is to investigate the rate of energy recovery or the improvement of efficiency by RBFS, which is one of the most important concerns in this study.

The open water test of a propeller used in the present study at various revolution rates was carried out by Kishi (2018)⁴¹. This open water chart was presented in Fig 4-25. In the self-propulsion analysis, the propeller revolution rate of 16.3 rps, which is the model point of ship with RBFS in calm water was used. On the other hand, the propeller angular velocity of 16.5 rps, which is the model point of ship with normal rudder in calm water was applied in the experiment. Therefore, some differences between the results of CFD and EFD were expected. In addition, the resistance and thrust were unbalanced in wave as a result of using a model point in calm water. In general, it should use the model point in each and individual wave. Thus, an extra towing force had to be considered during the self-propulsion in waves.

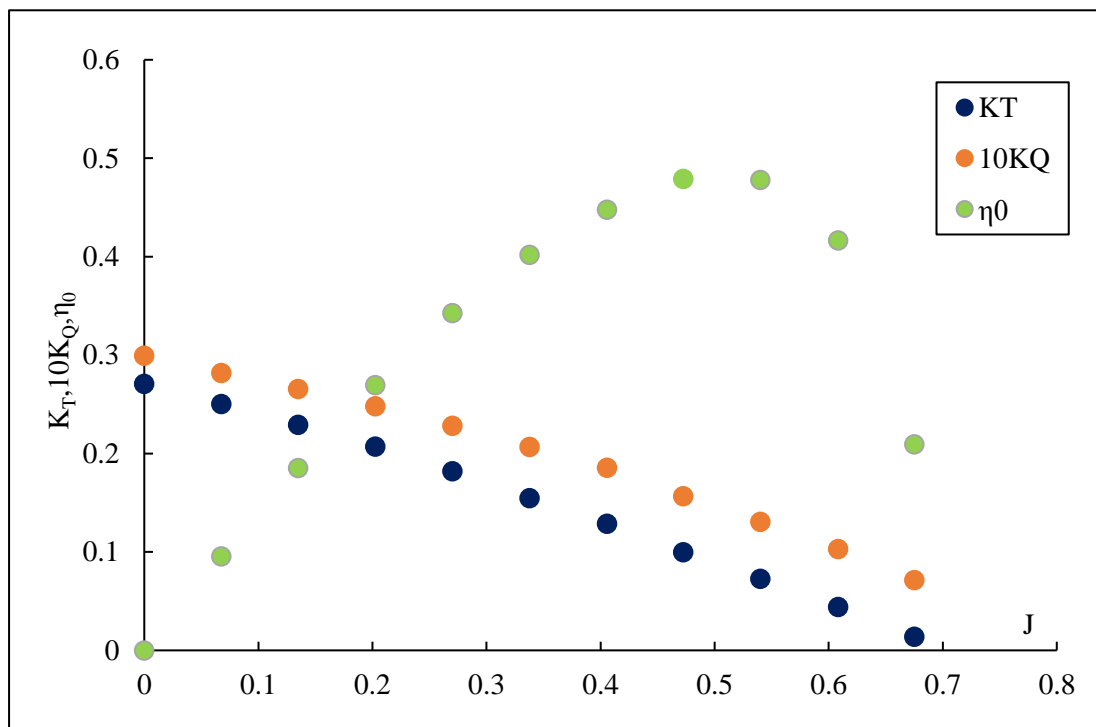


Fig 4-25 Open water graph of KVLCC2 propeller by Kishi (2018)

4.3.1 Effective wake

When a propeller is situated close to the hull in a position where the flow into the propeller is affected by the presence of the hull. The propeller inflow, i.e. the speed of advance of the propeller v_a , is generally slower than the ship speed, v_s due to the ship's wake. This wake is normally decomposed into three components; friction wake, potential wake and wave wake. The wake behind the hull without a propeller is called the nominal wake. On the other hand, the wake behind the vessel with an operating propeller is defined as the effective wake. In this dissertation, only the effective wake will be discussed.

In an evaluation of the self-propulsion, there are two approaches: "thrust identity" approach and "torque identity" approach. The thrust identity approach is about that the propulsor generates the same thrust in a wake field of wake fraction, w as in open-water test. The propeller produces identical torque in a wake field of wake fraction, w as in open-water test in the approach of torque identity⁴²). ITTC recommends the "thrust identity" approaches and thus, the thrust identity method was used to determine the effective wake coefficient in this research.

The thrust coefficient, K_T was obtained as an output from CFDSHIP-IOWA code, and then the advance number, J could be predicted on the propeller open water graph. The water inflow velocity into the propeller, v_a was calculated by the equation (46). The effective wake velocity, v_w is the deduction of the inflow velocity from the full ship's speed. The effective wake fraction proposed by Taylor is computed by equation (47). The time histories of effective wake of three cases (a hull without rudder, with normal rudder and with RBFS) in the converged region in three wavelengths ($\lambda/L=0.6, 1.1, \text{ and } 1.6$) over four encountered period are presented in Fig 4-26. For the ship with one propeller, the wake fraction coefficient, $1-w$ is generally in the range of 0.8 to 0.55. In this study, the average value of $1-w$ in all cases was over 0.5 which can also be checked in Table 4-3 and Table 4-4.

The effective wake was increased due to the rudder in all waves and in both CFD and EFD. It was increased more by rudder bulb and fins. It means that hull efficiency can be improved in accordance. Nevertheless, a large wake fraction might accidentally cause the risk of cavitation. That's why a cavitation investigation of the propeller and the rudder should be performed while using RBFS. Increasing the wavelength, the large fluctuation of the effective wake fraction's curve was occurred. The highest fluctuation rate was observed in $\lambda/L=1.6$. The CFD under-predicted with around 5% error the mean value of $1-w$ and computed a similar

trend compared to the experiment in each case. The error between CFD and EFD was a bit high (around 7%) in long wave condition.

$$K_T = aJ^2 + bJ + c \tag{44}$$

$$J = \frac{-b - \sqrt{b^2 - 4a(c - K_T)}}{2a} \tag{45}$$

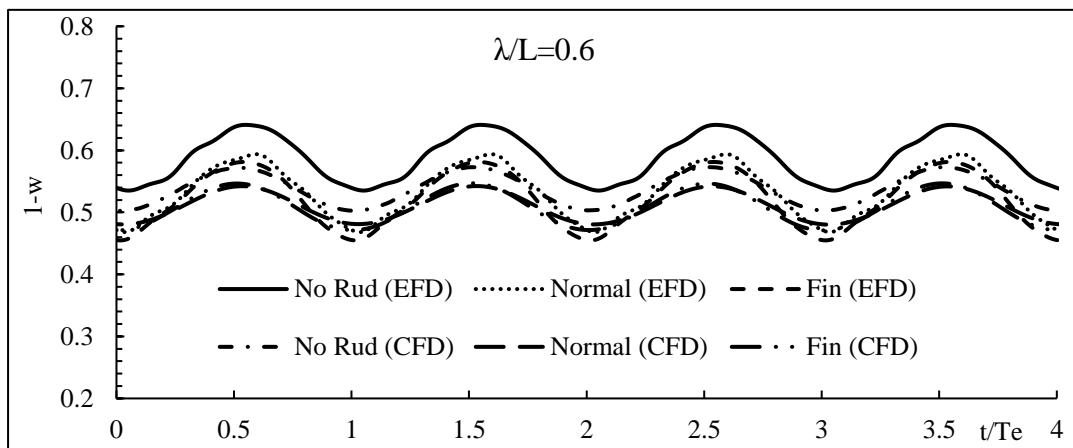
$$v_a = JnD \tag{46}$$

$$1 - w = \frac{v_a}{v_s} \tag{47}$$

Table 4-1 Propeller open water data

Diameter, D (m)	0.0986
n (rps) in CFD	16.3
a	-0.1458
b	-0.264
c	0.2715

(a , b , and c are constants of thrust coefficient curve, K_T in the propeller open water performance chart shown in Fig 4-26)



(a) $\lambda/L=0.6$

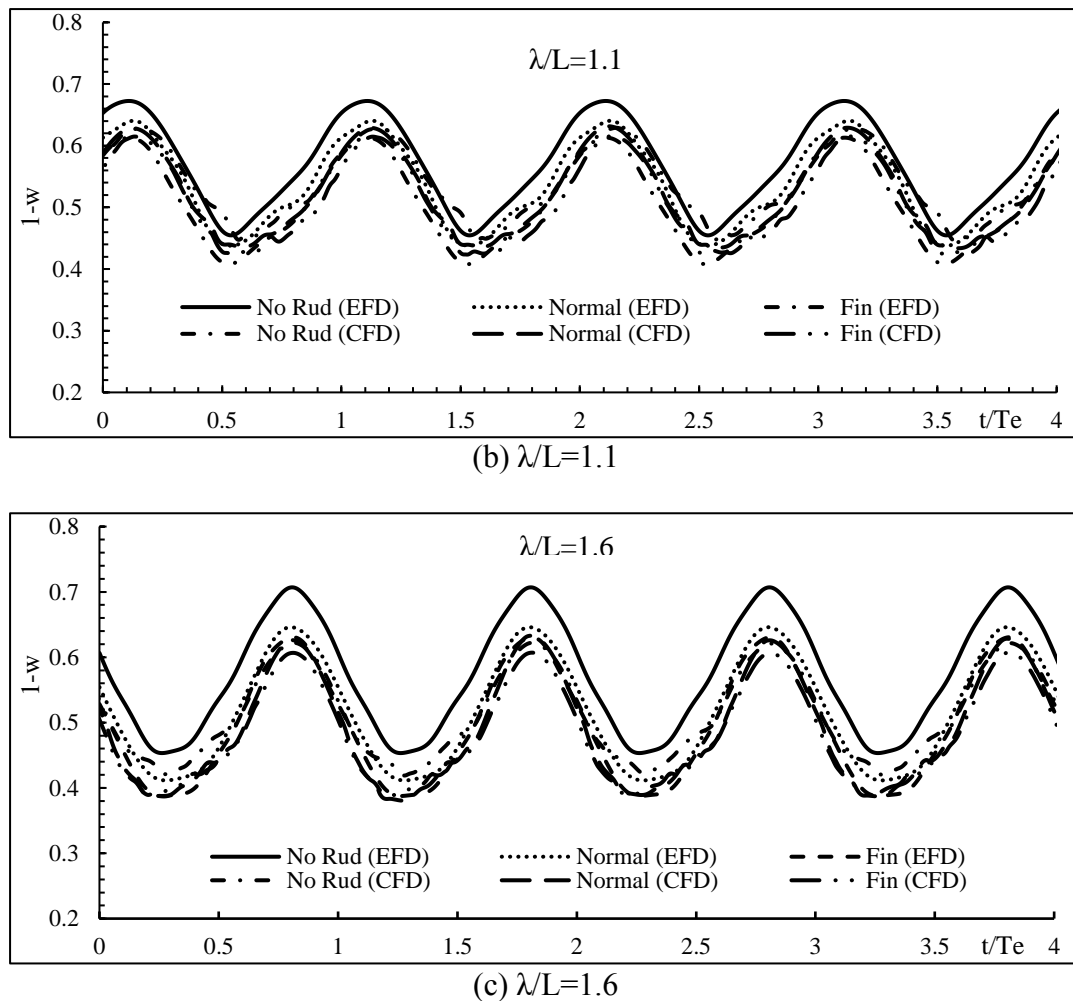


Fig 4-26 Comparison of time history of wake fraction

4.3.2 Thrust and resistance

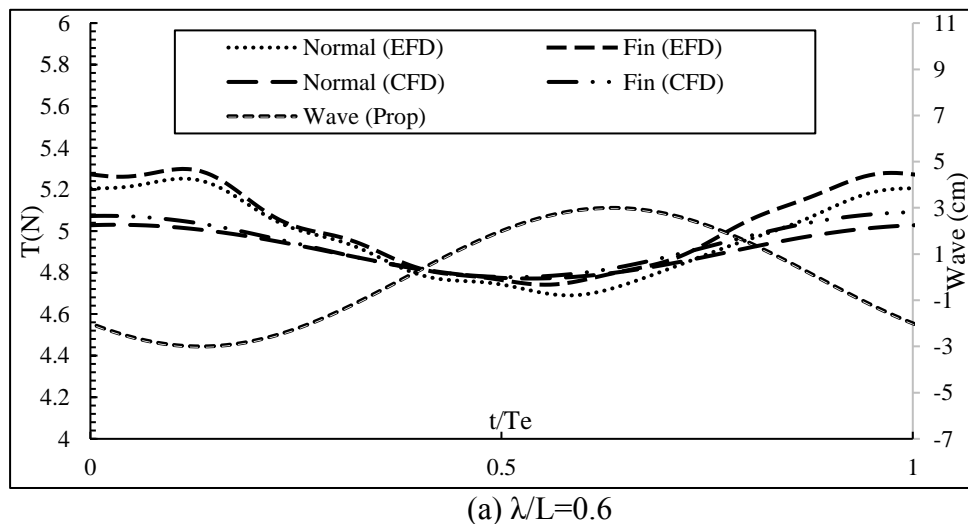
The efficient operating of a ship with low external force is one of the main concerns that ship-owners and naval architects are demanding. For that reason, the characteristic of thrust and resistance of a ship in waves and how much RBFS influences them were examined.

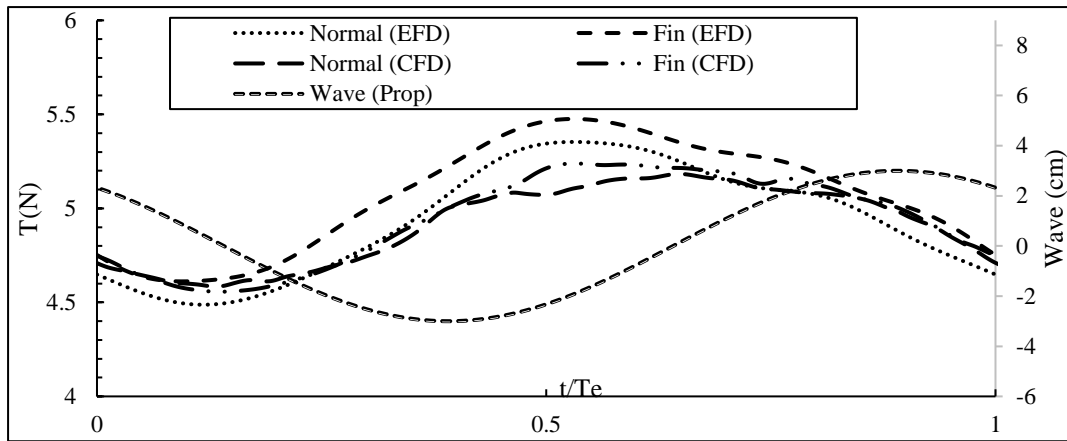
In CFD simulation, the prediction of propeller thrust was carried out by the body force propeller model based on blade element theory using the CFD output velocities components at the propeller plane without modelling of real propeller geometry. The overall thrust was computed by integrating the individual body force acting in axial direction contribution of each element on the propeller plane. CFD codes provide the thrust coefficient, K_T and the thrust in each case was calculated by equation (48). In experiment, the indicated thrust was measured through the propeller dynamometer fitted in the ship model between motor and propeller.

$$T = K_T \rho n^2 D^4 \quad (48)$$

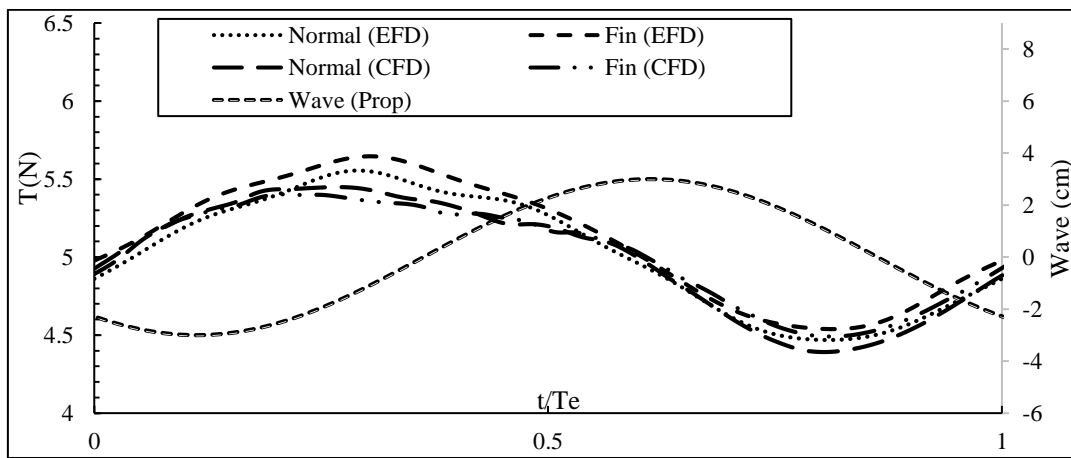
The comparison of time history of thrust between conventional rudder and RBFS in $\lambda/L=0.6, 1.1, \text{ and } 1.6$ over an encounter period were plotted in Fig 4-27. The significant difference of thrust time history between two types of rudder in both CFD and EFD was not occurred in all wave conditions. The curve of thrust oscillated in a simple harmonic and the amplitude increased with the increase of wavelength ratio. CFD predicted the similar trend and nature of the curve measured in experiment. The phase lags of thrust in all wavelengths were almost the same in both EFD and CFD.

Fig 4-28 and Fig 4-29 reveal the comparison of computed and measured mean thrust between a normal rudder and RBFS in five wavelengths ($\lambda/L=0.6, 0.85, 1.1, 1.35, \text{ and } 1.6$). In CFD simulation, the thrust was improved in all wave condition except $\lambda/L=1.35$. It was increased 0.53%, 0.59%, 0.57%, and 0.12% in $\lambda/L=0.6, 0.85, 1.1, \text{ and } 1.6$ respectively. However, it was decreased 0.06% in $\lambda/L=1.35$. In the experiment, the additional thrust was obtained in all wave lengths. The thrust improvement of 0.2%, 0.67%, 0.67%, 0.04%, and 0.74% was investigated in $\lambda/L=0.6, 0.85, 1.1, 1.35, \text{ and } 1.6$ respectively. CFD under-predicted with around 0.3% error the mean thrust of normal rudder in all waves as compared to the experimental results. It also under-predicted the thrust of RBFS in all waves except $\lambda/L=0.6$. The error of RBFS's thrust between CFD and EFD in $\lambda/L=0.6$ was around 0.03%. Overall, it can be proved that RBFS can generate the additional thrust in waves as in calm water.





(b) $\lambda/L = 1.1$



(c) $\lambda/L = 1.6$

Fig 4-27 Comparison of time history of thrust

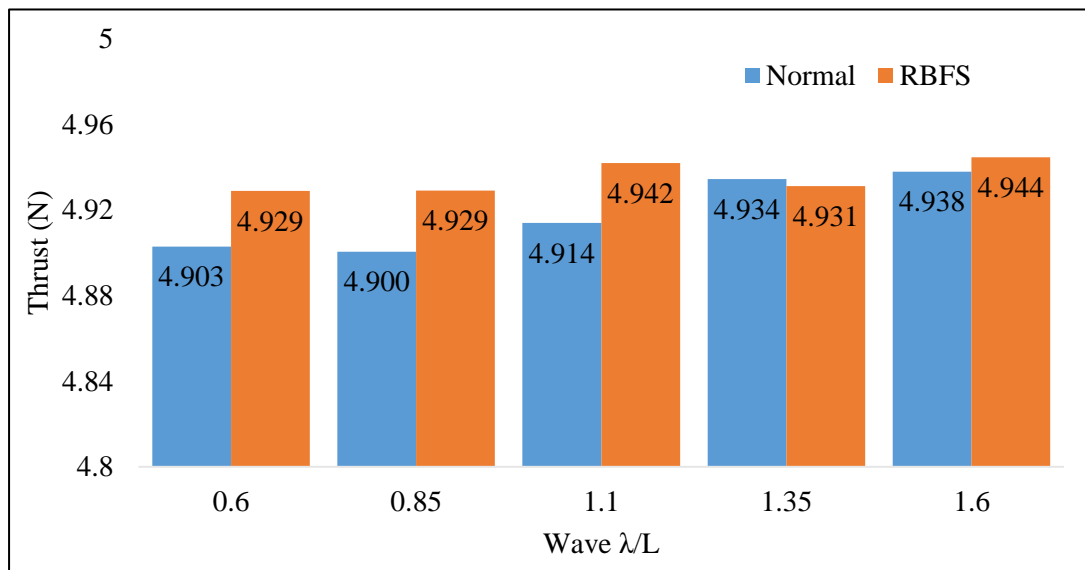


Fig 4-28 Comparison of mean thrust in CFD

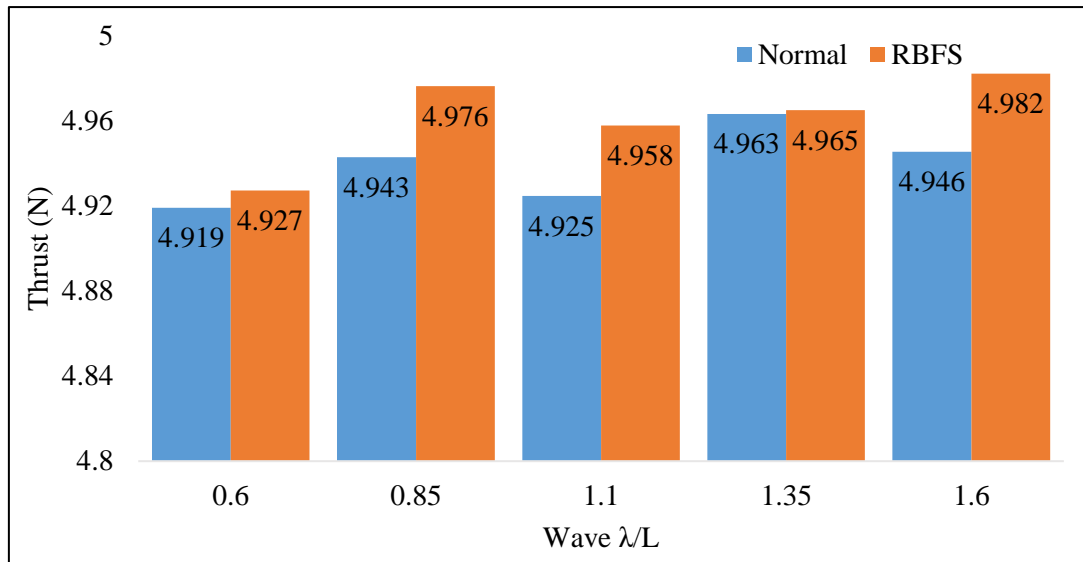


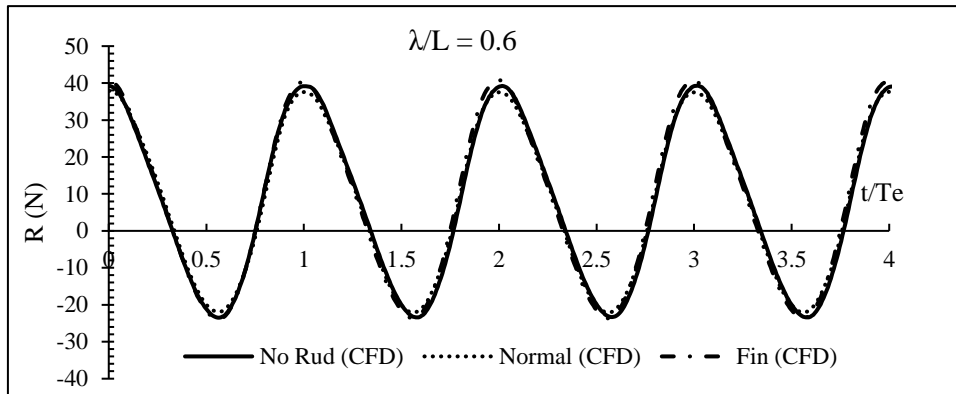
Fig 4-29 Comparison of mean thrust in EFD

In the CFD simulation, the total resistance coefficient, C_T was computed by the summation of each and single resistance coefficient output; frictional resistance coefficient, viscous pressure resistance coefficient, and wave resistance coefficient. Then the total resistance of the ship, R_T was computed by equation (49) where S refers to the area of the wetted surface. The convergence of the axial force time history curve was observed after 3000 iterations. The time history of axial force in that converged region was extracted over four periods and described in Fig 4-30. Only the resistance data by CFD computation was included as the experimental data of the time history of resistance was not available. The resistance data oscillated in a simple harmonic pattern at $\lambda/L = 0.6$ and 1.6 . But there was some non-linearity in the medium wave, in which the resonance generally occurs. In the time history graph of axial force, any changes between the normal rudder and RBF could not be investigated.

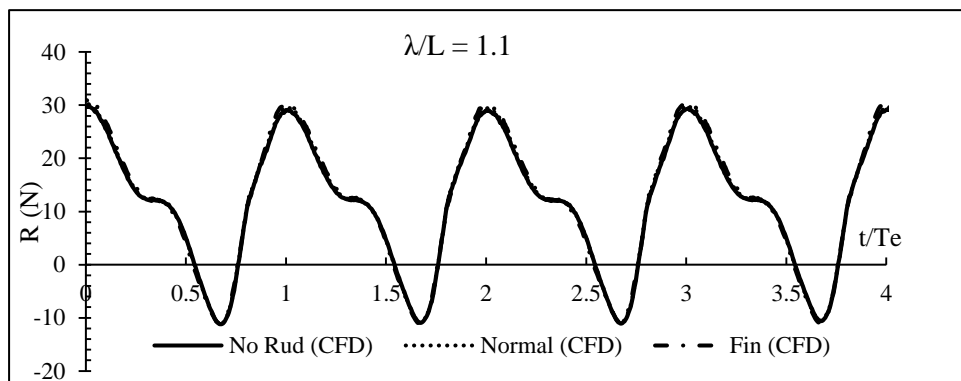
$$R_T = 0.5C_T\rho SV_S^2 \quad (49)$$

Fig 4-31 and Fig 4-32 give information about the comparison of computed and measured mean resistance between a normal rudder and RBFS in five wavelengths ($\lambda/L=0.6, 0.85, 1.1, 1.35,$ and 1.6). In CFD simulation, the resistance was dropped 0.9%, 1.1%, and 0.07% in $\lambda/L=0.6, 1.1,$ and 1.6 but it was risen 1.9% and 0.9% in $\lambda/L=0.85$ and 1.35 respectively. The mean value of resistance was exceed 1.0%, 0.7%, and 0.9% in $\lambda/L=0.85, 1.35,$ and 1.6 in the experiment. On the other hand, it was fallen 0.3% and 0.4% in $\lambda/L=0.6$ and 1.1 . In general, it is necessary to modify the RBFS for reducing drag since the resistance was increased a bit in most of the wavelengths. CFD over-predicted the axial force with around 0.5%, 2.6%, 6%, and

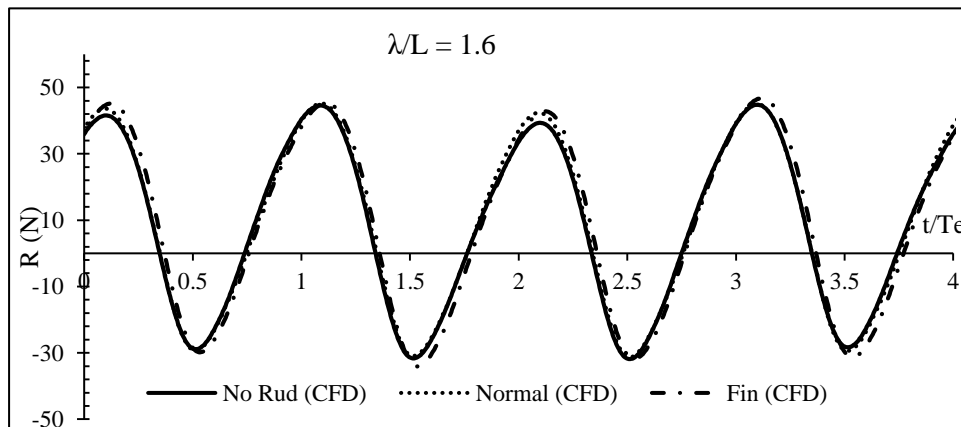
8% error in $\lambda/L=0.6, 0.85, 1.1,$ and 1.35 as compared to the experiment. However, the over-prediction of an axial force in $\lambda/L=1.6$ was fairly large and the estimated error was around 20%.



(a) $\lambda/L=0.6$



(b) $\lambda/L=1.1$



(c) $\lambda/L=1.6$

Fig 4-30 Comparison of computed axial force

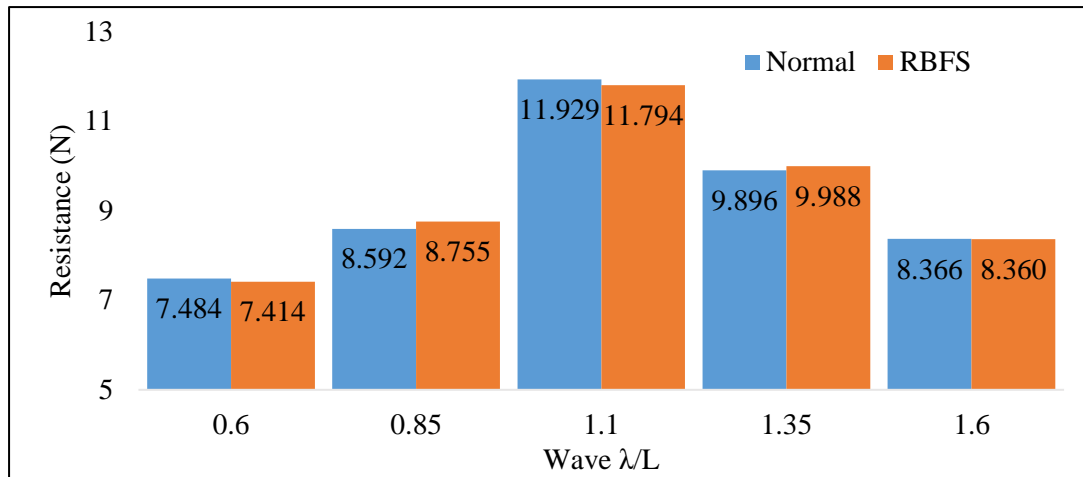


Fig 4-31 Comparison of mean value of resistance in CFD

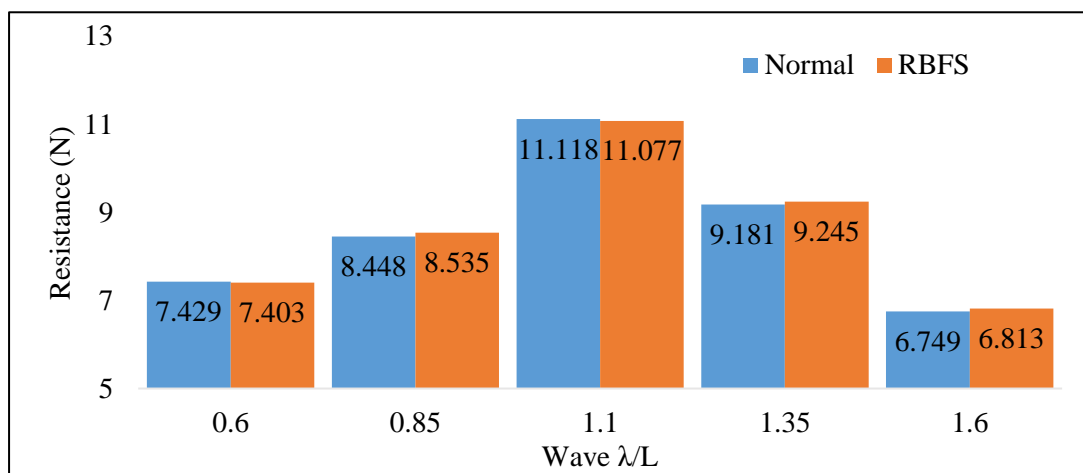


Fig 4-32 Comparison of mean value of resistance in EFD

4.3.3 Torque and delivered power

In the computational study, the prediction of propeller torque was performed by the body force propeller model based on blade element theory using the CFD output velocities components at the propeller plane without modelling real propeller geometry. The overall torque was computed by integrating the individual body force acting in angular direction contribution of each element on the propeller plane. CFDSHIP-Iowa code provides the torque coefficient, K_Q and the torque in each case, Q_D , was calculated by equation (50) in which the number of propeller revolutions is 16.3rps in CFD and 16.5rps in the experiment. In the experiment, the indicated torque was measured by means of the propeller dynamometer fitted in the ship model between the motor and propeller.

$$Q_D = K_Q \rho n^2 D^5 \quad (50)$$

The comparison of the mean value of computed and measured torque between a conventional rudder and the RBFS in five wave conditions ($\lambda/L=0.6, 0.85, 1.1, 1.35, \text{ and } 1.6$)

is given in Fig 4-33. The very small difference between two rudders was observed at all waves in CFD computation. Contradictorily, RBFS required more torque than a normal rudder in EFD. In fact, the torque should be lower in ESDs than a hull without ESDs. In CFD, the torque was declined approximately 0.2%, 0.04%, 0.04%, and 0.8% in $\lambda/L=0.6, 0.85, 1.1,$ and 1.6 . However, it was multiplied roughly 0.3% in $\lambda/L=1.35$. In the measurement of torque, it was increased just about 5.6%, 7.3%, 0.2%, 2.5%, and 5.2% in $\lambda/L=0.6, 0.85, 1.1, 1.35$ and 1.6 respectively. CFD under-predicted the torque with an average error of 14% as opposed to the experimentally measured data.

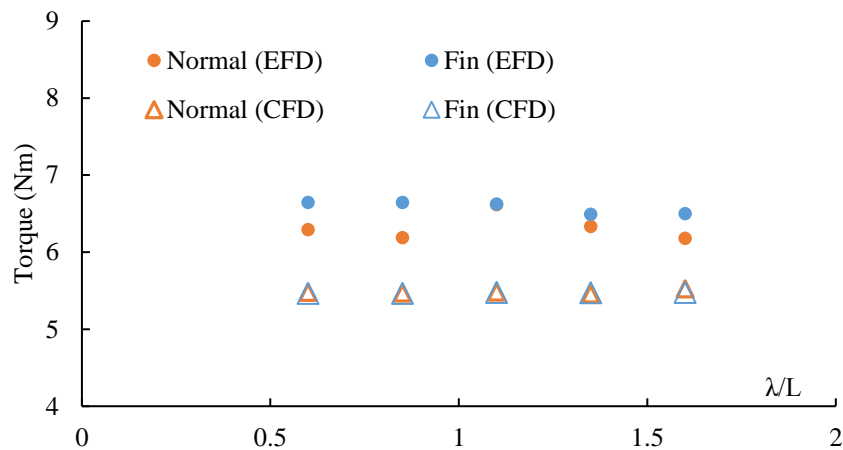


Fig 4-33 Comparison of torque

The prediction of the power required to propel a ship is one of the important considerations for a ship designer. The transmission of the power produced in the engine to the useful power output of the propeller cannot be fulfilled without some energy losses. Therefore, there are many types of power related to ship propulsion for example; effective power, thrust power and delivered power. In this dissertation, only delivered power will be discussed. It is the power delivered to the propeller, in which there are losses due to gearbox, bearings, stern tube seals and so on. The delivered power, P_D was computed by the equation (51).

$$P_D = 2\pi n Q_D \quad (51)$$

Table 4-2 shows the comparison of delivered horse power between a normal rudder and RBFS in EFD and CFD. In the experiment, similar to the torque, the delivered power required to rotate the propeller was much higher in RBFS than in a normal rudder. In contrast, a ship with RBFS required less power than a hull with a normal rudder in CFD simulation, although the difference was quite small. In the computation, a ship with RBFS necessitated less power 0.2%, 0.04%, 0.04%, and 0.8% in $\lambda/L=0.6, 0.85, 1.1,$ and 1.6 . Nonetheless, it needed roughly more power 5.6%, 7.3%, 0.2%, 2.5%, and 5.2% in $\lambda/L=0.6, 0.85, 1.1, 1.35$ and 1.6 in the

measurement. CFD under-predicted the trend of delivered power with an average error of 15% as compared to EFD data in each wavelength.

Table 4-2 Comparison of delivered power

	λ/L	0.6	0.85	1.1	1.35	1.6
EFD	Normal	6.2929	6.1893	6.6143	6.3344	6.1789
	RBFS	6.6454	6.6454	6.6247	6.4899	6.5003
CFD	Normal	5.4772	5.4665	5.4792	5.4557	5.5231
	RBFS	5.4627	5.4642	5.4767	5.4725	5.4762

4.3.4 Efficiencies

To assess the performance of energy saving device, estimation of efficiency is very important. In the present study, mechanical efficiencies were not taken into account and only propulsive efficiencies such as hull efficiency, open water efficiency, relative rotative efficiency and quasi-propulsive efficiency were computed. A measure of how effectively the shape of ship hull foam without ESD or with ESD designed to suit the propulsion arrangement is generally defined as the hull efficiency. It is a ratio of thrust deduction factor and effective wake. In other words, it is a ratio of effective power and thrust power as shown in equation (52). The thrust deduction fraction, $1-t$, was computed according to equation (51), in which R_T represents the total resistance of a ship with a propeller and R_0 means the towing resistance of a vessel without a propeller.

$$1-t = 1 - \left[\frac{R_T - R_0}{T} \right] \quad (51)$$

$$\eta_H = \frac{P_E}{P_T} = \frac{R_T v_s}{T v_a} = \frac{1-t}{1-w} \quad (52)$$

Table 4-3 and Table 4-4 provide information about the comparison of resistance, thrust, and hull efficiency between a conventional rudder and RBFS in CFD and EFD. To be able to see clearly the difference of hull efficiency, the comparison in the bar chart was illustrated in Fig 4-34 and Fig 4-35. In the numerical simulation, hull efficiency was improved by about 0.3% and 3.7% only at two wavelengths ($\lambda/L=0.6$ and 1.1) due to the RBFS. It was deteriorated with 0.3%, 1.0%, and 0.2% reduction in $\lambda/L=0.85$, 1.35, and 1.6. In the experiment, 0.7%, 2.7%,

and 0.1% improvement of hull efficiency was observed in $\lambda/L=0.6, 1.1,$ and 1.6 . However, the propulsion system was worse slightly with 0.6% and 1.5% decrease of hull efficiency in $\lambda/L=0.85$ and 1.35 . In calm water, hull efficiency exceeded 3.6% and 7.3% in CFD and EFD respectively²⁶). Therefore, it can be stated that RBFS in wave conditions is not as efficient as in calm water. The estimation of CFD followed a similar trend to the EFD measurement. CFD over-predicted the hull efficiency of both rudder cases in all wavelengths with an average error of 3.0% in the comparison with EFD. Thus, CFD had a good agreement with experiment.

Table 4-3 Self-propulsion factors computed by CFD

λ/L	Rudder Types	Resistance (N)	Thrust (N)	1-t	1-w	η_H
0.6	Normal	7.4840	4.9028	0.7993	0.5109	1.5643
	RBFS	7.4143	4.9288	0.7920	0.5046	1.5697
0.85	Normal	8.5917	4.9004	0.8178	0.5114	1.5989
	RBFS	8.7550	4.9289	0.8042	0.5047	1.5936
1.1	Normal	11.9292	4.9138	0.8174	0.5157	1.5849
	RBFS	11.7944	4.9418	0.8190	0.4984	1.6433
1.35	Normal	9.8960	4.9344	0.8050	0.5023	1.6026
	RBFS	9.9882	4.9310	0.7981	0.5029	1.5868
1.6	Normal	8.3659	4.9378	0.7969	0.4926	1.6177
	RBFS	8.3603	4.9445	0.8076	0.5003	1.6142

Table 4-4 Self-propulsion factors measured by EFD

λ/L	Rudder Types	Resistance (N)	Thrust (N)	1-t	1-w	η_H
0.6	Normal	7.4287	4.9191	0.8331	0.5419	1.5374
	RBFS	7.4032	4.9273	0.8386	0.5416	1.5483
0.85	Normal	8.4483	4.9429	0.8147	0.5375	1.5157
	RBFS	8.5351	4.9764	0.7985	0.5301	1.5062
1.1	Normal	11.1180	4.9247	0.8285	0.5423	1.5277
	RBFS	11.0768	4.9579	0.8379	0.5343	1.5682
1.35	Normal	9.1808	4.9633	0.827	0.5327	1.5524
	RBFS	9.2451	4.9651	0.8141	0.5325	1.5287
1.6	Normal	6.7486	4.9455	0.8362	0.5368	1.5576
	RBFS	6.8132	4.9822	0.8244	0.5287	1.5594

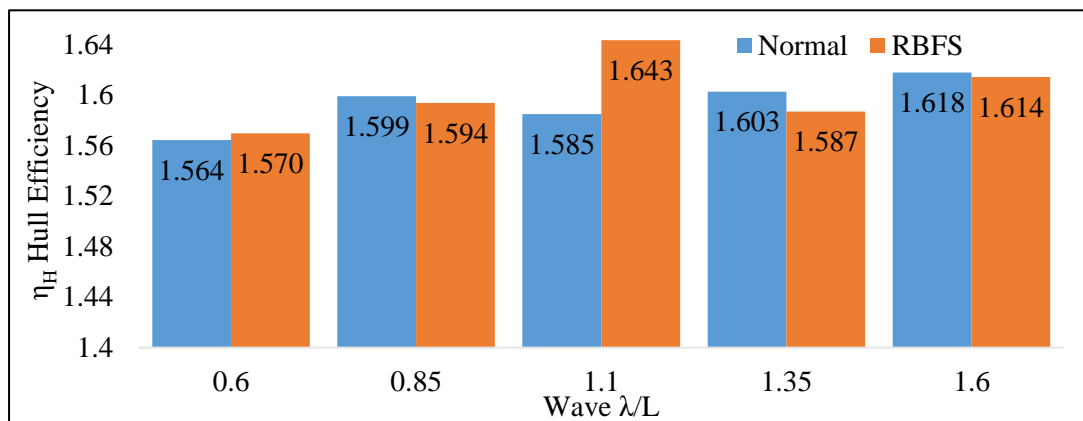


Fig 4-34 Comparison of computed hull efficiency

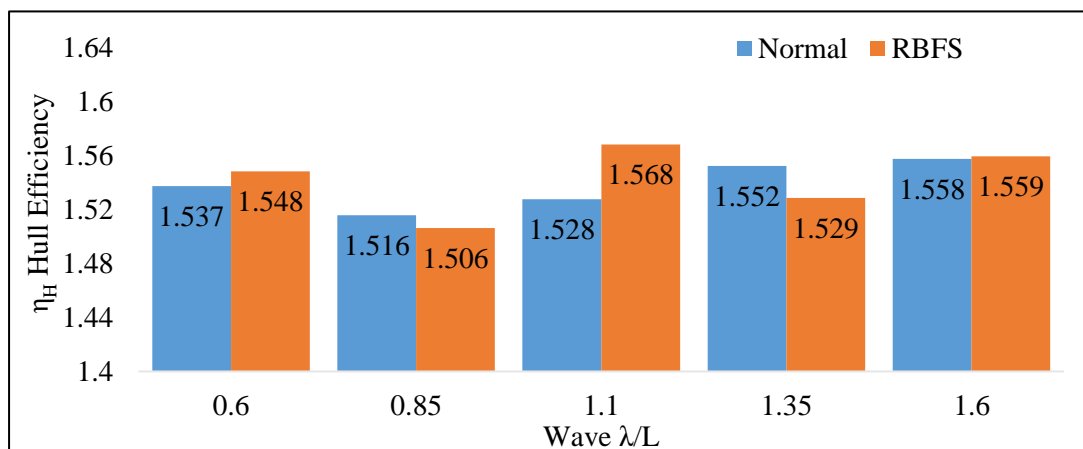


Fig 4-35 Comparison of measured hull efficiency

Comparison of open water efficiency, relative rotative efficiency, and quasi-propulsive efficiency was performed and that results were presented in Table 4-6. Equations (54) and (55) show how to compute the open water efficiency, η_0 and relative rotative efficiency, η_R . The quasi-propulsive efficiency, η_D is the product of three efficiencies as shown in equation (56).

$$K_{Q0} = aJ^2 + bJ + c \quad (53)$$

$$\eta_0 = \frac{Tv_a}{2\pi nQ_0} = \frac{K_T J}{2\pi K_{Q0}} \quad (54)$$

$$\eta_R = \frac{Q_0}{Q_D} = \frac{K_{Q0}}{K_Q} \quad (55)$$

$$\eta_D = \frac{P_E}{P_D} = \eta_H \eta_0 \eta_R \quad (56)$$

Table 4-5 Propeller open water data

Diameter, D (m)	0.0986
n (rps) in CFD	16.3
a	-0.01611
b	-0.02085
c	0.03135

(a , b , and c are constants of torque coefficient curve, K_Q in the propeller open water performance chart shown in Fig 4-25)

The propeller open water efficiency, η_0 , is an assessment of the propeller performance in a homogeneous wake field without hull in front of it. It mainly depends on the speed of advance, v_a , thrust force, T , rate of revolution, n , and so on. In the comparison of open water efficiency between a hull with a normal rudder and RBFS, it was decreased to some amount due to RBFS in all wavelengths. One of the reasons might be the increase of the wake fraction. The 1.0%, 3.0%, and 0.3% reduction of open water efficiency in $\lambda/L=0.6$, 1.1, and 1.6 was investigated.

The relative rotative efficiency, η_r , is a ratio of the efficiency of propulsor operating behind a ship to its open-water efficiency. The open water velocity field is generally uniform but the flow pattern behind a ship is non-uniform. Due to this difference, the two efficiencies will not necessarily be the same as each other. However, its ratio is very close to unity since the

difference is quite small. When the comparison of this efficiency was carried out, RBFS could improve it by approximately 0.6%, 0.9%, and 0.5% in $\lambda/L=0.6$, 1.1, and 1.6 respectively. Thus, it can be said that the flow in the case of RBFS was smoother as compared to the ship with a conventional rudder.

The quasi-propulsive efficiency, η_D , was increased by roughly 1.5% in medium wavelength, $\lambda/L=1.1$. Nonetheless, it dropped slightly with the estimated reduction of 0.14% and 0.02% in $\lambda/L=0.6$ and 1.6. This amount of lowering is considered very small. It can make a remark that RBFS does not have an adverse effect on the propulsion system in wave conditions from the aspect of its efficiency.

Table 4-6 Comparison of propulsive efficiencies

	$\lambda/L = 0.6$		$\lambda/L = 1.1$		$\lambda/L = 1.6$	
Efficiencies	Normal	RBFS	Normal	RBFS	Normal	RBFS
η_H	1.5643	1.5697	1.5849	1.6433	1.6177	1.6142
η_0	0.2770	0.2741	0.2797	0.2713	0.2730	0.2723
η_R	1.1909	1.1979	1.1871	1.1981	1.1915	1.1972
η_D	0.5160	0.5153	0.5262	0.5341	0.5263	0.5262

Chapter -5- Various Fin's Configurations

5.1 Motivation

The current chapter is a continuation of the research on the modification of fin's geometry in the calm water done by Troung³⁰). That research was about finding the best configuration of the fin's shape based on the wake field in calm water and the investigation of the performance of new the rudder-fin design in calm water. These new fins were designed by shortening the span, modifying the root camber line and changing AOA. The present chapter features the performance of these newly designed rudder fins in various regular head waves to develop effective energy-saving devices in waves.

The improvement of the flow field, thrust, and hull efficiency of a ship with these new fin's geometries was higher than that with the original fin's geometry in calm water³⁰). In reality, ships are being driven in the actual sea state with wind, waves, and adverse weather conditions. Therefore, it is absolutely necessary the performance testing in different wave conditions before practical use. The aim of current study is to contribute or to give awareness about this issue to the shipbuilding industry by confirming systematically whether the performance of those newly designed fins is still improving in regular head waves or not. In the investigation of the performance, not only the self-propulsion analysis but also the motion and wake field analysis was executed in three wavelengths ($\lambda/L=0.6, 1.1, \text{ and } 1.6$) to comprehend the detailed performance of RBFS with the aid of CFDShip-Iowa code. The validation of self-propulsion factors computed in the numerical simulation was carried out with the available experimental results.

5.2 Physical geometry

The same model of KRISO Very Large Crude Carrier (KVLCC2) with a scale ratio of 1:100 and propeller applied in the previous research were used to investigate the performance of the new fin's configuration. The rudder profile of KVLCC2 presented at the Workshop on Verification and Validation of Ship Manoeuvring Simulation Methods (SIMMAN 2008) was applied in the present study.

The modification of the rudder fins was performed providing that the self-propulsion model test of a ship with the original RBF system in calm water was accomplished by Troung. Three geometric parameters of the rudder fin were considered to reform the rudder fins. These are the span of fin, angle of attack (AOA) and camber line of the fin. Shortening the span of the fin can reduce the wetted surface area, resulting in a decrease in frictional resistance.

Various Fin's Configurations

Besides this, the flow direction near the tip of the starboard-side fin was opposite to that of the root of a fin in the original RBFS and thus, shortening the span length would be better to improve the lift-drag ratio. The lift force which can transform into an additional thrust can be adjusted by AOA and camber profile. Accordingly, it was decided to change the above parameters of rudder fins.

Truong (2019) executed the performance of many types of fin's configuration in the still water. In this dissertation, the investigation of only three newly designed fins in waves are proposed. For the ease of identification, these newly designed fins are named as cut0.005-fin, cut0.007-fin and NACA-fin respectively. The cut0.005-fin, and cut0.007-fin are the RBF in which the starboard side fin was cut at the section of $y/L = 0.005$ and 0.007 respectively, and rotated 6-degree upward as shown in Fig 5-1 and Fig 5-2. The NACA-fin is the RBF where the root camber profile of both side fins was reformed into NACA5412, tip camber profile was kept the same as the original one, and 6-degree AOA was applied on both sides as demonstrated in Fig 5-3.

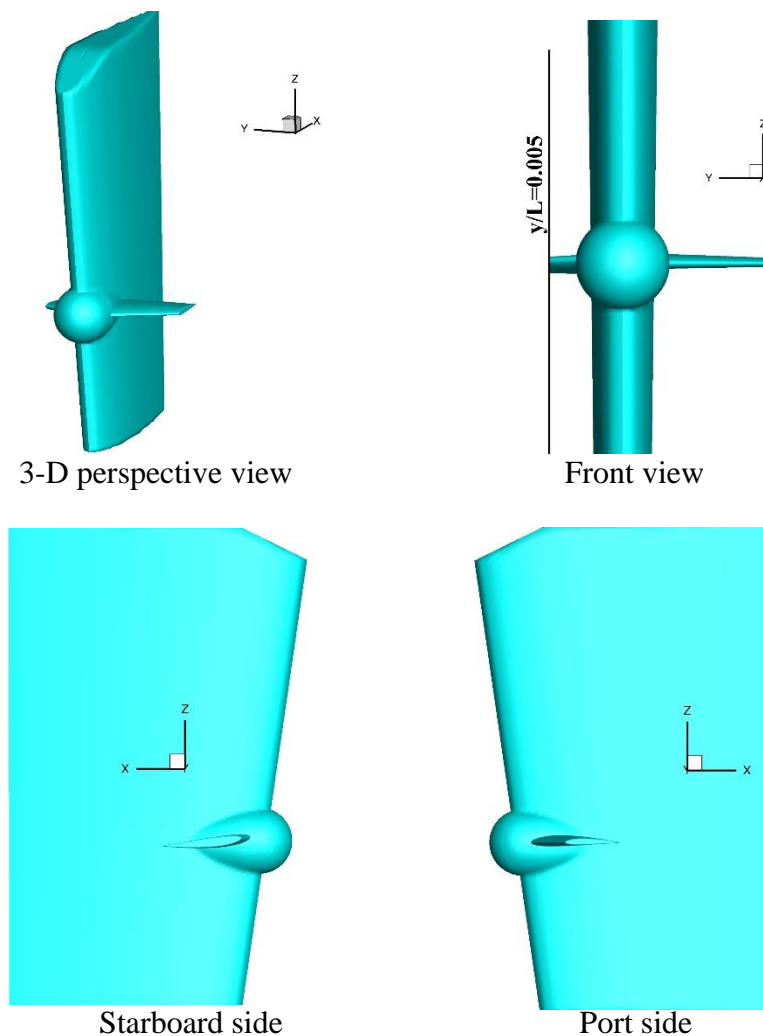


Fig 5-1 Cut0.005-fin

Various Fin's Configurations

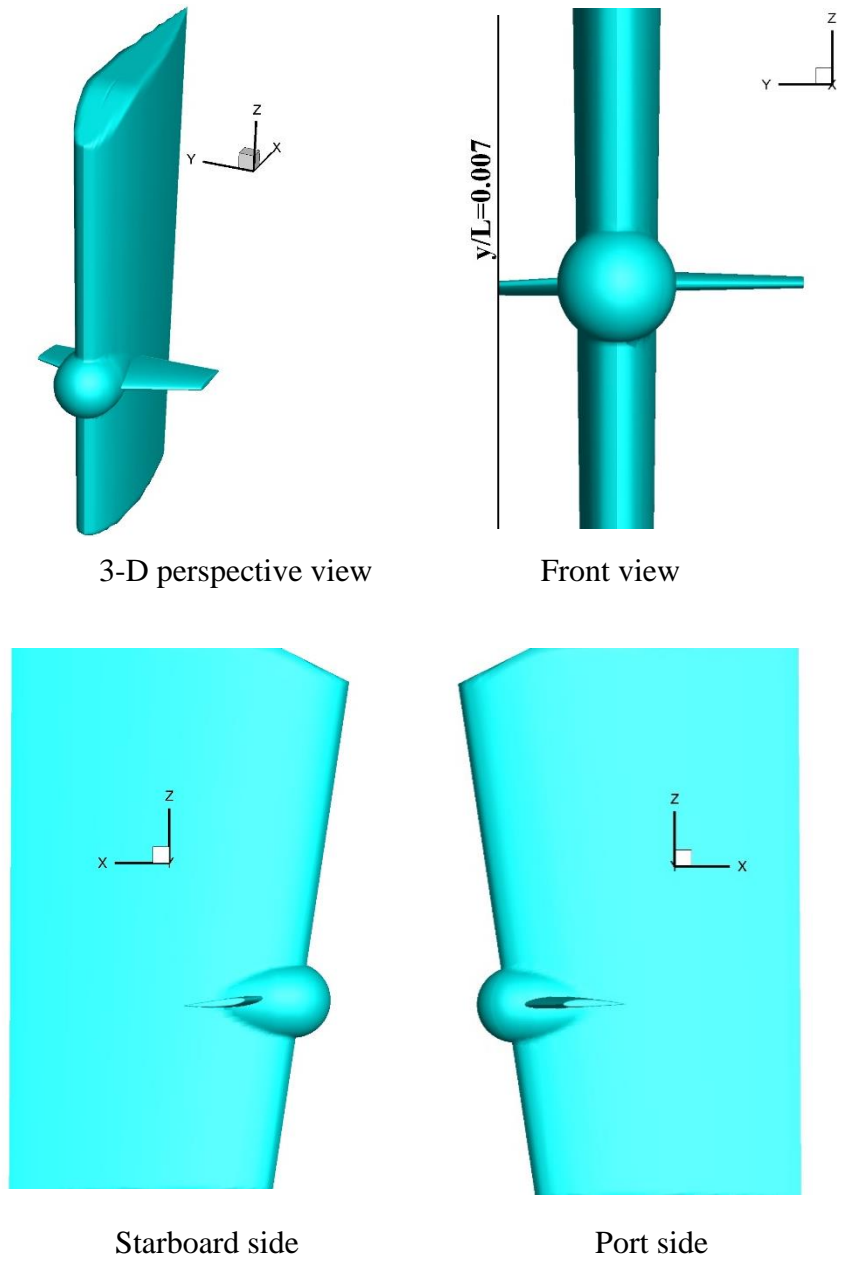


Fig 5-2 Cut0.007-fin

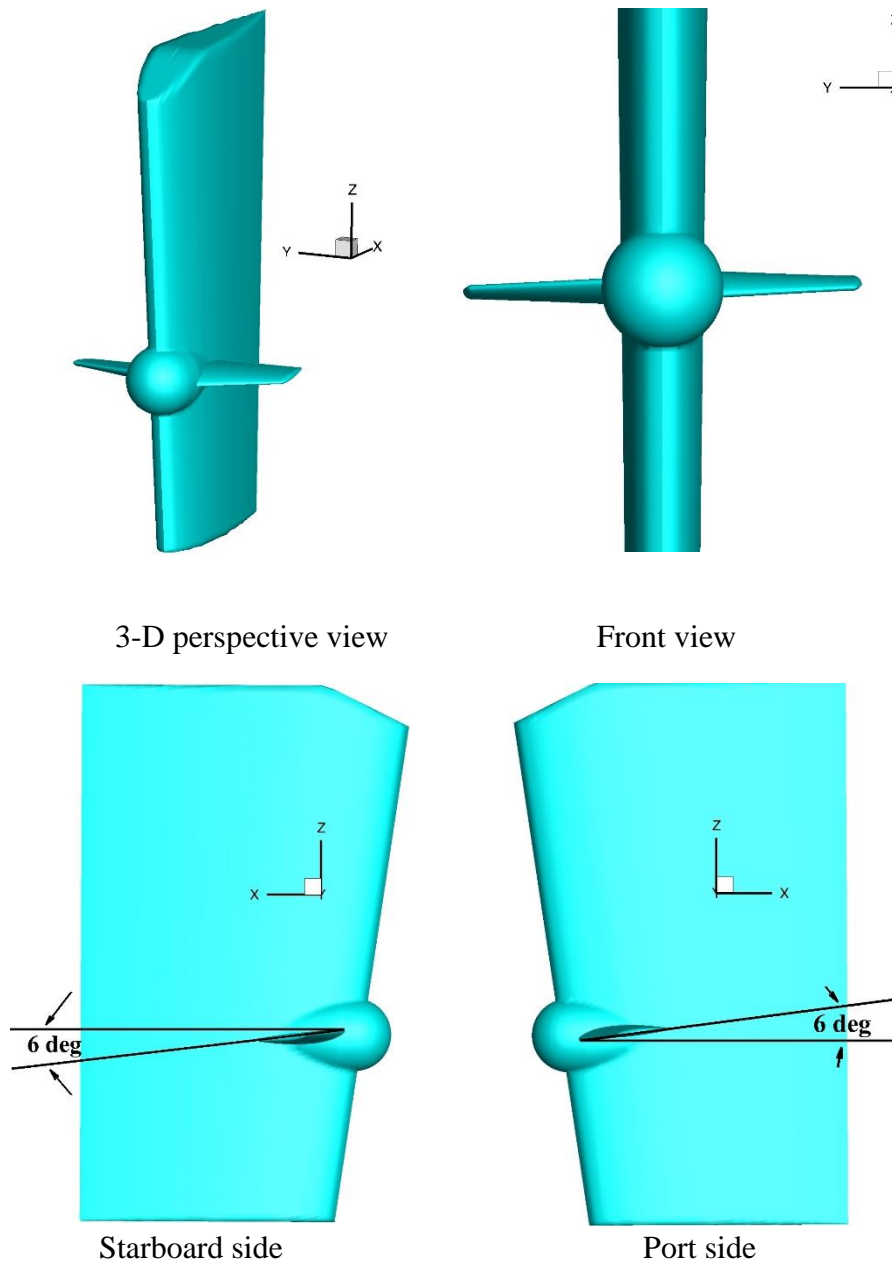


Fig 5-3 NACA-fin

5.3 Test conditions

A moderate range of wavelengths ($\lambda/L = 0.6, 1.1, \text{ and } 1.6$) was covered in computational analysis. In each type of wavelength, the wave amplitude is 3cm. There are totally 18 simulations in two conditions; namely as towing (without propeller) and self-propulsion (with propeller) for three cases; a ship with cut0.005-fin, ship with cut0.007-fin, and ship with NACA-fin. The summary of all the simulated conditions was provided in table 5-1. The objective ship model was run at a designated speed of 0.795 m/s which is relevant to Froude number of 0.142, and Reynold number of 2.564×10^6 . The simulations considered two degree of freedom motions (heave and pitch). The propeller revolution rate of 16.3 rps was

used in the self-propulsion analysis. The numerical simulations are carried out in the same grid system, computational domain and boundary conditions, and computational conditions as the previous research.

Table 5-1 CFD simulation matrix

Wave conditions	Types of rudder	Test conditions (propeller)
$\lambda/L=0.6, A=3\text{cm}$	Cut0.005-fin	w/o
		w/
	Cut0.007-fin	w/o
		w/
	NACA-fin	w/o
		w/
$\lambda/L=1.1, A=3\text{cm}$	Cut0.005-fin	w/o
		w/
	Cut0.007-fin	w/o
		w/
	NACA-fin	w/o
		w/
$\lambda/L=1.6, A=3\text{cm}$	Cut0.005-fin	w/o
		w/
	Cut0.007-fin	w/o
		w/
	NACA-fin	w/o
		w/

(w/o = without propeller and w/ = with propeller)

5.4 Results and discussions

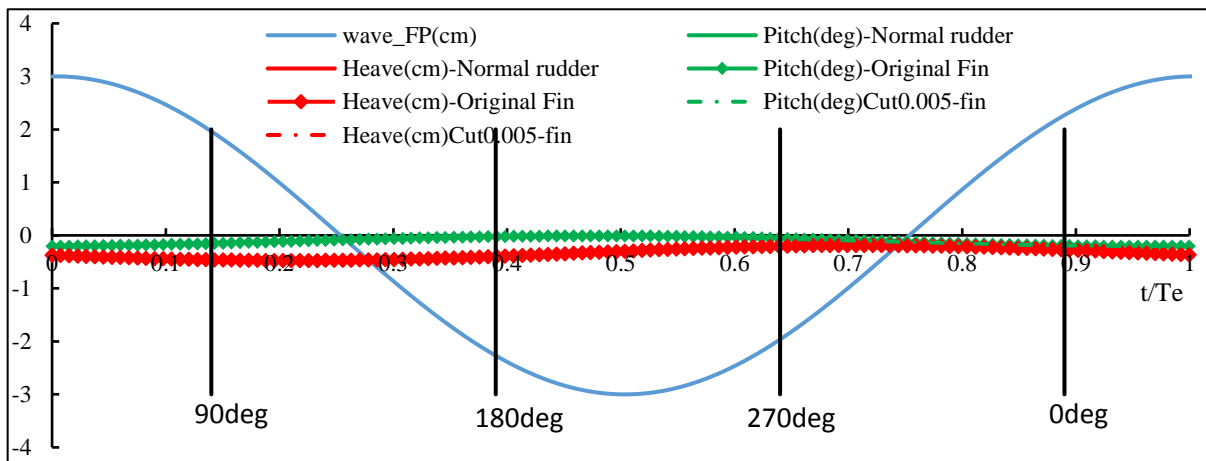
5.4.1 Motion responses

In this study, only two oscillatory motions, namely heave and pitch motions were predicted. In CFDShip-Iowa, the 6DOF equations of motion of a ship are described by translations concerning the static location of the center of gravity on the earth system, and by the rotations in terms of the Euler angle.

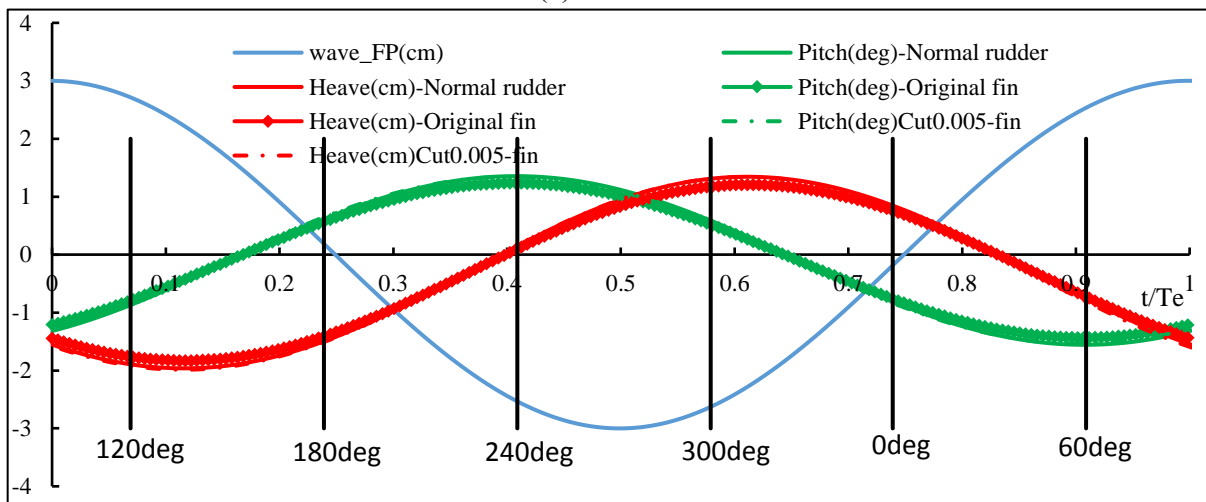
Fig 5-4 presents the computed results of heave and pitch motions of KVLCC2 with normal rudder, rudder with an original fin, and rudder with cut0.005-fin for three-wave conditions over one encounter period. The data of wave at a forward perpendicular (FP) was also added in the graph with a blue-colored line. Fig 5-4 also provide a phase relationship between the wave, pitch, and heave motions with heave following pitch harmonically. The

period of the motions was the same as the wave period. The amplitude of heave motions can be defined as the difference in the displacement of the ship from the equilibrium position to its lower or upper extreme position. The heaving force and pitching moment are small when the effective wavelength is less than half of the ship's length. Consequently, the heave and pitch motions were small in the short wave, $\lambda/L=0.6$, and are large in $\lambda/L= 1.1$ and 1.6 .

In the comparison of heave and pitch motions of cut0.005fin with original fin and normal rudder cases, no significant difference was found in all wave conditions. Hence, the lines representing all types of rudder coincided with each other. The mean values of heave and pitch motions of all cases were obtained at nearly the same value of 0.3cm and 0.1degree respectively. It can be reported that any kind of fins does not have a significant influence on the vessel's motion responses since its size is quite small as compared to the size of a ship.

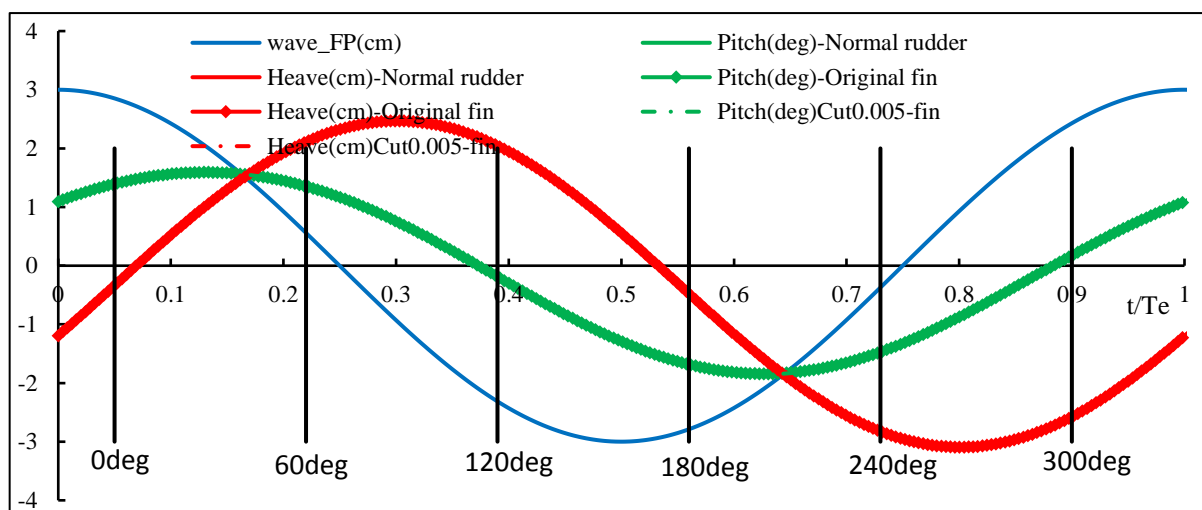


(a) $\lambda/L=0.6$



(b) $\lambda/L=1.1$

Fig 5-4 Comparison of heave and pitch motions



(c) $\lambda/L=1.6$

Fig 5-4 (continued)

5.4.2 Wake Fields

5.4.2.1 Flow fields at $x/L=1.0$

Some of the basic working principles of RBFS are reduction of propeller hub vortex and improvement of wake fields. Therefore, we need to confirm the concept by visualization of the viscous flow field, and studying its nature of it at many cross-sections around the ESD if possible. By doing so, any required modifications to ESD parameters can be made, and finally, the optimum design can be achieved based on the flow field. In the previous chapter, the phase-averaged flow field improvement of the bulbous rudder with a horizontal fin has been confirmed numerically and experimentally at five different cross-sectional planes in $\lambda/L=0.6, 0.85, 1.1, 1.35,$ and 1.6 . In the current chapter, how the characteristics of the velocity profile will be changed by three newly designed fins in the wave will be investigated in two planes ($x/L=1.0$ and $x/L=1.025$) at $\lambda/L=0.6, 1.1,$ and 1.6 .

Fig 5-5 gives an illustration of a comparison of the axial velocity contour (u/U) and cross-flow vectors ($v/U, w/U$) between new fins and original fin at $x/L=1$ for $\lambda/L=1.1$, medium wave condition. The computed results of a normal rudder, RBFS with original fin, cut0.005-fin, cut0.007fin, and NACA-fin are presented in column 1, 2, 3, 4, and 5 respectively. The wake fields were drawn in six phases (0deg, 60deg, 120deg, 180deg, 240deg and 300deg) over one encounter period. Phase 0deg means that the wave is crossing up the zero line at the position of wave gauge meter as described in Fig 5-4(b).

Similar to the phase-averaged wake field of the original fin, the axial velocities were accelerated by the propeller to 1.6 times of ship speed in that of cut0.005fin, cut0.007fin and

NACA-fin. The upward flow in the outer area of the flow field was observed in every single phase. The hub vortex would tend to move toward the left side, i.e. portside, in the upward flow. That was owing to the propeller that rotates clockwise as viewed from the stern side. The vertical ship movement could be seen clearly in all types of the rudder.

In 0deg phase, there was no significant difference of wake field at port side. In starboard side, the low-speed region was found at the root of the fin in both cut-fins and NACA fin. In 60deg phase, a significant difference was not observed in both side of rudder. The speed of the circular motion under the starboard side fin was weak in cut-fins due to the short fin's span. In 120deg phase, the flow field was almost the same in all types of the fin on the starboard side. The small-scaled flow separation above the port side fin disappeared in NACA-fin but it was still observed in two cut-fins. This might be owing to the 6degree AOA in the upward direction. This might be an advantage of lowering the pressure resistance. In 180deg phase, the reverse circulating flow was investigated in the root of the port side fin of cut0.007fin and NACA-fin. However, the flow separation near the tip of the port side fin was weakened. Moreover, the low-speed area at root of the fin became slightly smaller by cut0.007fin and NACA-fin. In 240deg phase, the small-scaled flow separation at tip of the port side fin and the root of the starboard side fin of the original RBFS was diminished to some extent in cut0.007fin and NACA-fin because of the AOA. The low-speed region above the starboard side fin was a bit larger in these types of fin. In 300deg phase, the complex flow pattern in the port side of the original RBFS became smooth marginally in both cut-fins and NACA-fin. The nature of wake field was changed a bit in the starboard side of these fins.

Therefore, it could be proved that the newly designed fins did not have any adverse effect on the wake field and maintained the advantage of reducing the hub vortex as the original one. In addition, they could lessen the flow separation that was observed in the original fin.

Various Fin's Configurations

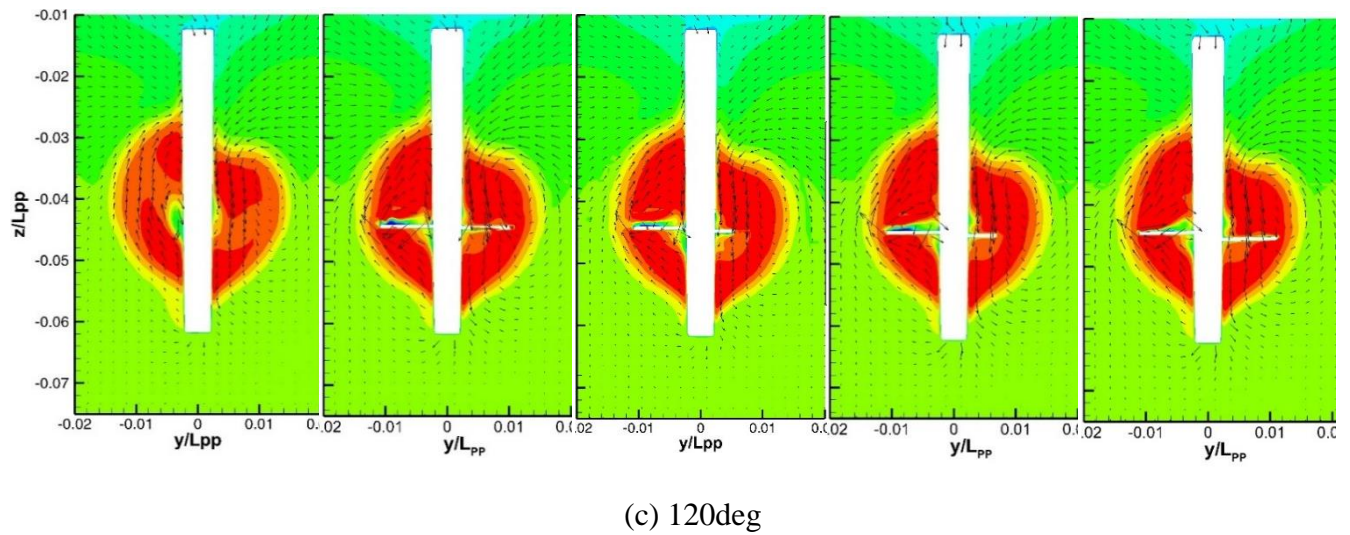
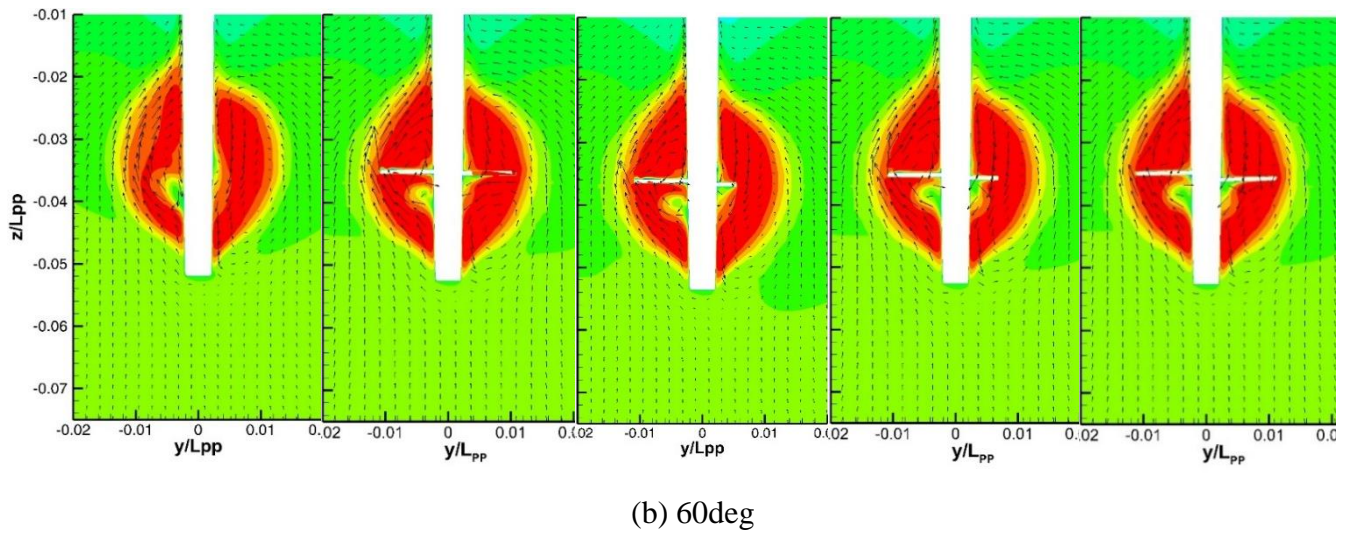
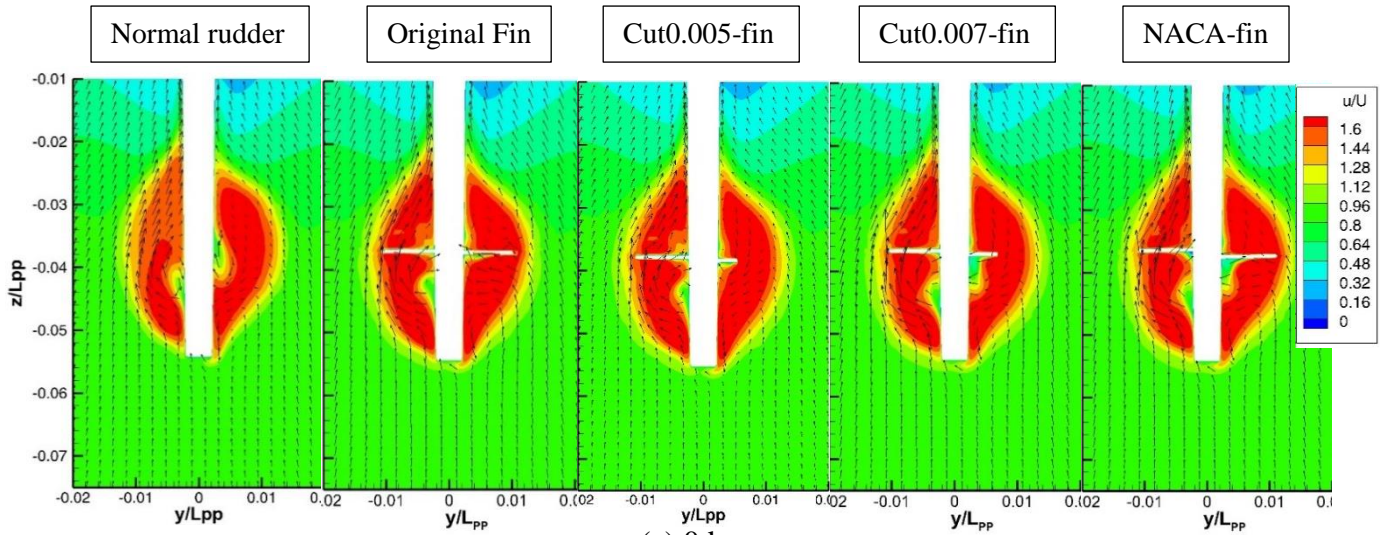
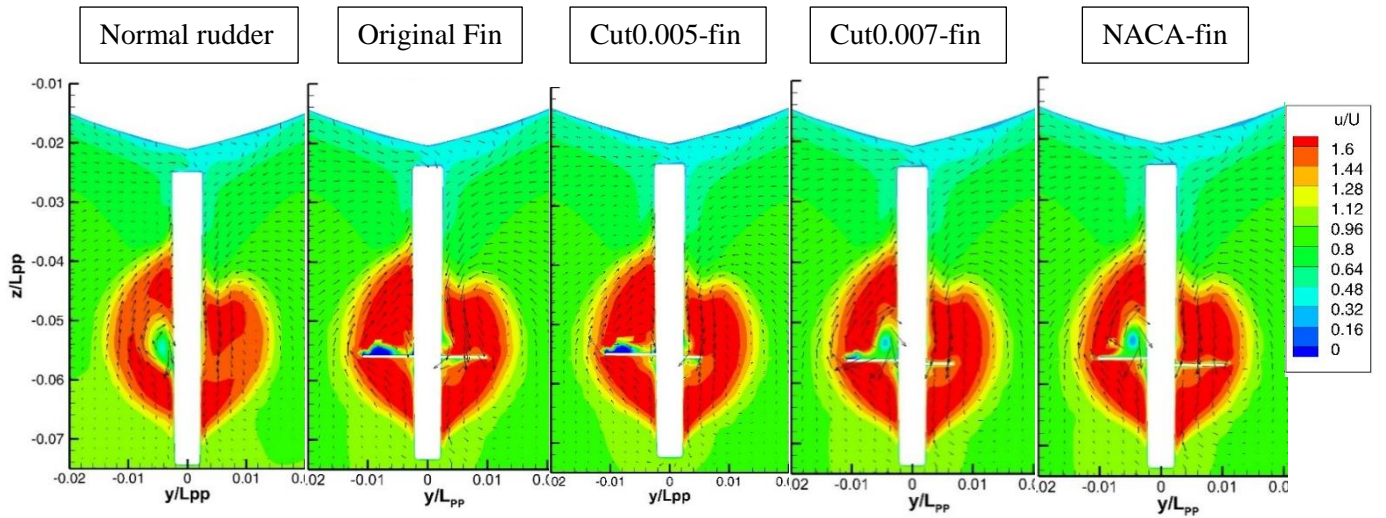
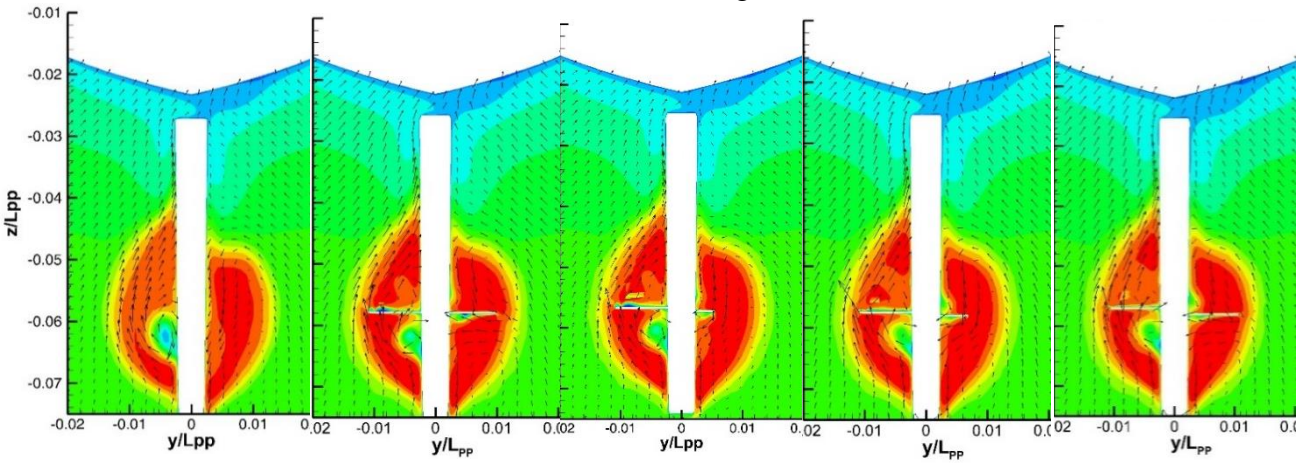


Fig 5-5 Comparison of flow field at $x/L=1.0$ in $\lambda/L=1.1$

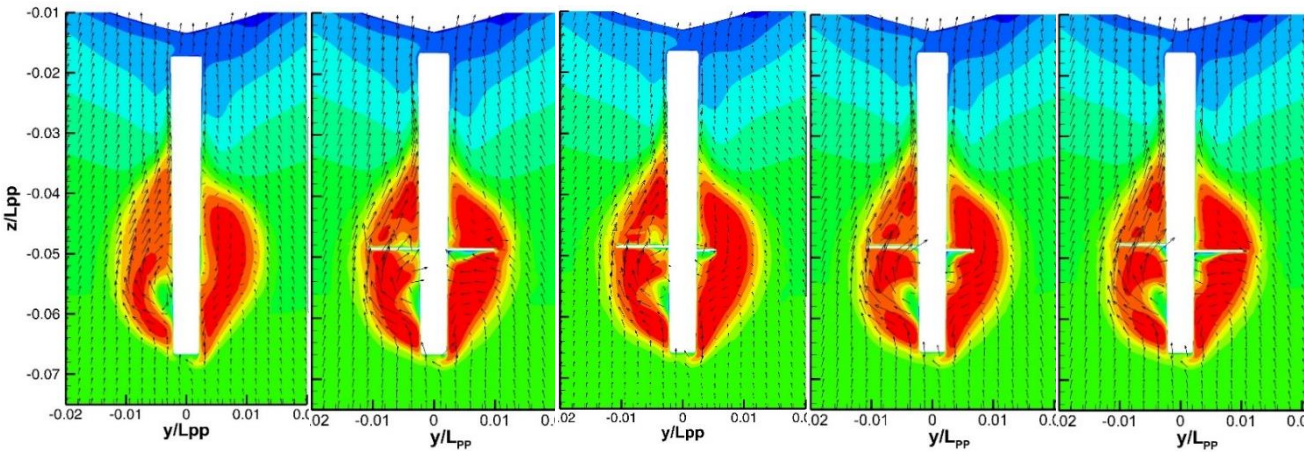
Various Fin's Configurations



(d) 180deg



(e) 240deg



(f) 300deg

Fig 5-5 (continued)

5.4.2.2 Flow field at $x/L=1.025$

The viscous wake dynamics downstream of a rudder is one of the primary concerns of this research to see how much RBF can change the wake field and is effective. For this reason, a comparison of the axial velocity profile between an original fin and newly designed fins was carried out in three wavelengths ($\lambda/L=0.6, 1.1, \text{ and } 1.6$) at $x/L=1.025$, which is the downstream of the rudder as described in Fig 4-17.

Fig 5-6 provides the comparison of the wakefield fluctuation at $x/L = 1.025$, which is 8cm behind the AP, in $\lambda/L=1.1$. The flow field figures are composed of the axial velocity contour (u/U) and cross-flow vectors (v/U and w/U). The predicted results of a normal rudder, RBFS with original fin, cut0.005-fin, cut0.007fin, and NACA-fin are illustrated in columns 1, 2, 3, 4, and 5 respectively. The predicted phases were divided equally into six phases starting from 0deg to 360deg with an increment of 60 degree over one encounter period as shown in Fig 5-4(b).

According to the large motion of a ship in the medium wave, movement of the velocity contour and transformation of its shape could be seen clearly in each phase diagram of all types of the rudder. Compared to the wake field in a section of $x/L=1.0$, the speed of the axial velocity became weak as the water particles moved away from a ship and a propeller. In the same way as the original fin, the range of high-speed axial velocity contour in cut0.005-fin, cut0.007-fin, and NACA-fin were slightly larger than that of a conventional rudder. In the comparison of the original fin with newly designed fins, there was no prominent or major difference. Only a small improvement of wake field in two cut-fins was observed on the starboard side. The concaved shape of the high-velocity field formed on the starboard side of an original fin was smooth and strong slightly in cut0.005-fin and cut0.007-fin. Similar to the original fin, the new fins weakened the strength of the hub vortex and the velocity around it. It may lead to the reduction of the vortex resistance and further improvement of the propulsion performance of a vessel.

Various Fin's Configurations

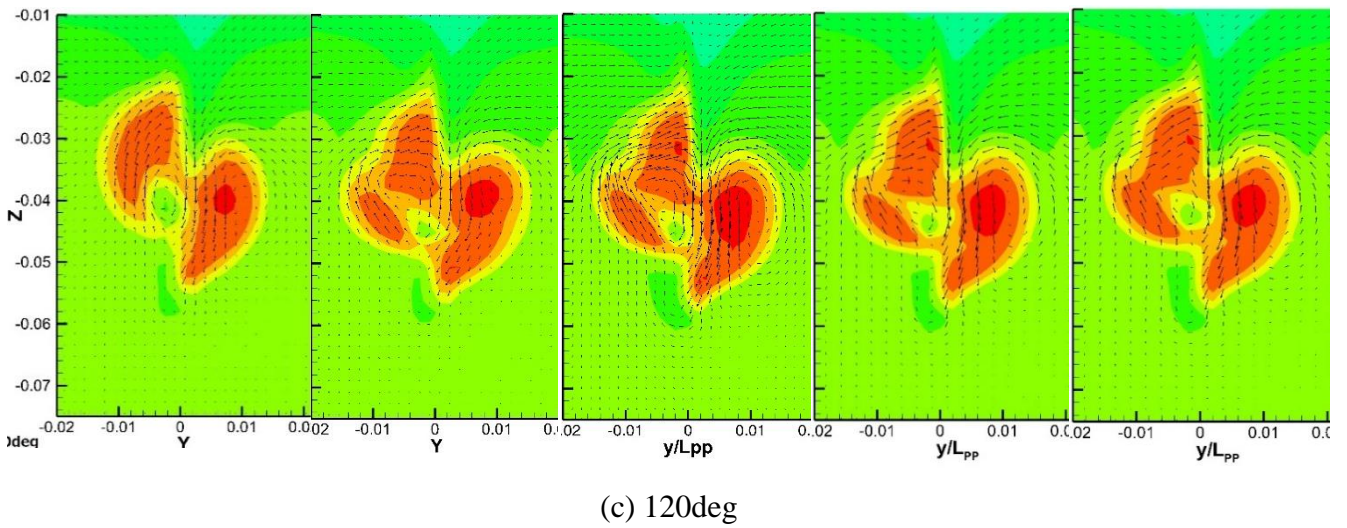
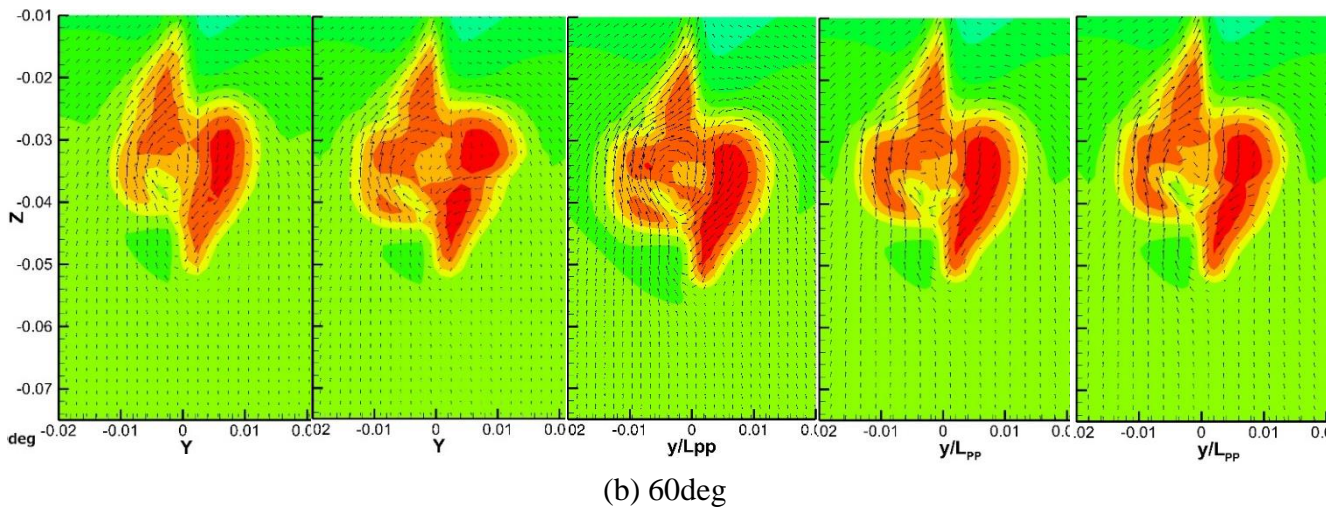
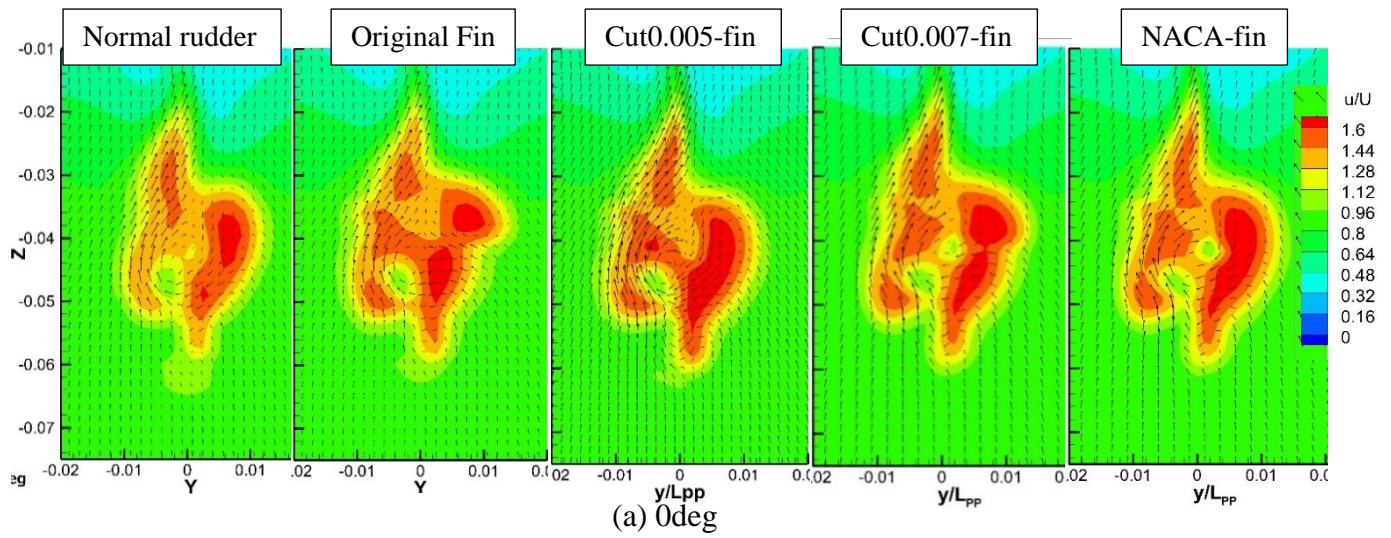
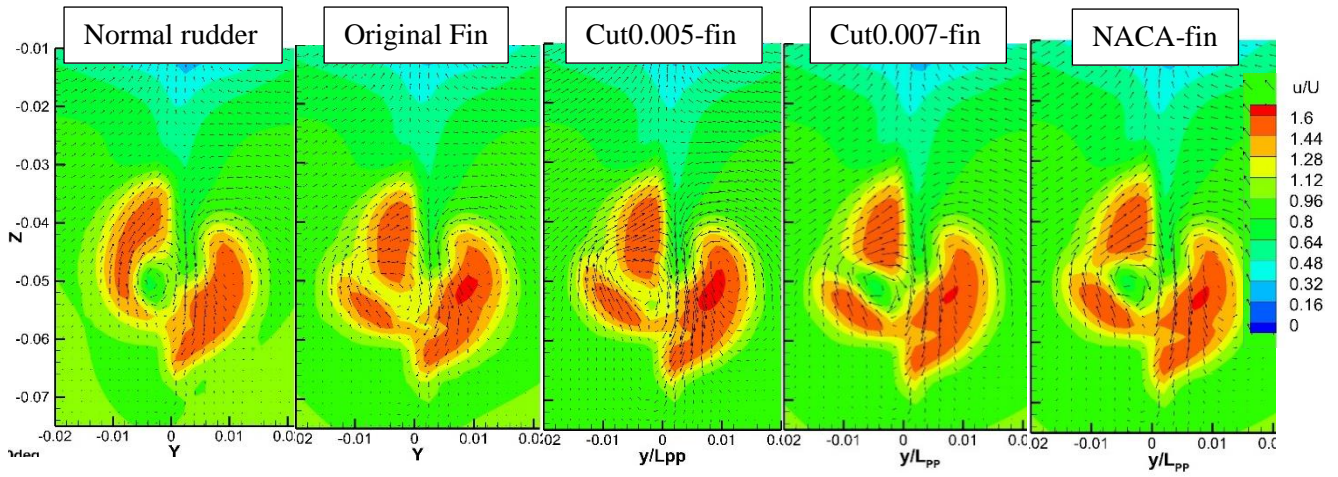
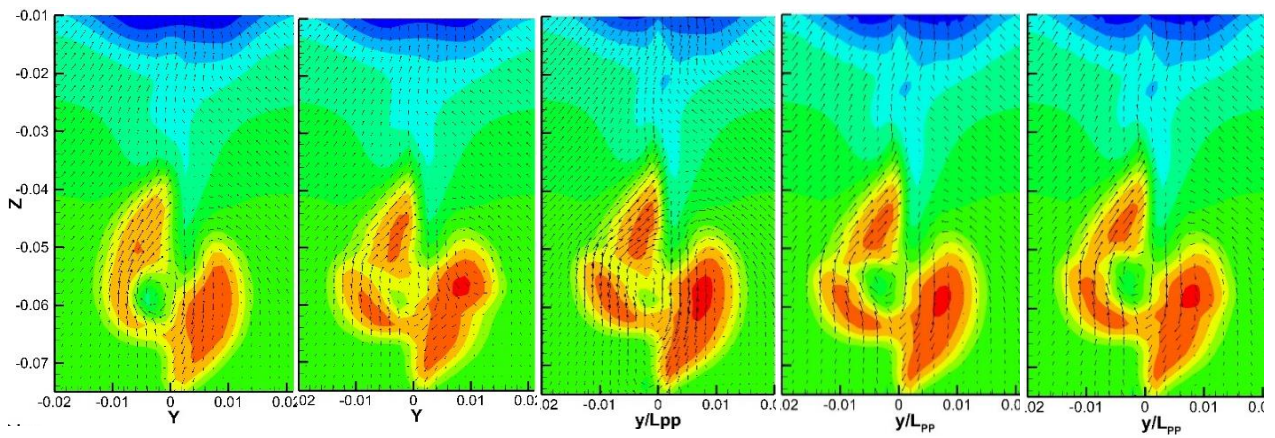


Fig 5-6 Comparison of flow field at $x/L=1.025$ in $\lambda/L=1.1$

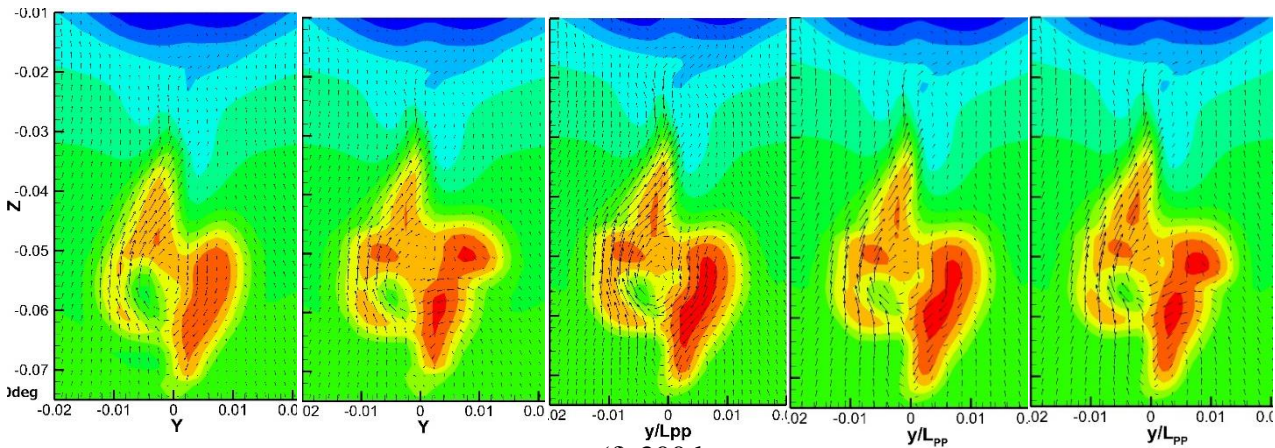
Various Fin's Configurations



(d) 180deg



(e) 240deg



(f) 300deg

Fig 5-6 (continued)

5.4.3 Self-propulsion factors

One of the purposes of designing new rudder fins is to lessen the burden of resistance in the ship propulsion system. For this reason, the comparison of resistance between normal rudder, rudder with original fin, and new fins were performed in three wavelengths ($\lambda/L=0.6$, 1.1, and 1.6). Fig 5-7 reveals the change of mean resistance by various RBFS compared with an conventional rudder.

In short wavelength, $\lambda/L=0.6$, all newly designed fins increased a bit the resistance even though the original one reduced it by about 0.9%. The resistance was risen roughly 2.4%, 0.5%, and 1.7% by cut0.005fin, cut0.007fin, and NACA-fin. All types of RBFS cut down the resistance about 1.1%, 0.6%, 7.8%, and 7.5% respectively in $\lambda/L=1.1$. In long wavelength, $\lambda/L=1.6$, similar to the medium wavelength, original fin, cut0.005-fin, cut0.007-fin, and NACA-fin decreased the total resistance by nearly 0.07%, 2.7%, 10.1%, and 12.8%. Overall, it could be reported that the RBFS could reduce the total resistance to some amount in most of the wavelengths. In comparison to the available experiment data, CFD over-predicted the resistance of a hull with cut0.005fin approximately 3.3%, 5.6%, and 20% in each wave condition. Nevertheless, it could follow the same trend as the EFD measurement.

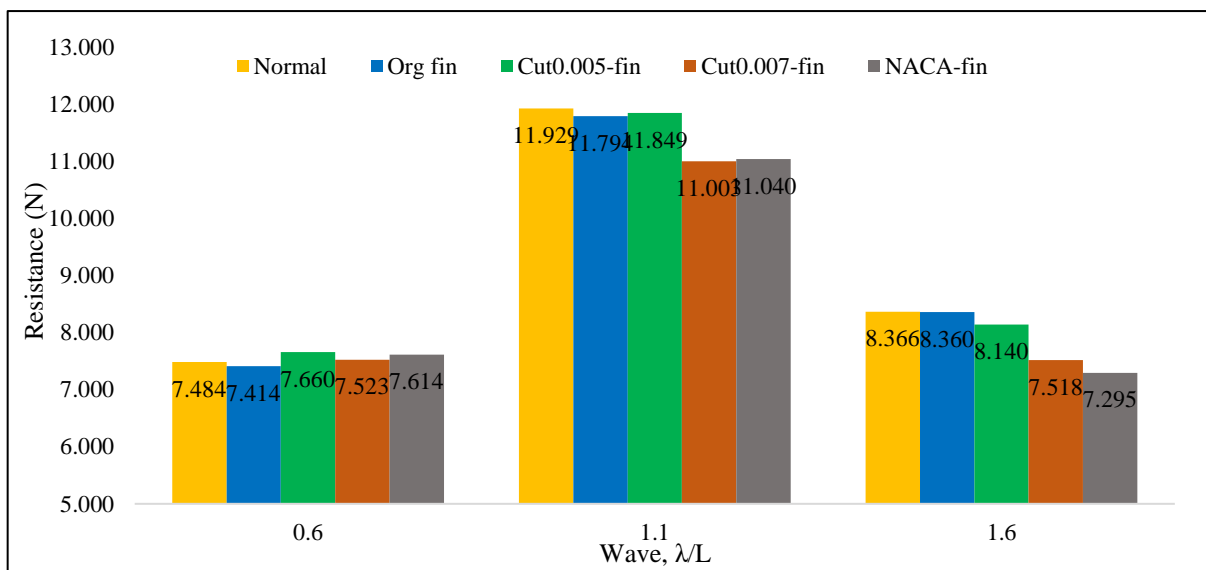


Fig 5-7 Comparison of total resistance predicted by CFD

Thrust comparison was also performed since the additional thrust produced by rudder fin is one of the main concerns in this study. In calm water, the new fins generated 0.3%, 1.0%, and 0.97% of additional thrust as compared to the convectional rudder. Thus, we needed to investigate whether they could keep this improvement or were more efficient in waves. Fig 5-

8 provides the comparison of computed thrust between five types of rudder in three wavelengths, $\lambda/L=0.6$, 1.1, and 1.6.

All types of RBFS produced the additional thrust more or less in wave conditions. In short wavelength, $\lambda/L=0.6$, two cut-fins increased the thrust by about 0.23% and 0.75% as compared to the normal rudder. NACA-fin also raised the propeller thrust with 0.83% improvement. All new fins exceeded the generated thrust by 0.5%, 0.93%, and 0.98% respectively in $\lambda/L=1.1$. The rate of improvement of thrust by new RBFS in long wavelength was higher a little than that in other wavelengths. 1.65%, 1.9%, and 1.96% improvement of thrust by cut0.005-fin, cut0.007-fin, and NACA-fin were observed in $\lambda/L=1.6$ in contrast to the conventional rudder. Therefore, it could make a remark that RBFS with all types of fin in this study had a potential for generating the additional thrust in waves as in the calm water. CFD under-predicted the thrust of a propeller in a condition with cut0.005fin in short and medium wavelength. The estimated amount of error was around 0.8%. It over-predicted approximately 0.68% of thrust in $\lambda/L=1.6$, as opposed to the experimental result.

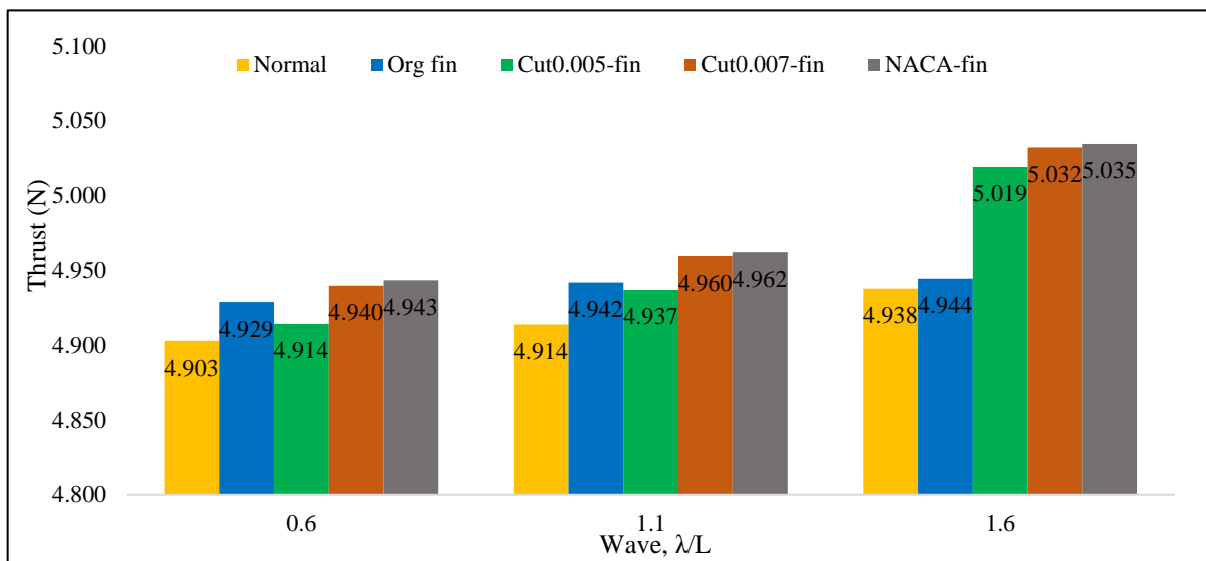


Fig 5-8 Comparison of thrust predicted by CFD

The most interesting factor in this study, hull efficiency, in each case was estimated by CFD and compared with the conventional rudder in three wavelengths. The compared results with each other cases are shown in Table 5-2. The wake fraction and thrust deduction fraction are also presented in that table. Table 5-3 provides the self-propulsion factors measured in the experiment for validation.

The newly developed fins improved significantly the hull efficiency in all wave conditions. In short wavelength, $\lambda/L=0.6$, 1.17%, 4.18% and 1.85% of improvement in hull

efficiency by cut0.005-fin, cut0.007-fin, and NACA-fin was investigated as compared to the normal rudder. Among all wavelengths, the highest improvement of hull efficiency by RBFS with various fins was observed in medium wavelength, $\lambda/L=1.1$. The amount of improvement was roughly 2.6%, 3.7%, and 4.59% in each type of new fin. RBFS with the original fin did not improve the hull efficiency in $\lambda/L=1.6$. Nevertheless, the new fins increased it by approximately 0.3%, 3.61%, and 3.13% respectively. In calm water, cut0.005-fin, cut0.007-fin, and NACA-fin enhanced the hull efficiency by about 7.45%, 8.5%, and 4%. Hence, the new fins were still effective in waves as in calm water. According to the results, cut0.007-fin and NACA-fin were more efficient than the original fin in all wavelengths. In comparison to the experiment, CFD over-predicted the hull efficiency of a ship with cut0.005-fin round about 1.2%, 6.5%, and 2.8% in each wavelength. CFD prediction followed the same trend of measured data in all wave conditions except in $\lambda/L=1.1$ where the hull efficiency was decreased by approximately 0.1% in the experiment.

Table 5-2 Comparison of self-propulsion factors predicted by CFD

Waves (λ/L)	Rudder Types	Resistance (N)	Thrust (N)	1-t	1-w	η_H
0.6	Normal	7.484	4.903	0.799	0.511	1.564
	Org fin	7.414	4.929	0.792	0.505	1.570
	Cut0.005-fin	7.660	4.914	0.804	0.508	1.583
	Cut0.007-fin	7.523	4.940	0.818	0.502	1.630
	NACA-fin	7.614	4.943	0.799	0.501	1.593
1.1	Normal	11.929	4.914	0.817	0.516	1.585
	Org fin	11.794	4.942	0.819	0.498	1.643
	Cut0.005-fin	11.849	4.937	0.817	0.502	1.626
	Cut0.007-fin	11.003	4.960	0.818	0.497	1.644
	NACA-fin	11.040	4.962	0.824	0.497	1.658
1.6	Normal	8.366	4.938	0.797	0.493	1.618
	Org fin	8.360	4.944	0.808	0.500	1.614
	Cut0.005-fin	8.140	5.019	0.782	0.482	1.623
	Cut0.007-fin	7.518	5.032	0.805	0.480	1.676
	NACA-fin	7.295	5.035	0.800	0.479	1.668

Table 5-3 Comparison of self-propulsion factors measured in experiment (Mwangi, 2021)

Waves (λ/L)	Rudder Types	Resistance (N)	Thrust (N)	1-t	1-w	η_H
0.6	Normal	7.429	4.919	0.833	0.542	1.537
	Org fin	7.403	4.927	0.839	0.542	1.548
	Cut0.005-fin	7.416	4.954	0.837	0.535	1.564
1.1	Normal	11.118	4.925	0.829	0.542	1.528
	Org fin	11.077	4.958	0.838	0.534	1.568
	Cut0.005-fin	11.218	4.973	0.810	0.531	1.526
1.6	Normal	6.749	4.946	0.836	0.537	1.558
	Org fin	6.813	4.982	0.824	0.529	1.559
	Cut0.005-fin	6.770	4.985	0.833	0.528	1.578

Chapter -6- Conclusion and Suggestions for Further Work

6.1 Conclusion

In this dissertation, CFD has been used for the systematic and comprehensive prediction of flow fields, axial force, ship motions, and self-propulsive factors of KVLCC2 model without a rudder, with a conventional rudder, and with various RBFS. These various RBFS are the ones with original symmetrical fin, cut0.005-fin, cut0.007-fin, and NACA-fin. The numerical computations were performed to investigate the energy saving mechanism of each RBFS in waves using CFDSHIP-IOWA version 4.5. Five wavelengths ($\lambda/L=0.6, 0.85, 1.1, 1.35,$ and 1.6) with 3cm wave amplitude were considered in the comparison between a normal rudder and an original RBFS. The performance of the newly developed fins based on the calm water conditions was investigated in three wavelengths ($\lambda/L=0.6, 1.1,$ and 1.6) with 3cm wave amplitude. The computational results of the motions, wake fields, and self-propulsion factors were compared with the available data measured in the experiment which was carried out in the towing tank of Osaka University by Mwangi (2021). A good agreement of CFD with the measured data was reported.

6.1.1 Comparison between a normal rudder and RBFS

Two degree of freedom (DOF) motions, heave and pitch motions, were predicted to examine the effect of RBFS on the ship's motion response.

- There was no significant difference between the heave motion of a conventional rudder and RBFS. The same pattern of the time history's curve and mean value of it was observed clearly in both types of rudder.
- Similar to the heave motion, the prominent difference in pitch motion was not found out in all wave conditions. In comparison to the experimental data, CFD had good agreement with EFD although there was some abnormal measurement of pitch motion in the experiment.

The prediction of the viscous flow field at three transverse planes along with the ship's length, single longitudinal plane, and one horizontal plane and visualization of vortex were performed in three wavelengths.

- The propeller's inflow velocity field at $x/L=0.96875$ was exactly the same in both hulls with a normal rudder and conventional rudder. Compared to the boundary layer near

Conclusion and Suggestions for Further Work

the hull and stern tube measured in the experiment, it was observed that CFD predicted the larger boundary layer.

- In the comparison of the wake field at $x/L=1.0$, the range of the high-speed contour was marginally wider in the RBFS than in the normal rudder. The hub vortex's size was shrunk a bit by rudder blub on the port side.
- The hub vortex's strength and velocity around its core in the RBFS became weak and small owing to the rudder bulb at the flow field downstream of a rudder. The computational flow field was slightly slower than the measured flow field in $\lambda/L=1.1$ and 1.6.
- The wide area of the high-speed region in RBFS was also observed at the flow field of $y/L=0.0$ section in all wavelengths as compared to the normal rudder.
- According to the wake field at the horizontal plane, the flow separation formed in the port side of a normal rudder was improved by RBFS. Nonetheless, the small-scaled flow separation was investigated at the trailing edge of the starboard side rudder fins.
- It was clearly seen that the rudder fin on starboard side eliminated overwhelmingly the strength of hub vortex.

The effective wake, thrust, torque, delivered power, axial force, and efficiencies of both types of the rudder were computed and compared to each other.

- RBFS increased the effective wake in all wave conditions. The CFD under-predicted with around 5% error the mean value of $1-w$ and computed a similar trend compared to the experiment in each case.
- Thrust was enhanced up to 0.6% by RBFS in all wavelengths except $\lambda/L=1.35$ where the additional thrust could not be produced by the rudder fin.
- In CFD simulation, the resistance of a hull with RBFS dropped around 1.0% in $\lambda/L=0.6$, 1.1, and 1.6 but it rose 1.9% and 0.9% in $\lambda/L=0.85$ and 1.35 respectively. CFD over-predicted the axial force with an average error 8% as compared to the experiment.
- Hull efficiency was improved by about 0.3% and 3.7% at $\lambda/L=0.6$ and 1.1 due to the RBFS. It deteriorated with 0.2% reduction in $\lambda/L=1.6$. CFD over-predicted the hull efficiency of both rudder cases with an average error of 3.0% in the comparison with EFD.

Conclusion and Suggestions for Further Work

- The quasi-propulsive efficiency was increased by roughly 1.5% in medium wavelength, $\lambda/L=1.1$ but it dropped slightly with the estimated reduction of 0.14% and 0.02% in $\lambda/L=0.6$ and 1.6.

Overall, RBFS could improve the propulsion efficiency of KVLCC2 model in some wavelengths, and CFD had a good agreement with EFD. Therefore, RBFS in the present study may contribute to achieving the required EEDI index and meeting some SDGs.

6.1.2 Various fin's configurations

The numerical simulation of three newly designed fins based on the performance in calm water was carried out in three wavelengths.

- The significant difference between the original fin and new fins in heave and pitch motions was not discovered.
- Similar to the original fin, the new fins could maintain the reduction of the propeller hub vortex. Moreover, the flow separation in the trailing edge of the starboard-side fin was diminished by the new fins, especially NACA-fin.
- The resistance was increased by around 1.2% in a short wavelength but it was decreased by approximately 7% in the medium and long wavelength.
- The new fins produced the additional thrust in all wavelengths as compared to the normal rudder.
- Hull efficiency was improved up to 4.6% by the new fins in all wavelengths. It was observed that cut0.007-fin and NACA-fin were more efficient than the original fin.
- CFD predicted the self-propulsion factors of cut0.005-fin well and followed the same trend of hull efficiency in the experiment.

6.2 Suggestions for Further Work

The following studies are suggested as the further research that needs to be done in the future.

- The optimization of the rudder fin is still necessary for further research not only in clam water but also in waves, for example, moving either the vertical position or the horizontal position of the fin based on the flow field analysis.
- As the laminar flow plays a significant role in model scale whereas the full-scale scenarios generate the complete turbulent flow with an insignificant laminar region, the investigation of the performance of RBFS should be carried out in full scale for a good accuracy as compared to the reality. Moreover, to verify EEDI for a ship with ESD by classification societies, the extension of propulsive performance results from the model to full scale is mandatory⁴³⁾.
- In the present study, the performance of RBFS has been investigated in the wave conditions that only the wavelength was varied but the wave amplitude was fixed as the same. Mwangi (2021) studied the wave amplitude dependency on the propulsion of KVLCC2, in which the relative ship motion increased and high-velocity flow entered the propeller plane from the bottom as the wave amplitude increased⁴⁰⁾. For this reason, the effectiveness of RBFS may differ in waves with various wave amplitudes and such kind of investigation should be carried out numerically and experimentally.
- Last but not least, the study on the performance of a combination of RBFS and other ESDs; especially the ones installed in front of a propeller, for example, the wake equalizing duct, is proposed for future research.

References

- 1) Policy Update 15 by the International Council on Clean Transportation, October 3, 2011.
- 2) Wang, X., Yuen, K. F., Wong, Y. D., and Li, K. X.: "How can the maritime industry meet Sustainable Development Goals? An analysis of sustainability reports from the social entrepreneurship perspective", *Transportation Research Part D: Transport and Environment*, Vol. 78, 2020.
- 3) Report of the Specialist committee on Energy Saving Methods, Proceedings of 28th ITTC, Volume II, pp 661-720.
- 4) Robert B Zubaly "Applied Naval Architecture" June 30, 2009.
- 5) Xu, L., He, D., and Wan, D.: "Research Status and Analysis of the Ship Hydrodynamic Energy-saving Devices", 2017.
- 6) Crist, P.: "Greenhouse gas emissions reduction potential from international shipping", Working paper, OECD, 2009.
- 7) Matsumoto, D. and Sakamoto, T.: "Finned Rudder", Patent EP2110311A2, 2009.
- 8) Mewis, F. and Deichmann, F.: "Power and Cost-Savings for Container Vessels by Hydrodynamics Energy Saving Devices", *SHIP EFFICIENCY* by STG, 2013.
- 9) Hoshino, T., Oshima, A., Fujita, K., Kuroiwa, T., Hayashi, F., and Yamazaki, E.: "Development of High-Performance Stator Fin by Using Advanced Panel Method", *MHI Tech Review*, 41(6), 1-4, 2004.
- 10) Kawakita, C., Takashima, R., and Sato, K.: "CFD on Cavitation around Marine Propellers with Energy-Saving Devices", *MHI Tech Review*, 49(1), 63-67, 2012.
- 11) Okada, Y., Kawasaki, M., Katayama, K., Okazaki, A., Fukuda, K.: "The Development of Ultimate Rudder for EEDI", *International Conference on Computational Methods in Maritime Engineering*, 2015.
- 12) Nielsn, J.R., Shin, K.W., Lundgren, E., Faghani, F.: "Combined Kappel propeller and rudder bulb system for improved propulsion efficiency", *MAN Diesel & Turbo*, Frederikshavn, Denmark, 2012.
- 13) Kim, JH, Choi, JE, Choi, BJ, and Chung, SH.: "Twisted Rudder for Reducing Fuel-Oil Consumption", *International Journal Naval Architecture and Ocean Engineering*, Vol.6, pp 715-722, 2014.
- 14) Li, X. J., Miao, F. and Shen, H. L.: "Numerical prediction of energy saving effect of rudder ball based on CFD Technology", *Ship Standardization Eng*, 47(3):18-20, 2014.

References

- 15) Yan, G. Z., Chen, L. Q. and Huang, S. Q.: "Evaluation and analysis of the energy-saving effect of fin stabilizer and rudder bulb in the open water", National Symposium on water dynamics, 2014.
- 16) Chen, L. Q. and Huang, S. Q.: "Analysis on energy saving effect of variable parameters of rudder ball under self-propulsion", National Symposium on hydrodynamics, 2015.
- 17) Wang, G. B. and Xie, Y. H.: "Calculation and analysis of the hydrodynamic performance of duct propeller with rudder ball", *Marine Eng*, 42(3):48-50, 2013.
- 18) Hu, H. Z., Su, Y. M. and Sheng, H. L.: "Study on the energy saving effect of rudder thrust fins", *Ship Science and Technology*, 38(3):67-72, 2016.
- 19) Wang, W. Q., Wang, S. X. and Zhang, T. T.: "Hydrodynamic performance analysis of ruder thrust fins in ship motion", *Journal of ship*, 27(6):67-72, 2016.
- 20) Shin, K. W. and Andersen, P.: "CFD analysis of Rudder Bulb Performance in Ship Maneuvering", 6th World Maritime Technology Conference, Shanghai, China, 2018
- 21) Shen, H. L., Obwogi, E. O. and Su, Y. M.: "Scale effects for rudder bulb and rudder thrust fin on propulsive efficiency based on computational fluid dynamics", *Ocean Eng*, 199-209, 2016.
- 22) Tacar, Z., Sasaki, N., Atlar, M., and Korkut, E.: "An investigation into effects of gate rudder system on ship performance as a novel energy-saving and manoeuvring device", *Journal of Ocean Engineering*, Vol. 218, 2020.
- 23) Su, Y., Lin, J., Zhao, D., Guo, C., and Guo, Hang.: "Influence of a pre-swirl stator and rudder bulb system on the propulsion performance of a large-scale ship model, *Journal of Ocean Engineering*", Vol. 218, 2020.
- 24) Obwogi, E. O., Shen, H. L., and Su, Y, M.: "The design and energy saving effect prediction of rudder-bulb-fin device based on CFD and model test", *Journal of Applied Ocean Research*, Vol 114, 2021.
- 25) Kim, K., Andersen, M. L., and Orych, M.: "Hydrodynamic Optimization of Energy Saving Devices in Full Scale", 30th symposium on Naval Hydrodynamics, Hobart, Tasmania, Australia, November, 2014.
- 26) Truong, T. Q., Wu, P-C., Aoyagi, K., Koike, K., Akiyama, Y. and Toda, Y.: "The EFD and CFD Study of Rudder-Bulb-Fin System in Ship and Propeller Wake Field of KVLCC2 Tanker in Calm Water", 27th ISOPE, California, USA, 2017.
- 27) Truong, T. Q., and Toda, Y.: "The CFD study of rudder-bulb-fin system in changing cambered Foil and AOA applied to KVLCC2 tanker", *Proceedings of 11th International*

References

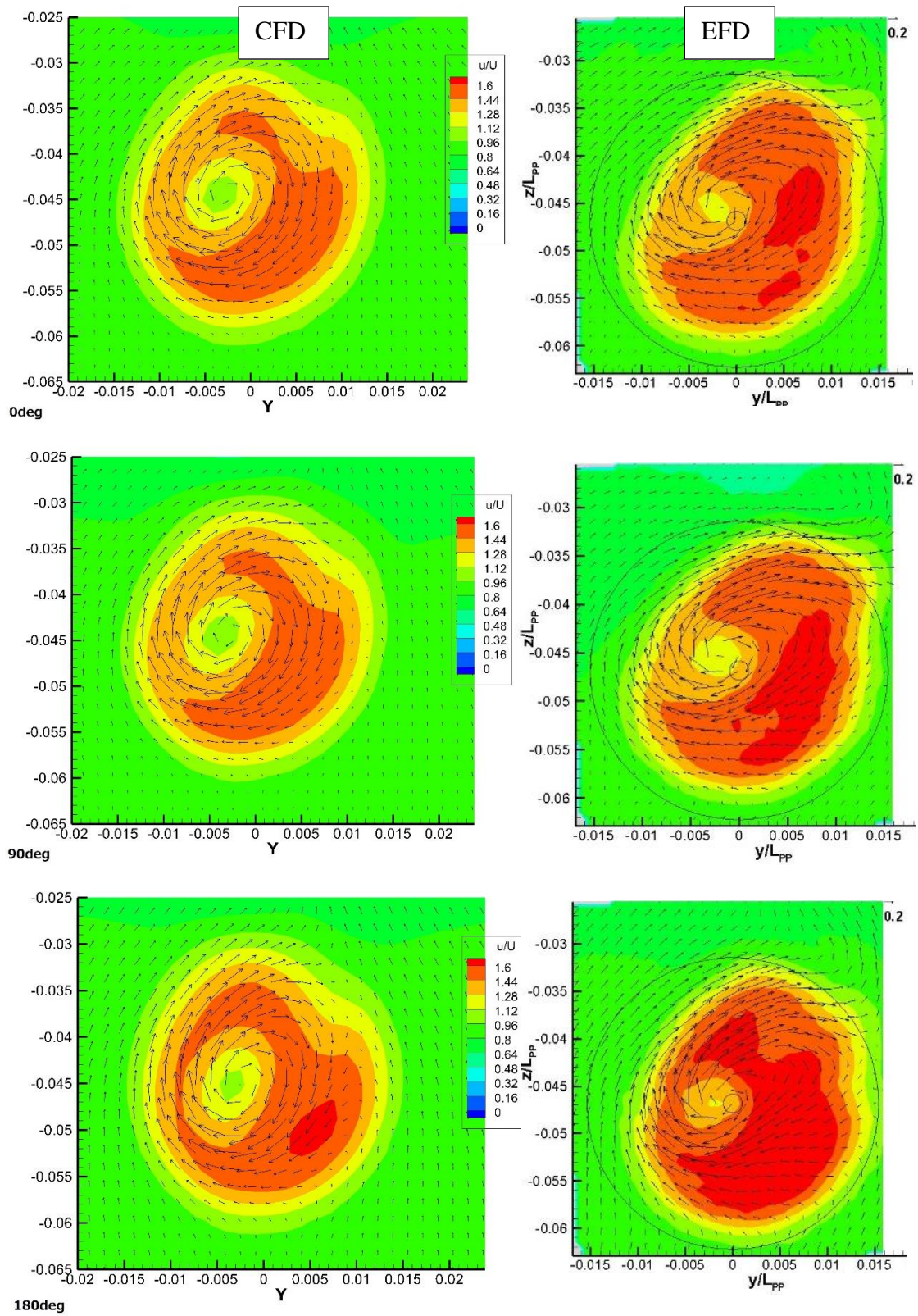
- Workshop on Ship and Marine Hydrodynamics, Hamburg, Germany, September 22-25, 2019.
- 28) Truong, T.Q., Toda, Y., and Ogawa, S.: “Improvement of rudder-bulb-fin system”, Proceedings of JASNAOE Spring Conference, pp 371-374, Japan, June, 2019.
- 29) Mwangi, B.O., Matsuura, H., and Toda, Y.: “The effect of energy saving devices (ESDs) on the flow field around the stern of KVLCC2 model tanker”, Proceedings of 31st ISOPE, pp 2651-2658, Rhodes, Greece, June, 2021.
- 30) Truong TQ. : “A Study on Rudder-Bulb-Fin System Applied to KVLCC2 Tanker in Calm Water”, doctoral dissertation, Graduate School of Engineering, Osaka University, 2019.
- 31) Retrieved from Pointwise, Gridgen: "<http://www.pointwise.com/>".2010.
- 32) Sadat-Hosseini, H., Wu, P-C., Carrica, P. M., Kim, H., Toda, Y. and Stern, F. (2013) “CFD verification and validation of added resistance and motions of KVLCC2 with fixed and free surge in short and long head waves”, Ocean Engineering, Vol 59, pp 240-273, 2013.
- 33) Practical guidelines for ship CFD applications, ITTC- recommended procedures and guidelines, 2014.
- 34) Weymouth, G., Wilson, R., and Stern, F.: “RANS CFD Predictions of Pitch and Heave Motions in Head Seas”, Journal of Ship Research, Vol. 49, pp. 80-97, 2005.
- 35) Paterson, G., Wilson, W. and Stern, F.: "General-purpose parallel Unsteady RANS Ship Hydrodynamics Code", CFDSHIP-IOWA, IIHR Report No.432, pp.2-21, 2003.
- 36) <https://www.iuhr.uiowa.edu/shiphydro/cfd-code/>
- 37) Morgut, M and Nobile, E.: “Influence of grid type and turbulence model on the numerical prediction of the flow around marine propellers working in uniform flow”, Journal of Ocean Engineering, Vol 42, pp 26-34, 2012.
- 38) Tokgoz, E., Kuroda, K., Win, Y.N., and Toda, Y.: "A New Method to Predict the Propeller Body-force Distribution for Modeling the Propeller in Viscous CFD Code without Potential Flow Code", Journal of the Japan Society of Naval Architects and Ocean Engineers, Vol. 19, pp.1-7, 2014.
- 39) Emel Tokgöz.: “A CFD Study on the Propeller-Hull Interaction Flow in Waves Using Body-Force Distribution Model”, Doctoral dissertation, Osaka University, 2015.
- 40) Mwangi, B.O.: “SPIV Flow Field Measurement around the Stern of a Self-propelled KVLCC2 Model Ship in Regular Head Waves”, Doctoral dissertation, Osaka University, 2021.

References

- 41) Kishi, J.: “The EFD and CFD Study on various Rudder-Bulb-Fin System in Ship and Propeller Wake Field”, Master Thesis, Graduate School of Engineering, Osaka University, 2018. (in Japanese)
- 42) Bertram, V.: “Chapter-3: Resistance and propulsion; Practical Ship Hydrodynamics”, Second edition.
- 43) Park, S., Oh, G., Rhee, S. H., Koo, B-Y., and Lee, H.: “Full scale wake prediction of an energy saving device by using computational fluid dynamics”, Journal of Ocean Engineering, Vol. 101, pp. 254-263, 2015.

APPENDIX

Computed and Measured Flow field of a KVLCC2 model without a rudder



APPENDIX

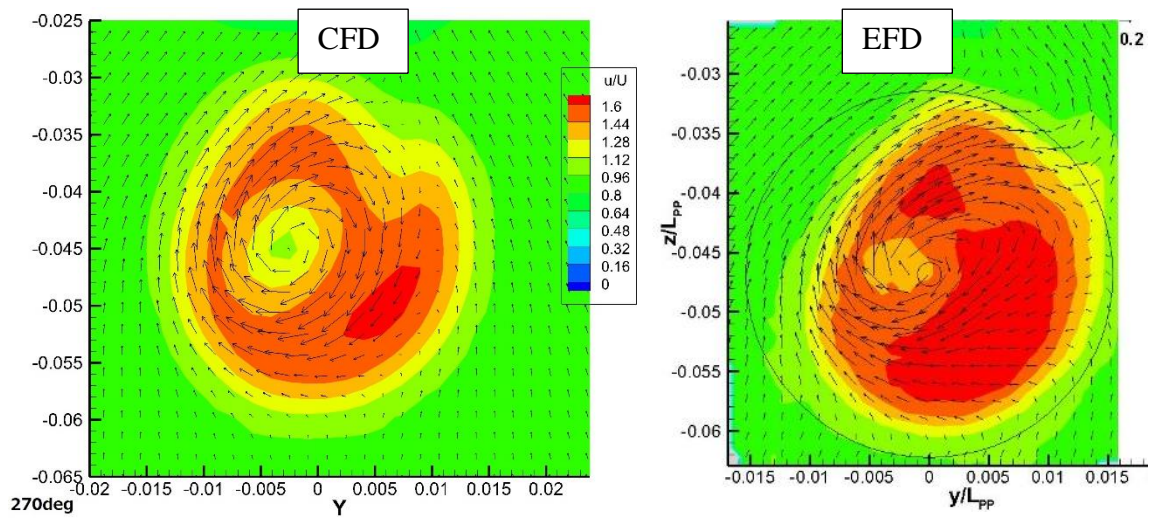


Fig. Comparison of flow field at $x/L=1.025$ in $\lambda/L=0.6$ (Left: CFD & Right: EFD)

List of publications

Journal Paper

Htay, W. N., Mwangi, B. O., Matsuura, H., and Toda, Y.: “Effectiveness of bulbous rudder with horizontal fins on the propulsion performance of ship in waves”, *Journal of The Japan Society of Naval Architects and Ocean Engineers*, Vol 34, pp. 29-36, 2021.

Peer-reviewed International Conference Proceedings

Htay, W. N., Truong, T. Q. and Toda, Y.: “A CFD based Comparison Study of Conventional Rudder and Rudder with Bulb-Fins System of KVLCC2 in Waves”, *Proceedings of 30th International Offshore and Polar Engineering Conference*, Vol. 4, pp. 3377-3384, 2020.

Htay, W. N., Magari, A., and Toda, Y.: “A Study on the Performance of Rudder Bulb Fins System of KVLCC2 in Regular Head Waves”, *Proceedings of 31st International Offshore and Polar Engineering Conference*, Vol. 4, pp. 2643-2650, 2021.

Domestic Conference Proceedings

Htay, W. N., Mwangi, B. O., Matsuura, H., and Toda, Y.: “Effectiveness of bulbous rudder with horizontal fins on the propulsion performance of ship in waves”, *Autumn Conference of The Japan Society of Naval Architects and Ocean Engineers*, Vol 33, pp. 501-508, 2021.

Htay, W.N., Tsuda, Y., RoyChoudhury, S., and Toda, Y.: “Energy-Saving Effect of Bulbous Rudder with Fins Having Different Configurations in Waves”, *Spring Conference of The Japan Society of Naval Architects and Ocean Engineers*, Vol 34, pp. 275-280, 2022.

Curriculum Vitae

Education

Doctoral Course (Naval Architecture and Ocean Engineering) 2019 – To date

Osaka University, Japan

Advisor: Prof. Yasuyuki Toda

Areas of research: Computational fluid dynamics, Energy-saving device, Resistance and Propulsion

Topic: “Study on the Energy Saving Mechanism of Rudder-Bulb-Fins System applied to KVLCC2 Model in Waves”

Master of Engineering (Naval Architecture and Ocean Engineering) 2017-2019

Osaka University, Japan

Advisor: Prof. Yasuyuki Toda

Areas of research: Computational fluid dynamics, Energy-saving device, Resistance and Propulsion

Topic: “A CFD based Comparison Study of Conventional Rudder and Rudder with Bulb-Fins System of KVLCC2 in Waves”

Bachelor of Engineering (Naval Architecture) 2011-2017

Myanmar Maritime University, Myanmar

Advisor: Dr. Aye Aye Mon

Areas of study: Ship design, Structural design, Ship stability, Resistance, Propulsion, and Powering

Topic: “Design of River Cruise and Resistance Analysis with CFD Simulation”